2009

In-Situ Growth of Porous Alumino-Silicates and Fabrication of Nano-Porous Membranes

Pradeep Kodumuri
Cleveland State University

IN-SITU GROWTH OF POROUS ALUMINO-SILICATES AND FABRICATION OF NANO-POROUS MEMBRANES

PRADEEP KODUMURI

Bachelor of Technology in Chemical Engineering

Nagarjuna University, India

June, 2000

Master of Science in Chemical Engineering

University of Louisiana at Lafayette

July, 2003

submitted in partial fulfillment of requirements for the degree

DOCTOR OF ENGINEERING

at the

CLEVELAND STATE UNIVERSITY

May, 2009

This dissertation has been approved for the Fenn College of Engineering and the College of Graduate studies by

_____

Dissertation Chairperson, Dr. Surendra N. Tewari

_____

Department & Date

_____

Dr. Orhan Talu

_____

Department & Date

_____

Dr. Dhananjai B. Shah

_____

Department & Date

_____

Dr. Nolan Holland

_____

Department & Date

_____

Dr. Stan Duraj

_____

Department & Date

DEDICATION

This work is dedicated to my loving wife *Anuraga Jyothi* and my son *Pranet* who mean more to me than the world.

ACKNOWLEDGMENTS

I would like to express my gratitude to DOE for their financial support through a sponsored research project. (contract# DE-FC 36-04ER14007).

Dr. Surendra N Tewari has been more than an advisor during the course of my DRE program at Cleveland State University. He has inspired me and helped me train as a researcher and develop individualistic thinking. I would like to take this opportunity to thank him for all his support, guidance and encouragement. I have also had the opportunity to learn a great deal from my co-advisor, Dr. Orhan Talu, who has guided and advised me throughout the course of my program. I would like to thank him for that. I would also like to thank Dr.Nolan Holland who gave me the opportunity to work on a short-term project and get a flavor for a different dimension of research in chemical engineering. I would like to thank my dissertation committee members Dr. D.B. Shah, Dr. Nolan Holland and Dr. Stan Duraj for serving on my committee and providing me with valuable suggestions.

Thanks go to David Epperly , Jim Barker and Ali Kaddah, for their technical support. Special thanks to Ms. Becky Laird and Ms. Darlene Montgomery who have always gone out of their way to help and support me during the course of my DRE study.

My final appreciation and love go to my dearest wife Anuraga Jyothi who has been my support system throughout my graduate study. She has always been there for me and helped me through the highs and lows. Special thanks to her.

IN-SITU GROWTH OF POROUS ALUMINO-SILICATES AND FABRICATION OF NANO-POROUS MEMBRANES

PRADEEP KODUMURI

ABSTRACT

Feasibility of depositing continuous films of nano-porous alumino-silicates, primarily zeolites and MCM-41, on metallic and non-metallic substrates was examined with an aim to develop membranes for separation of gaseous mixtures and also for application as hydrogen storage material. Mesoporous silica was deposited in-side the pores of these nano-porous disks with an aim to develop membranes for selective separations.

Our study involves supported zeolite film growth on substrates using *in-situ* hydrothermal synthesis. Faujasite, Silicalite and Mesoporous silica have been grown on various metallic and non-metallic supports. Metallic substrates used for film growth included anodized titanium, sodium hydroxide treated Titanium, Anodized aluminum, and sintered copper. A non-metallic substrate used was nano-porous aluminum oxide. Zeolite film growth was characterized using Scanning Electron Microscope (AMRAY 1820) and High Resolution Transmission electron microscope. Silicalite was found to grow uniformly on all the substrates to form a uniform and closely packed film. Faujasite tends to grow in the form of individual particles which do not inter-grow like silicalite to form a continuous film.

Mesoporous silica was found to grow uniformly on anodized aluminum compared to growth on sintered copper and anodized titanium. Mesoporous silica growth on

Anodisc® was found to cover more than half the surface of the substrate. Commercially obtained Anodisc® was found to have cylindrical channels of the pore branching into each other and since we needed pore channels of uniform dimension for Mesoporous silica growth, we have fabricated nano-porous alumina with uniform pore channels.

Nano-porous alumina membranes containing uniform distribution of through thickness cylindrical pore channels were fabricated using anodization of aluminum disks. Free-standing nano-porous alumina membranes were used as templates for electro-deposition in order to fabricate nickel and palladium nano-wire mesh with large surface area to volume ratio. Such nano-wire metallic alloy meshes have a strong potential for application as advanced hydrogen storage material.

Statistical image analysis techniques were used to determine the dependence of the pore morphology and distribution on the crystal orientation by anodizing single crystal aluminum disks that were oriented with their surface normal along [111], [110] and [111] directions. The [100] oriented disks were found to have the highest tendency to anodize in oxalic acid electrolytic solutions.

TABLE OF CONTENTS

LIST OF FIGURES

LIST OF TABLES

CHAPTER I

INTRODUCTION

1.1 Hydrogen Storage System and Nano-porous Membranes

Materials having three dimensional sub-nano structured grid porous structure will not only provide large surface area to volume ratio to increase the amount of adsorbed hydrogen but also increase hydrogen uptake and release kinetics as compared with the materials that are solid. Overall purpose of this research is to explore the feasibility of creating such a nano-porous hydrogen-storage material using the following approach.

(a) Create a nano-porous silica based template with interconnected three dimensional networks of channels on a metallic substrate (most preferably a zeolite, to coat a base metal).

(b) Electrochemically grow the metal alloy (suitable for hydrogen storage) into the ceramic nano pores by using the base metal as a cathode and metal alloy as an anode by electro-deposition.

(c) Dissolve the ceramic template in basic solution to yield the metal alloy grid.

This research will specifically target the task “a” above, that of creating a nano-porous silica based template coating on a metallic substrate. Zeolites with pore size in the range 0.3 – 1.5 nm, such as faujasite or silicalite will be employed. Mesoporous silica (3-5 nm pore diameter) is another potential candidate for such application and will be investigated.

Second purpose of this research is to develop nano-porous membranes to be used as templates for nano-wire fabrication and also for filtering applications. This research will specifically target development of 60 - 100 µm thick nano-porous alumina membranes with uniformly distributed pores of size 50 - 100 nm. Anodized alumina is important for this study since this material can be used both as a substrate for zeolite growth and also as a template for metallic growth inside the pores. The nano-structured metallic alloy material would be of great importance for hydrogen storage.

1.1.1 Organization of Dissertation

This work is primarily composed of two research activities:

(a) Porous alumino-silicates and electro-deposition of metal into their pores – Characterization for growth and presence of metal in the pores

(b) Nano-porous alumina membranes - Fabrication and statistical characterization using image analysis techniques.

Each major chapter will deal these two activities as sub-sections. Results and discussion and conclusions are presented in chapters 3 and 4 followed by proposed future work and bibliography.

1.2 Micro-porous Alumino-Silicates – Growth on Metallic and Non-metallic Substrates

Sections 1.3 thru 1.4 will describe:

(a) Porous alumino-silicates and their crystalline structure and their growth on substrates

(b) Growth mechanism involved.

1.3 Growth of Porous Alumino-Silicates

Porous alumino-silicates used in our study can be classified into two groups:

(a) Zeolites: Faujasite and silicalite

(b) Mesoporous silica

Zeolites are hydrated alumino-silicates with a porous structure composed of silica (SiO_4) and alumina (AlO_4) tetrahedra sharing all corners with each other. The porous structure of a synthetic zeolite usually accommodates a wide variety of cations which are usually alkali, alkaline earth or rare earth cations, as well as organic cations. These cations are rather loosely bound to the framework and can be exchanged which makes them good ion-exchange beds for use in industrial and commercial applications. Zeolite templates with pore size in the range 0.3 – 1.5 nm, such as faujasite, silicalite and mesoporous silica have been used in this study. Faujasite has a three dimensional pore structure with pores running perpendicular to each other in the x, y and z planes. Framework structure of faujasite with a pore size of 0.74 nm is shown in Figure 1 [1].

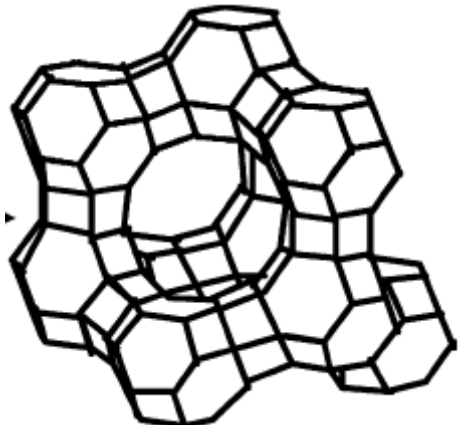

Figure 1 Framework structure of faujasite

Silicalite is the pure siliceous form of ZSM-5 type of zeolites. Figure 2 shows typical framework of microstructure of silicalite with perpendicularly arranged zigzag channels in the size range 6 A^0 x 6 A^0 [2].

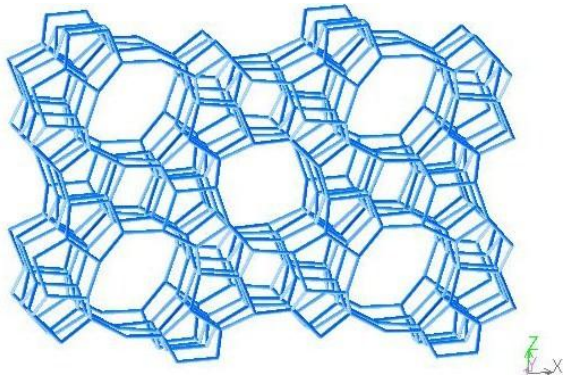

Figure 2 Framework structure of silicalite

Mesoporous silica belongs to MCM-41 class of materials. It has arrays of non-intersecting hexagonal channels with high surface area. Figure 3 shows the lamellar structure of mesoporous silica composed of hexagonal micellar rods with silica condensed in between these pore channels [3].

Figure 3 Lamellar structure of mesoporous silica

Conventionally zeolites have been grown on various kinds of supports. Various metallic and non-metallic supports used for zeolite growth are shown in Table I.

Metals	Composites	Single crystals
Aluminum, silicon, titanium, copper, nickel, stainless steel, gold, platinum	Cordierite, mullite and mica	Quartz, rutile and Sapphire

Table I Supports used for zeolite crystallization

Free standing zeolite membranes can be obtained by using a sacrificial support as substrate for zeolitic growth. Sano et al. [4] have used filter paper to promote zeolite growth at 170^{o}C. The filter paper was later burnt out at 500^{o}C resulting in a free standing zeolite. Davis et al. [5] reported the growth of zeolite Na-Y (aka Faujasite) on different metal substrates including copper, silver, platinum, titanium,

molybdenum, iron and tin. Continuous polycrystalline MFI crystals of size range 50 μ – 80 μ have been grown by Geus et al. [6] on porous ceramic/clay supports and they were reported to be thermally stable up to 400^{o}C.

The substrates that we have used can be classified as metallic and non-metallic substrates. Metallic substrates used were sintered copper, anodized titanium, sodium hydroxide treated titanium, and anodized aluminum. Non-metallic substrates used for zeolitic film growth were commercial anodic alumina Anodisc® and laboratory synthesized alumina.

1.3.1 In-Situ Hydrothermal Synthesis and Film Growth

In-situ hydrothermal synthesis of a clear solution containing a silica source, an aluminum source and an alkali source results in crystallizing zeolites. Hydrothermal synthesis is a process of carrying out the reaction chemistry at elevated temperatures and pressures. During crystallization in hydrothermal synthesis, the zeolite crystals that form are inter-grown; this results in the formation of a continuous film. Structure of zeolites during crystallization of ZSM-5 is determined by organic template molecules which are also known as structural directing agents (SDA). Commonly used template ions are (TMA^{+}) Trimethyl Ammonium and (TPA^{+}) Tetrapropyl Ammonium. The template molecule is later burnt off by calcination, heating the sample at high temperature in air for a certain length of time followed by cooling to room temperature. Industrially synthesized aluminum rich zeolites [X, Y, A, L etc] have a crystal size ranging from 100 nm – 10 μm.

Magdalena Lassinantti[7] has discussed three routes to synthesize zeolites:

(a) *In-situ* crystallization or direct crystallization – The substrate is treated with the zeolite precursor solution hydrothermally during synthesis. Synthesis of a zeolite film is a function of nucleation and crystal growth on the substrate. Many types of zeolites including faujasite and silicalite can be synthesized by this method.

(b) Vapor phase transport method – Zeolites are crystallized in the presence of a dry alumino-silicate amorphous gel under the vapors of the reacting ingredients. This method has been used to synthesize various kinds of zeolites such as MFI, MOR.

(c) Seed film method – Seed crystals are attached to the surface of the support which act as growth centers for crystallization. Zeolite Y, Zeolite A and Faujasite membranes have been grown on supports using this method.

The third method is generally referred to as the seed film method and is a very well established technique for growing polycrystalline zeolite layers on supports. Here the substrate was positively charged using a cationic polymer. Negatively charged seed crystals were then adsorbed onto the surface which acted as nucleation sites for zeolite crystallization and growth. Hedlund et al. [8] have also described a seed film method to grow thin silicalite-1 films on silicon wafers with thickness varying from 80 nm to 800 nm. Gossens et al. [9] have schematically described the direct crystallization and seed film method as shown in Figures 4 and 5.

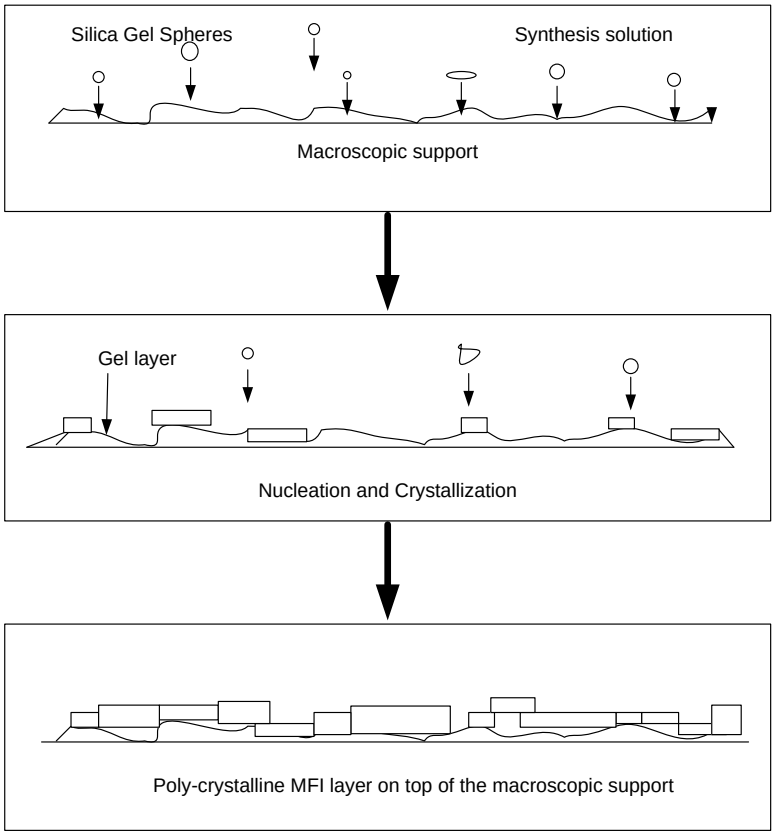

Figure 4 *In-situ* crystallization of zeolites on substrates

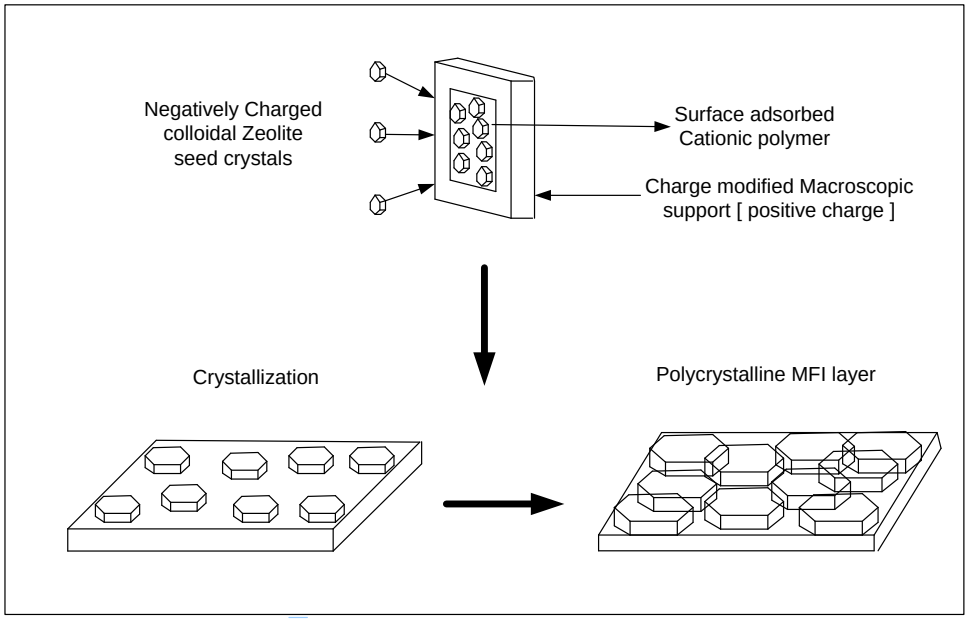

Figure 5 Seed film method

1.3.2 Nucleation, Crystallization and Film Growth

The various reaction steps involved in the formation of zeolite film on a support during hydrothermal synthesis include self-organization at the molecular scale, nucleation, agglomeration, crystallization and inter growth into a film. Jansen et al. [10] have studied the growth of MFI crystals on silicon substrate to describe the crystallization and film growth mechanism.

The process of crystallization is envisioned to be occurring mainly due to the presence of a homogenous gel layer on the surface of the macroscopic support during hydrothermal synthesis. Initially small globular shaped fast growing crystals are formed as gel spheres. Nucleation is believed to occur at the gel/liquid interface as has been suggested by the presence of loose crystallites in the top layer of the gel. Crystallization then proceeds into the gel layer and forms an intergrown polycrystalline zeolite film.

1.3.3 Mechanism of Crystal Growth on Macroscopic Support

The macroscopic supports get oxidized and form hydroxyl groups on the surface which are protruding into the synthesis solution during hydrothermal synthesis. The zeolite growth is expected to start via condensation mechanism thus resulting in a firm chemical bonding of the zeolite crystals with the surface.

Kaschiev et al. [11] studied the growth of silicalite on silicon to record the various events that occur *in-situ*. The observation of crystallization *in-situ* and evaluation using elemental analysis and infrared radiation has led the authors to describe the process as a series of sequential events as shown in figure 6.

(i) Large gel spheres are formed in the reaction mixture during the synthesis.

(ii) Crystallization starts at the gel/liquid interface and later on proceeds into the gel.

(iii) With time the gel layer gets consumed and the crystal growth rate decreases

(iv) Crystals form with increased dimensions

(v) Layer by layer growth leads to a polycrystalline layer

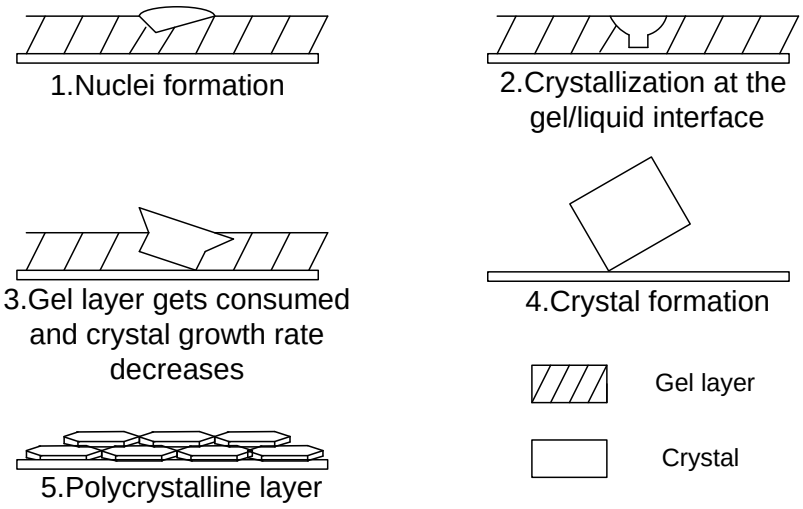

Figure 6 Crystallization of silicalite on silicon substrate

The reaction mixture is believed to have two nutrient pools near the substrate/gel/liquid interface. The gel layer is believed to be rich in SiO_2 and the liquid has TPA or the structure directing molecule. The gel phase diminishes with time as the crystal grows and the crystal growth rate decreases with time. The crystallites which are oriented parallel to both the nutrient pools have the fastest growth rate. Chemical bonding occurs between surface hydroxyl groups of the substrate and the (OH) groups of the crystals formed due to condensation. The crystals thus deposit onto the substrate and intergrow with good surface bonding resulting in a polycrystalline layer.

1.3.4 Film Growth Mechanisms after Zeolite Crystallization on the Surface

Four growth modes for homogeneous zeolite film growth on substrates, as shown in figure 7, have been discussed by Kaschiev et al [11]. These are layer, island, layer and island, and continuous growth modes. The layer mode involves growth of the layer by the spreading of one or few mono-atomic layers. This kind of growth is mediated by nucleation with building up of one monolayer upon another. Island growth occurs by the nucleation and growth of separate island like crystallites of varying multi-atomic height.

Layer and island growth mode incorporates both the island and the layer mode as the name suggests. The growth mechanism occurs first by building up of one or more mono layers. This is then followed by the formation of island-like crystallites on top of the preformed mono layers.

Continuous growth mode covers the substrate by random and simultaneous filling of the surface by several crystallite mono layers. This growth process differs from the layer mode in that the former is not nucleation mediated.

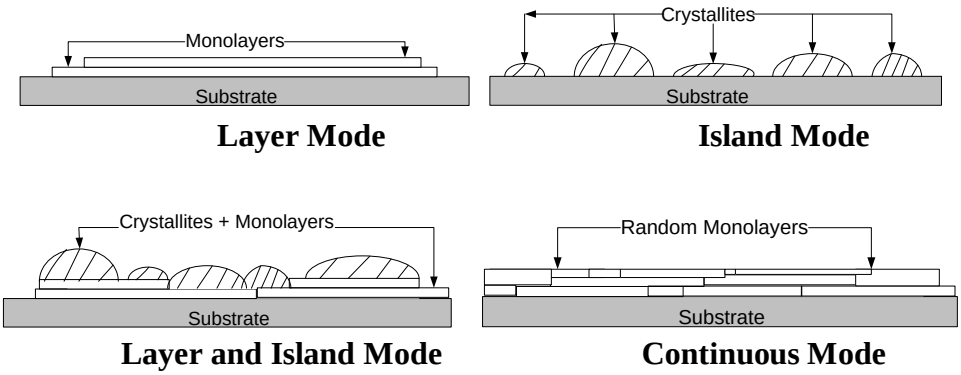

Figure 7 Film growth modes

The continuous growth results in films with low degree of crystallinity even though the layers are polycrystalline and are found to cover the substrate well in many cases. In the island mode the crystallites develop grain boundaries between and around them in the film and are polycrystalline. However, since the growth is not uniform in the form of homogeneous crystalline layers, the purpose of coating is not served well. The layer mode is the most favorable growth process which can result in thin films for membrane and catalyst applications.

The study done by Kaschiev et al. [11] also describes the growth mechanism of zeolites in the form of poly layers on substrate. The bare membrane is smooth at a microscopic level, free of any screw dislocations. The surface of the substrate has nucleation sites due to adsorbed molecules or edge dislocations. Growth occurs by the building up of layer filling, each one filling on top of an already deposited layer of thickness equal to or greater than a mono atomic layer as shown in figure 8. The number of layers deposited and the continuous film growth process are functions of the growth conditions and the film/substrate system.

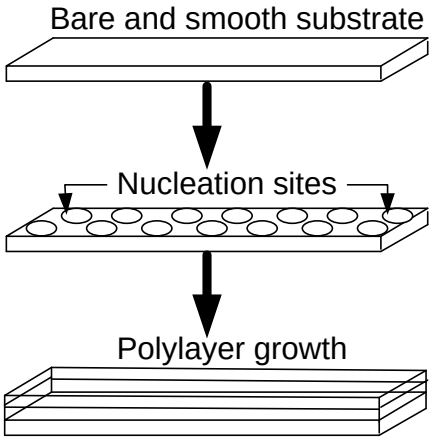

Figure 8 Poly-layer film growth

Gossens et al. [9] have described the intergrowth mechanisms of zeolite film formation. Polytypism and epitaxy are the two kinds of intergrowth mechanisms proposed for phase-pure zeolites. Polytypism is the most common intergrowth mechanism in zeolites. It is envisioned as occurring in each individual crystals by stacking of the various structurally uniform domains without any mismatch of the bonds. In case of MFI and FAU type zeolites, the periodicity with which the stacking occurs is due to an alternative bonding sequence of a common sheet. Epitaxy involves the oriented overgrowth of one zeolite phase upon other. This kind of overgrowth leads to materials which change composition across the interface. One example of epitaxial overgrowth involved seeding the synthesis mixture of zeolite X with zeolite A which resulted in the epitaxial overgrowth of the former.

1.3.5 Effects of Synthesis Parameters on Film Growth, Membrane Thickness, and Crystal Orientation

Film growth was found to be a function of various synthesis parameters. Many studies have been done in this area to investigate the effect on film growth rate, membrane thickness and crystal orientation. Magdalena Lassinantti [7] has examined the effects of time, repeated hydrothermal synthesis and temperature on supported zeolitic deposition.

1.3.5.1 Effect of Synthesis Time on Microstructure of Zeolite Formed

Increasing the time of hydrothermal synthesis for faujasite led to the conversion of zeolite X into Zeolite P. The crystal structure of the zeolite formed was needle like indicating the formation of a different p-type zeolite.

1.3.5.2 Effect of Repeated Hydrothermal Synthesis on Crystalline Films

Repeated hydrothermal synthesis results in the formation of uniform and densely packed zeolite layers on supports. Fresh synthesis solution was added periodically to the cleaned samples and it was found that the film growth rate was higher for the repeated synthesis as compared to the one-step synthesis. Repeated hydrothermal synthesis was also found to increase film thickness as compared to the conventional one-step synthesis.

1.3.5.3 Effect of Synthesis Time and Temperature on Film Thickness

Film thickness was found to be linearly proportional to the time and temperature of hydrothermal synthesis. Film thickness was found to increase with increase in time of synthesis. However, a maximum film thickness always existed and further synthesis resulted in a different zeolite phase as in the case of faujasite converting to zeolite P.

1.3.5.4 Effect of Reactant Concentrations on Zeolite Film Growth

The effects of different concentrations of various synthesis parameters like silica precursor [TEOS], organic template [TPA^+], hydroxide [TPAOH], dilution and temperature on the growth, membrane thickness and orientation of the MFI type zeolites grown on seeded substrates including porous glass and alumina have been investigated by Wong et al. [12] in their study. This study involves growth of MFI membranes on supports using the pre- seeding method. Porous vycor tube with a uniform pore structure of 5 nm was employed as the support for seeded MFI membrane growth.

(a) Effect of Silica precursor [TEOS] on film growth:

For a fixed amount of TPAOH in the synthesis solution, the growth rate was found to increase montonically (strictly increasing) with increase in the silica precursor, with slow increase in the lower concentration regions of the silica precursor. XRD intensities showed that (1 0 1) peak intensity increased with increase in TEOS concentration. This indicated that zeolite film grew preferentially in the < 1 0 1 > direction. Crystallinity of the zeolite film was much better for the higher silica precursor concentrations.

(b) Effect of Organic template [TPAOH] on film growth:

Film growth rate increased with increasing concentration of TPAOH and reached an optimum value beyond which the growth rate either stayed constant or decreased with further addition of TPAOH. Alkalinity was found to have a much stronger influence on film growth and crystallinity than TPA^+ concentration. The growth rate and (1 0 1) intensity increased to a certain optimum value and further increase resulted in poor film growth and crystallinity.

(c) Effect of Dilution on film growth:

Film growth and crystallinity decreases with increasing dilution of the solutions for a constant [TEOS] / [TPAOH] ratio. However, the film growth is very slow for highly concentrated solutions because of their high alkalinity and results in the etching of the substrate and dissolution of the zeolite also.

(d) Effect of Hydrothermal synthesis temperature:

Growth rate of the film increased exponentially with increase in temperature based on Arrhenius law:

$$k = A * e^{\frac{-E_a}{RT}}$$

In conclusion this study has showed that seeding the support results in faster film growth and protects the substrate from getting etched at higher solution concentrations.

Toshikazu et al. [13] have studied the effect of synthesis parameters such as stirring time, drying and heating temperatures on the orientation of MFI crystals. Jansen et al. [10] have shown that for low temperature and low silicon concentration the silicalite crystals grow with the long axis perpendicular to the substrate and for high silicon concentration the crystals grow with their long axis parallel to the substrate.

1.3.5.5 Effect of Pre-treating the Substrate on Film Growth

Zeolites (ZSM – 5 and silicalite) were formed on carbon membranes at 120^{o}C. Prior to hydrothermal synthesis carbon membranes were oxidized, TEOS (Tetra-ethoxy silane) adsorbed and heat treated by Smith et al [14]. This resulted in good adhesion and growth of ZSM – 5 and/or silicalite. In a study done by Bratton et al [15] it was shown that mechanical treatment of the substrate would result in much denser films as compared to the substrates which were not mechanically treated. Metal substrates plastically deformed were found to support growth of dense films as opposed to pure metals and/or alloys with low surface tension which did not produce such dense films.

1.3.5.6 Effect of pH on Crystal Structure

Cheng et al. [16] have shown in their study of silicalite deposition on α-Alumina that the nature of the films deposited is a function of the pH of the synthesis medium. Highly alkaline media resulted in films which do not strongly adhere to the support. In contrast, low alkaline media deposited strongly adhering dense films. This has been attributed to the nature of nucleation which changes with pH of the sol. In a highly alkaline medium zeolite film does not grow until homogenous nucleation is observed where as in the case of a low alkaline medium, heterogeneous nucleation leads to crystallization. One possible way of depositing thick zeolite coatings on ceramic supports is to perform repeated hydrothermal synthesis.

1.4 Mesoporous Silica

Mesoporous silica materials have applications as catalyst supports and shape and/or size selective adsorbents because of their large surface area which is of the order of 1000 m^2/g. These materials usually have pore sizes in the range of 2 – 10 nm depending on the synthesis procedure [17, 18, 19].

1.4.1 Formation of Mesoporous Silica

Mesoporous silica has been reported to be formed due to a liquid templating mechanism. Figure 9 shows the schematic of the mechanism involved in the formation of mesoporous channels as reported by Beck et al. [3]. The templating mechanism is based on the ionic interaction and the hydrogen bonding between surfactant micelles and silicates, which lead to self organization into an ordered array of mesostructures. Hexagonal arrays of cylindrical micelles are formed in the solution, and silicate species occupy the spaces between the cylinders. The targeted mesoporous structures are obtained by burn out of organic templates. Mesoporous silica has found great utility as catalysts and sorption media because of the regular arrays of uniform channels. Larger surface area is desired for enhancing of the reactions.

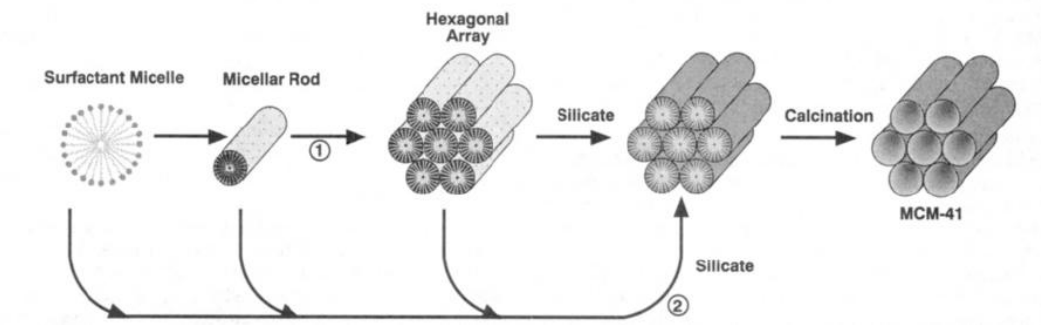

Figure 9 Liquid crystal templating mechanism – formation of mesoporous silica

1.4.2 Mesoporous Silica Growth on Substrates

Mesoporous silica has been reported to be synthesized in various structural forms depending on the synthesis procedure involved. Yang et al. [20] reported forming sphere-like mesoporous silica under acidic conditions. Huo et al. [21] reported forming hard mesospheres of silica using surfactant stabilized emulsion based synthesis chemistry. Mesoporous silica has also been grown as fibers by Yang et al. [22], Huo et al. [23] and Bruinsma et al. [24]. These fibers have prominent applications as high surface area materials. However, the most interesting properties of mesoporous silica as catalyst supports and adsorbents can be realized by depositing mesopore channels aligning as semi-cylindrical assemblies on the substrate. Figure 10 shows the assembly mechanism for forming micellar channels on the surface of a substrate [25].

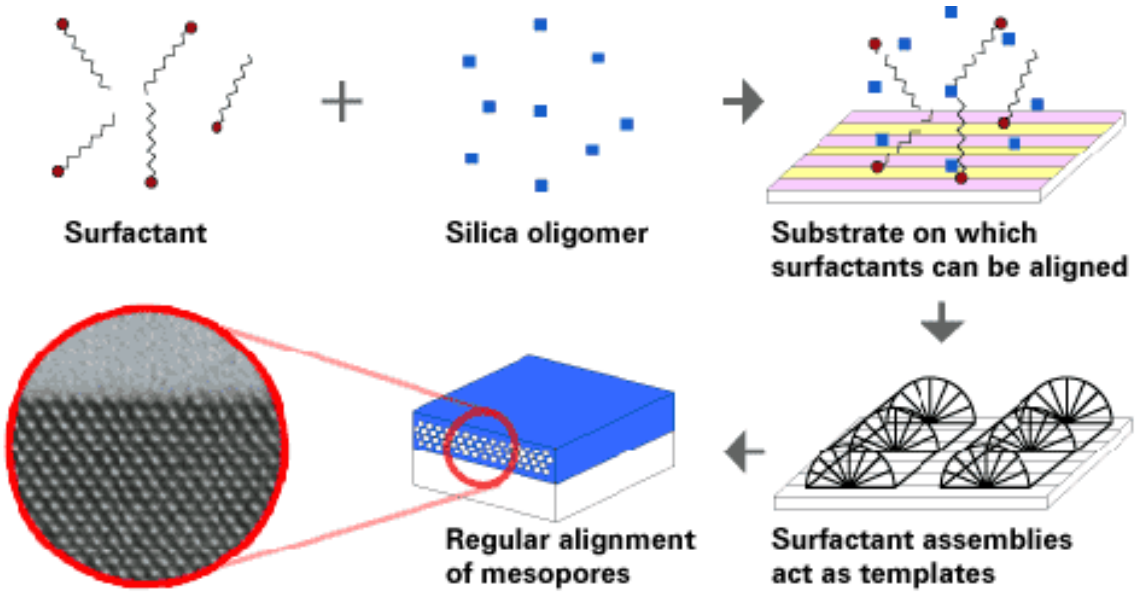

Figure 10 Alignment of mesopores using surface deposition

Ogawa et al. [26, 27, 28, 29, 30] have reported mesoporous silica deposition using the process of spin coating. Studies done by groups such as Yang et al. [31, 32, 33, 34, 35, 36], Aksay et al. [37], Tolbert et al. [38] and Schacht et al. [39] have demonstrated that the mesoporous silica film deposition occurs due to nucleation of micellar structures and silica condensation on the surface forming the mesopore channels. Surfactant molecules used in the synthesis of MCM-41 can affect the size of mesopores. Increasing the chain length of the surfactant molecule produces materials with bigger pores. Swelling the surfactant assembly by the use of an organic additive such as tri-methyl-benzene can also yield bigger pores.

1.5 Nano-porous Alumina Membranes – Fabrication

Section 1.6 of this chapter will describe:

(a) Applications and unique self-organized structure of alumina material

(b) Techniques of fabricating alumina membrane materials with thru thickness cylindrical pore channels.

(c) These materials were to be used as templates for the fabrication of nano-wires.

1.6 Nano-porous Anodic Alumina

Porous anodic alumina template is a self-ordered nano-channel array material with densely packed hexagonal porous structure. Anodic oxidation of aluminum results in a nano-porous oxide layer which has found diverse and important applications in various areas which include prevention of corrosion of automobile and aerospace structures, electronic, optical, magnetic devices, sensors and micro reactors [40, 41, 42, 43]. Meng et al. [44] used porous Alumina as a template to fabricate highly ordered nickel nano-wire arrays for high density magnetic storage. Nickel nano-wire arrays with 100 nm spacing achieved data density storage values of 75 Gb/in^2 which was an improvement from 70 Gb/in^2 for conventional cobalt alloy thin film media.

Aluminum oxide is usually formed by the anodization of aluminum in weak electrolytic acids such as sulphuric, oxalic and phosphoric acid. Nano-porous alumina is characterized by its pore morphology parameters such as pore size, pore spacing and wall thickness. These parameters can be adjusted by varying the experimental anodization conditions [45, 46, 47]. Yufei et al. [48] reported fabrication of large pore size in the macro porous range. Anodic alumina is of importance to our study since

this material can be used both as a substrate for zeolite growth and also as a template for metallic growth inside the pores which will yield a nano-structured material important for potential hydrogen storage applications.

1.6.1 Anodization of Aluminum

The following steps are performed in sequence to obtain nano-porous alumina, using pure (99.99%) aluminum as the starting material:

(i) Mechanical and electro polishing

(ii) Anodization of aluminum

(iii) Aluminum metal etching to obtain alumina

(iv) Barrier layer opening to obtain alumina with thru holes

1.6.2 Pretreatment – Degreasing and Electro-polishing

The most widely used pretreatment before anodization of alumina includes a degreasing step to remove oil and any impurities on the surface. The aluminum sample is then mechanically polished to obtain a smooth and clean metallic surface, followed by a controlled electro-polishing of the aluminum surface in a mixture of an acid, usually perchloric acid, ethanol and water. The degreased sample is placed in an electrolytic bath with aluminum as the anode and a counter electrode which is inert to the electrolyte involved. A small pulse of voltage is then applied for a short time which is usually a function of the current density to achieve a surface which is flat and uniform on the microscopic level. During this stage a preferential etching of hills yields a smooth surface as shown schematically in Figure 11. The resistance at A is less than that at C, because the resistance film is thinner; the current at A is therefore

larger than that at C, resulting in faster metal dissolution at A-B than at C-D. Well electro-polished aluminum surface was very smooth and defect-free as opposed to the non-electro-polished samples which developed pitting on the surface.

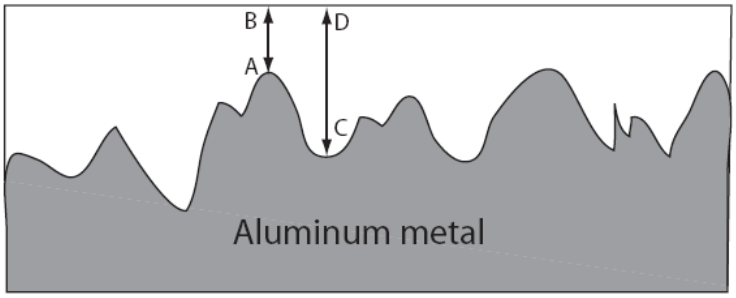

Figure 11 Microscopic aluminum surface

1.6.3 Anodization–Mechanism

Anodization of aluminum is carried out in an electrochemical cell with aluminum as the anode and any conducting material inert to the electrolyte as the cathode. Various electrolytes, mostly acidic, have been found to produce uniform porous alumina structure. Oxalic acid, phosphoric acid and sulphuric acid have been used as electrolyte. The cathode is a plate or rod of platinum, carbon, lead, stainless steel, nickel etc. which is inert to the electrolyte used. The electrochemical set up for anodization of aluminum using a DC power supply is shown in Figure 12.

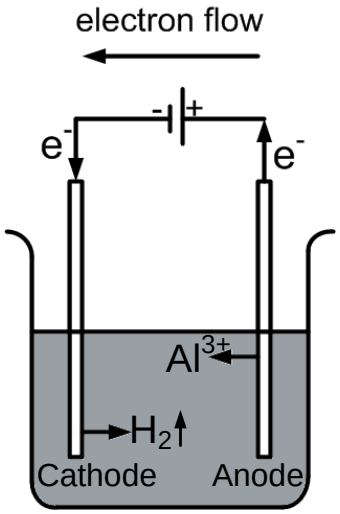

Figure 12 Electrochemical setup of aluminum anodization

The reactions involved during anodization of aluminum are as follows:

Oxidation near the anode

$$2Al \rightarrow 2Al^{3+} + 6e^{-} \quad (1)$$

$$2Al^{3+} + 3H_2O \rightarrow Al_2O_3 + 6H^{+} \quad (2)$$

Hydrogen gas evolution near cathode

$$6H^{+} + 6e^{-} \rightarrow 3H_2 \quad (3)$$

Overall Alumina formation reaction

$$2Al + 3H_2O \rightarrow Al_2O_3 + 3H_2 \quad (4)$$

During anodization aluminum undergoes oxidation getting converted into aluminum cations (Al^{3+}), and releasing 3 electrons for each oxidizing aluminum atom. The aluminum cations then react with water in the aqueous electrolyte resulting in the formation of alumina. The hydrogen gas is released at the cathode. Alumina thus obtained has base metal on the bottom and also a thinner oxide layer known as the 'barrier layer' which is the collection of pore-ends in the form of 'caps'. The base

aluminum metal can then be chemically dissolved in a saturated $HgCl_2$ or $CuCl_2$ solution [49] to obtain nano-porous alumina membranes. Alumina layer has also been reported to have been detached using a voltage reversal technique where the polarities for the cathode and the anode were switched after an initial anodization step. Anodizing with reversed polarities for a time period of 12 – 24 hrs resulted in detachment of the alumina layer from the base metal [50]. The alumina layer thus obtained has pore openings on one side with pore caps on the other end. Pore caps can be opened by chemical treatment in 5 wt% H_3PO_4 for about 90 minutes resulting in porous alumina with through holes [51, 52, 53]. The schematic process is shown in Figure 13. The time required for complete pore cap opening increases with increase in pore diameter and barrier layer thickness as shown in table II.

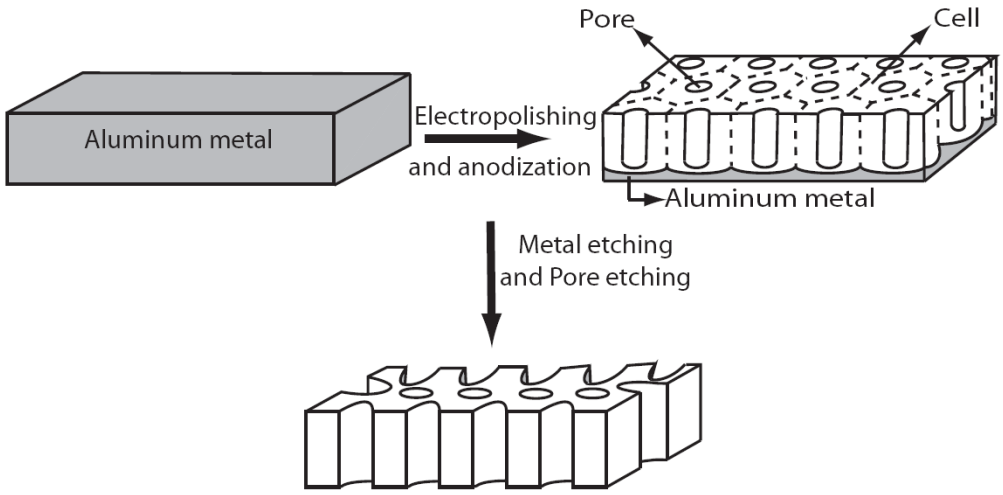

Figure 13 Fabrication of porous anodic alumina

Anodization voltage (V)	Time of acid treatment (min)
25	23
40	75
50	85

Table II Time required for complete pore cap opening at various voltages

1.6.4 Alumina Formation in Various Electrolytes at Different Voltages

1.6.4.1 Aluminum Oxidation in 0.3 M Oxalic Acid

Masuda et al. [54] have done pioneering work to produce self-organized nano-porous anodic alumina with large domains of uniformly shaped and spaced pores. Aluminum (99.99% pure) was anodized in 0.3M oxalic acid at a constant voltage of 40V. Highly ordered nano-hole arrays of platinum and gold were fabricated using anodic alumina membrane as a template. The porous alumina was later dissolved using 10 wt% NaOH to obtain the nano-porous metallic porous structure. For a constant voltage more ordered cell configuration occurred with longer anodization times. Anodization at 40 V produced close to ideal hexagonal honeycomb structure with great regularity. Longer anodization time periods resulted in defect/dislocation free surface morphology of the alumina template. Metal was deposited into the pores of alumina by electroless deposition. Alumina layer was then dissolved using 10 wt% NaOH to obtain the highly ordered metal nano-hole array as shown in figure 14.

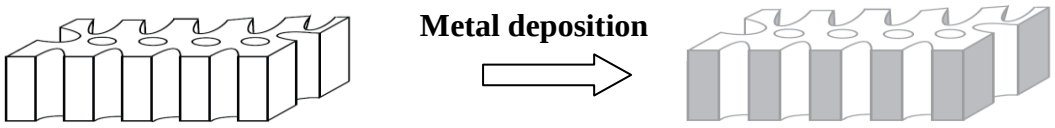

Figure 14 Fabrication of metallic nano-hole arrays

1.6.4.2 Aluminum Oxidation in 0.3 M Sulfuric Acid

Masuda et al [55] also used sulfuric acid to fabricate highly ordered porous alumina. Anodization was carried out in 0.3 M sulfuric acid at a constant potential in a range of 20 – 27 V. Here also the ordering of the cell arrangement was found to be voltage dependent; the best quality anodization was achieved between 25 to 27 V.

Self-ordering of pores occurred at 40V in oxalic acid; in sulfuric acid it occurred between 25 V- 27 V. Other anodizing conditions such as concentration of the electrolyte and temperature were not found to influence self-ordering for anodization in sulfuric acid. Thickness of the alumina membrane was found to increase with anodization time. Since pore ordering occurred at a lower voltage in sulfuric acid as compared to oxalic acid this also resulted in pores of much smaller dimensions in sulfuric acid.

1.6.5 Growth Mechanism of Alumina Pores

The conditions for self-organized formation of hexagonal arrays of pores in aluminum oxide have been investigated by Jessensky et al. [56] in oxalic acid and sulfuric acid. The steady-state pore growth kinetics in alumina maintains equilibrium between field-enhanced oxide dissolution at the oxide/electrolyte interface and oxide growth at the metal/oxide interface. The oxide layer always grows perpendicular to the surface of the metal with the pore walls growing upwards. A volume expansion,

about twice the original volume, occurs during aluminum anodization. Jessensky et al. [56] have proposed development of repulsive forces between the neighboring pores resulting from the volume expansion induced mechanical stresses in the oxide layer. Since the overall thickness of the alumina layer that forms is a function of the anodizing voltage and electrolyte composition, these processing variables also influence the extent of this mechanical stress resulting in varying pore-size and spacing distributions.

1.6.6 Optimum Growth Conditions for Alumina

Ordering of pores in domains of 1 -5 μm in size is usually observed in anodized alumina disks [57]. This domain size was reported to increase with increase in anodization time and change in concentration of electrolyte [58]. The arrangement of pores in these domains was found to be a function of the growing voltage; 40 V produced the best polycrystalline hexagonal ordering of pores on the surface for oxidation in 0.3M oxalic acid. A different set of anodization conditions have been found to hold for 20 wt% sulfuric acid. The range of anodization voltages was 18 – 25 V and the anodizing current was found to be 4 times higher in the case of oxalic acid. Optimum conditions for self-organized pore growth of alumina in oxalic acid and sulfuric acid have been established. Table III lists the optimum growth conditions for anodization of aluminum in sulfuric and oxalic acid and the corresponding inter-pore distance [50].

Electrolyte	Voltage (V)	Pore spacing (nm)
Sulfuric Acid	25	63
Oxalic Acid	40	100

Table III Optimum growth conditions in sulfuric and oxalic acid

The best results for pore growth were found at moderate volume expansion which occurs at moderate forming voltage and current efficiency. These conditions were 40 V for 0.3 M oxalic acid and 18.7 V for 20 wt% sulfuric acid.

1.6.7 Free Standing Alumina Membranes with Thru Hole Morphology

Free-standing porous alumina membranes have been fabricated by Schneider et al [59] with through-hole morphology which have a high flexibility and large area. The sequential steps involved in this process include:

(a) Self-assembly of the pores into highly ordered hexagonal cell configuration by anodization.

(b) Detachment of alumina layer from the base metal by voltage reversal technique without employing any chemical etching techniques

(c) The obtained pre-structured base metal was then anodized to obtain a homogeneously uniform alumina membrane which was again separated from the aluminum metal by the voltage reversal technique.

(d) The alumina membrane thus obtained after a two-step anodizing technique was chemically etched in phosphoric acid to open the pore bottoms at the barrier layer to obtain a membrane with through holes.

Voltage reversal technique was reported to provide a much uniform surface with large ordered domains of alumina pores compared to the non-uniform regions obtained by chemical etching.

CHAPTER II

EXPERIMENTAL METHODS AND TECHNIQUES

2.1 Alumino-Silicates – Growth on Metallic and Non-metallic Substrates

Sections 2.2 thru 2.6 of chapter 2 will describe:

(a) Experimental method for fabricating porous alumino-silicate coatings on metallic and non-metallic substrates and electrochemically growing metal into the pores.

(b) Subsequent characterization of these coatings for uniform growth and evidence for the presence of metal after electro-deposition.

2.2 Initial Experiments and *in-situ* Hydrothermal Synthesis

Initial experiments for metal growth in a zeolite template involved compacting lab-synthesized and Cu exchanged faujasite powder on a nickel mesh as the electrode for electro-deposition. Copper was then electrodeposited into this specimen. The subsequent EDAX and HRTEM examination of these films showed presence of copper as shown in figure 15. However, this approach caused de-lamination of the

mechanically forced-in zeolite layer from the nickel substrate due to hydrogen evolution during electroplating process.

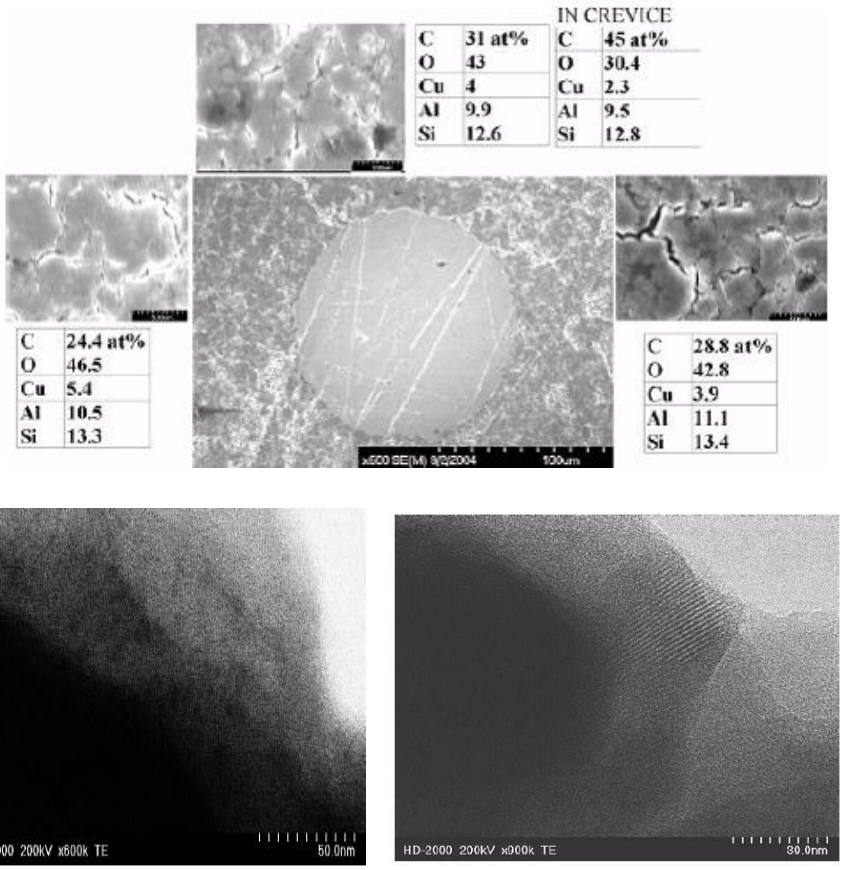

Faujasite before copper growth **Faujasite after copper growth**

Figure 15 EDAX and HRTEM of copper in faujasite micro-pores

2.3 Micro-scale Roughening of Metallic Substrates

Direct in-situ hydrothermal synthesis is another route to grow zeolite layer on various substrates, involving nucleation and crystal growth on the surface of the support in the presence of a precursor solution. This process was pursued with an aim to prevent the film detachment mentioned above. It was also proposed that micro scale "roughening" of the metal surface would result in microscopic features on the

surface which may serve as nucleation sites for zeolite and thus provide better adhesion between the zeolite film and the metal substrate.

2.3.1 Sintered Copper

To achieve micro-scale roughening copper particles in size range 53µ - 75µ were sintered on a bare copper foil at a temperature of 1020^0C (Figure 16). These particles have voids in the size range of 50 µ.

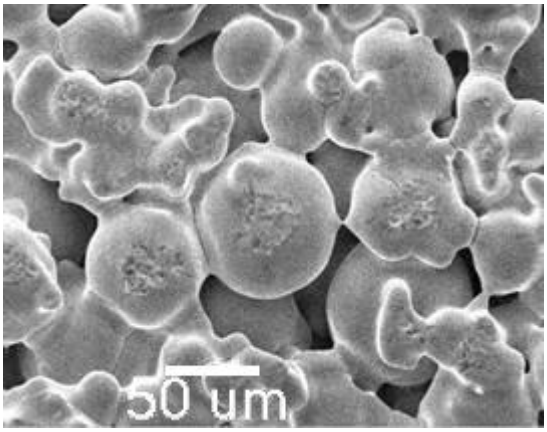

Figure 16 Sintered copper surface

2.3.2 Anodized/NaOH Treated Titanium

Titanium alloy was anodized and heat treated to develop an oxide layer with porous structure on the surface to help and support nucleation of the silicalite crystals. Titanium was anodized in 0.5 wt% HF at 20V for 45min using titanium as both anode and the cathode. This was followed by heating the sample to 500^0C in air at slow temperature increments. It was soaked at this temperature for 2 hrs and then cooled to room temperature. This resulted in a very uniformly distributed porous structure of about 50 nm dimension (figure 17) on the titanium surface. The other kind of treatment involved NaOH exposure at 60^0C for 24 hrs, oven drying at 40^0C followed

by heating up to 500^{o}C. This also produced a uniform nano-textured oxide surface layer on the surface of titanium, as shown in figure 17.

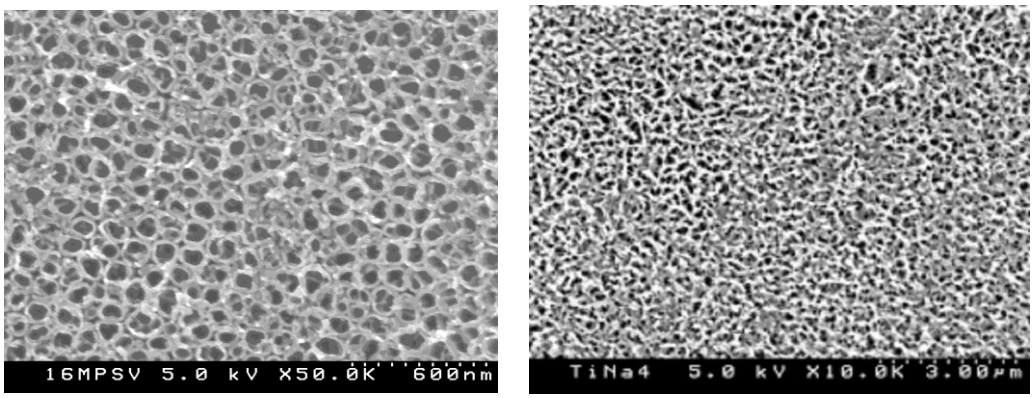

Anodized Titanium **NaOH treated Titanium**

Figure 17 Anodized and NaOH treated Titanium

2.4 *In-Situ* Growth of Zeolites on Metal Cathodes

Anodized titanium, NaOH treated titanium and sintered copper were used as substrates for deposition of silicalite and faujasite. These silicalite and faujasite layers were examined for their suitability as nano-porous templates for electro-deposition of nano-scale metal grid. The various zeolites used in the study and the metallic substrates involved are shown in figure 18.

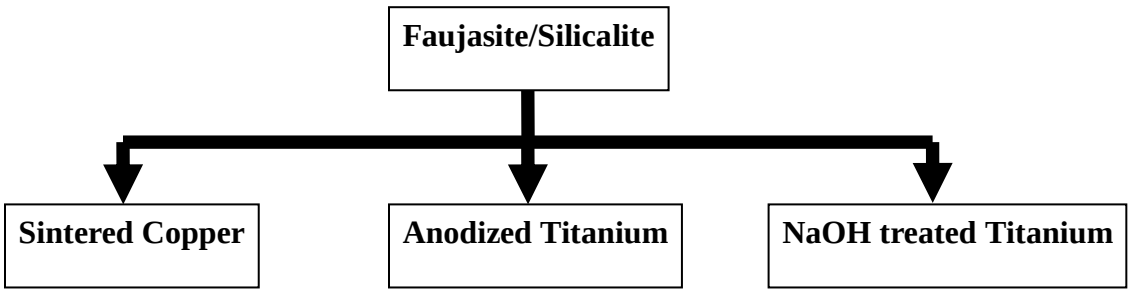

Figure 18 Metallic Substrates and zeolite growth

2.4.1 Zeolite Reaction Chemistry

Faujasite was synthesized in the lab using the following reaction chemistry –

Oxide molar ratio – 378 SiO_2:100Al_2O_3:507 Na_2O:18500 H_2O [60].

The mixing weights of the water, silica, alumina precursor and sodium salt were calculated using the above oxide molar ratio:

40 wt% colloidal silica: $NaAlO_2$: 50 wt% NaOH: H_2O – 13.84g: 4.0g: 17.0g: 64g.

Total amount of water was divided into three equal volumes – v1, v2 and v3

(a) NaOH (Sigma Aldrich, NaOH 50% solution in water) was dissolved in volume "v1" of distilled water and this mixture was stirred until a clear solution was obtained.

(b) In a separate container $NaAlO_2$ was added to volume "v2" of water and this mixture was stirred until a clear solution was obtained.

(c) The base solution from (a) was added to the $NaAlO_2$ solution and they were mixed.

(d) Colloidal silica (DuPont, 40 wt% colloidal silica in water) was diluted in the remaining volume "v3" of water in a teflon vessel to avoid etching of glass by silica and this was added to the mixture of NaOH and $NaAlO_2$.

(e) The reaction mixture obtained was aged for about 8.5 hrs at room temperature and then was transferred into a reaction vessel and was heated at 100^0C for up to 10 hrs under normal gravity conditions to obtain faujasite.

Micro-scale roughened substrates were placed in the reaction chemistry for growing the template on the metal surface.

Silicalite crystals were synthesized using the reaction chemistry with an oxide molar ratio of 100 SiO_2: 7.5 TPABr: 9.6 NaOH: 3291 H_2O [60]. Mixing weights were calculated using the above molar ratio:

40 wt% colloidal silica: TPABr: 50 wt% NaOH: H_2O – 19.50g: 2.6g: 1.0g: 65g.

Total amount of water was divided into three equal volumes – v1, v2 and v3.

(a) Sodium hydroxide (Sigma Aldrich, NaOH 50% solution in water) was dissolved in a volume "v1" of distilled water and mixture was stirred until a clear solution was obtained.

(b) In a separate container TPABr (Tri-propyl Ammonium Bromide – Fischer Scientific 99% purity) was added to volume "v2" of distilled water and mixture was stirred until a clear solution was obtained.

(c) The base solution from (a) was then added to the TPABr solution and they were mixed.

(d) Colloidal silica was diluted in the rest of the water, volume "v3", in a teflon vessel to avoid etching of glass by silica and this was added to the mixture of NaOH and TPABr.

(e) The reaction mixture obtained was transferred into a reaction vessel with a Teflon liner and was heated to 170^0C for up to 72 hrs under normal gravity conditions to obtain silicalite. Metallic substrates were placed vertically inside stainless steel autoclaves with teflon liners to get a silicalite coating.

2.5 Mesoporous Silica Growth on Metallic and Non-metallic Substrates

Mesoporous silica (MPS) have 1-4 nm tunable pores and 1-2 nm pore walls with an approximate porosity of 70-80%. Considerable effort was devoted to synthesize MPS and to fine tune film growth on cathode metals.

MPS has several advantages over Faujasite and silicalite for our study:

1. MPS materials can be grown with very large aspect ratios, which should aid thicker film growth on the cathode.
2. MPS materials tend to agglomerate into parallel bundles, which should aid the uniformity parallel to the surface on the cathode.
3. The porosity is higher which would result in a denser metallic growth into the pores of the mesoporous silica.
4. The surfactant can be removed chemically to open the nano-pores, avoiding high temperature calcinations, which result in cracking of the deposited film by thermal stress.
5. The synthesis conditions are milder and require less expensive chemicals.

Mesoporous silica materials are synthesized in aqueous solutions using surfactants. The surfactants form tubular micelles on which silica is condensed. The surfactant can then be removed leaving a highly porous material. The surfactant can be removed either by calcinations at high temperature (>500^{o}C), or by dissolution using solvents at room temperature. The alkane chain length of the surfactant controls the pore diameter range of 1-4 nm. The synthesis conditions are mild, some even at room temperature, although 120 C synthesis route was used in our experiments. The pore structure of MPS is one-dimensional arranged in hexagonally coordinated

bundles, but impurities in solutions result in irregularities in the final product often resulting in three-dimensional connectivity.

2.5.1 Synthesis of Mesoporous Silica

Mesoporous silica was synthesized based on the study of Michael Kruk et al [61]. Mixing weights used were:

Distilled water: CTMABr: sodium silicalite – 150g: 6.57 g: 5.5 g

(a) An aqueous solution of sodium silicate with Na/Si = 0.5 (2.4 wt % Na_2O, 9.2 wt % SiO_2, 88.4 wt % H_2O) and an aqueous solution of surfactant (cetyl tri-methyl ammonium bromide) were prepared. Initially 150 cc of distilled water was mixed with 6.57 grams of CTMABr and stirred mildly for 10 minutes.

(b) Then, 5.5 g of sodium silicate (14 wt% NaOH, 27 wt% SiO_2) was added drop by drop while ultrasonically zapping the mixture at room temperature for 1 hour.

(c) Synthesis was performed for 24 hrs around 115-120^o C at a pressure of 8 – 12 psi.

(d) The mixtures after heating were cooled to the same temperatures as before the initial mixing and pH of the mixture was adjusted to 10.86 by adding acetic acid (CH_3COOH).

2.5.2 Mesoporous Silica Deposition

The following metallic and non-metallic substrates have been used for mesoporous silica growth:

Metallic – (a) sintered copper (b) Anodized Titanium (c) Anodized Aluminum

Non-Metallic – Commercially procured Anodisc®

The process of metallic growth and stripping the metal from the mesoporous silica has utilized the following steps:

1. Micro-structuring of metal cathode,
2. In-situ growth of MPS,
3. Removal of surfactant by chemical wash at room temperature,
4. Metal electrochemical growth in the nano-pores, and
5. Removal of silica matrix

Sintered copper and anodized titanium were fabricated as described earlier. Anodized aluminum was used in our study due to the virtue of its self-ordered and densely packed highly porous cylindrical arrays. Pure aluminum electrochemically anodized in 0.3M oxalic acid at 40 V shows a nano-porous microstructure on the surface as shown in Figure 19.

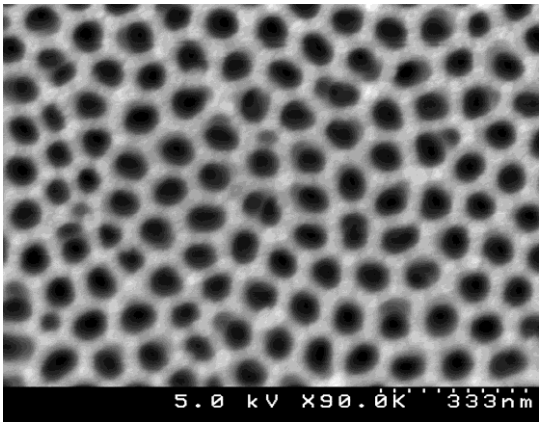

Figure 19 Nano-porous Alumina

2.6 Commercial Alumina – Anodisc®

Anodisc is a commercially available alumina membrane procured from Whatman International. These membranes have 1-dimensional pores with pore diameter of 200 nm. These membranes are stand-alone membranes with a thickness of about 60 μ. They are being used here for MPS growth since they have through-thickness cylindrical pores where MPS can grow and deposit.

2.7 Nano-porous Alumina Membranes – Fabrication and Characterization

Sections 2.8 thru 2.10 of chapter 2 describe the experimental methods for the following:

(a) Fabrication of porous anodic alumina membranes using polycrystalline aluminum.

(b) Statistical analysis of pore morphology of alumina to determine pore size, inter-pore spacing, pore distribution and pore ordering

2.8 Laboratory – Synthesized Anodic Alumina

We have observed that the commercially available alumina membrane pore channels develop smaller branches which are non-uniform and multi-dimensional. Hence we have taken up the task of developing an alumina membrane with uniform pore cylinders in one dimension.

2.9 Poly-Crystalline Anodic Alumina – PCAA - Fabrication of Free Standing Porous Alumina Membranes with Thru Porosity

2.9.1 Anodization of Pure Alumina to form Porous Aluminum Oxide Templates with Thru Porosity

Free-standing porous alumina membranes have been fabricated by anodic oxidation of polycrystalline aluminum. The various steps involved in fabricating porous alumina materials are mechanical polishing, electro-polishing, metal dissolution and barrier layer dissolution.

2.9.2 Mechanical Polishing of Aluminum

High purity aluminum metal (99.999%) was used as the starting material for fabricating porous anodic alumina materials. Polycrystalline aluminum material has been acquired from Fisher scientific and this material will be referred to as PCA for all purposes in this work. PCA was mechanically polished using emery paper of various grit sizes ranging from 80 to 1200 under running cold water.

2.9.3 Electro-polishing of Aluminum

Electro-polishing of aluminum was performed to develop an alumina surface which is very flat and uniform on the microscopic level. A small pulse of voltage is passed through the sample in an electrolytic mixture of 109.5 ml ethanol, 20.85 ml water and 20.25 ml perchloric acid at 6.5^0C using platinum as the cathode in an electrochemical cell at a current density higher than 500 mA/cm^2 for a short period of time to create a microscopically smooth polished surface. The electro-polished aluminum has a mirror finish with a microstructure composed of concaves which act

as ‘dimples’ or random sites for nucleation of pores on the surface of the aluminum metal during anodization. Electro-polished aluminum was stored in distilled water to minimize the amount of surface oxidation in air soon after it was removed from the electrochemical bath. We have noticed that samples which were electro-polished without mechanical polishing tend to corrode along the edges and dissolve into the electrolyte.

2.9.4 Anodization

Anodization of the aluminum was performed for 24 hrs using the electro-polished aluminum as the anode and platinum as the cathode in an electrolyte solution of 0.3M oxalic acid at 7^{o}C. During the anodization process aluminum converts to alumina oxide. Real-time current data was acquired using a multimeter with a pc-interface. A digital multimeter (Radioshack - PC Interface 46-Range Digital Multimeter) with a RGB interface has been connected to the electrochemical cell in series to record the anodization current data as a function of time. The frequency of sampling can be controlled from the multimeter. We have used sampling frequency of 1 sec and 5 sec. A screenshot of Meter View 1.0 used for real-time data acquisition is shown in the Figure 20. Figures 21 and 22 show typical anodization current behavior of aluminum with time. The sample was anodized; removed from the electrochemical bath and washed with distilled water. Anodized alumina at this stage is present in the form of a porous surface oxide on the aluminum metal.

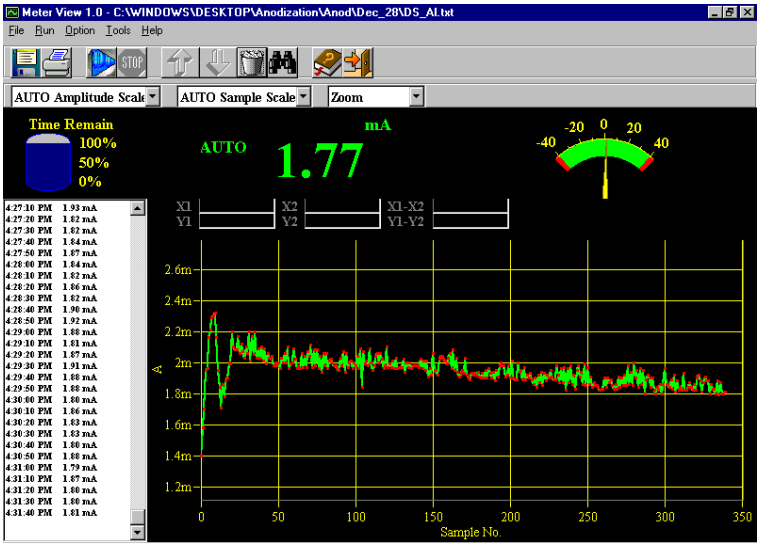

Figure 20 Anodization current density acquisition using Meterview 1.0

2.9.5 Current Density Transients - Polycrystalline Aluminum Anodization at 40V

The current density transient for polycrystalline aluminum anodization shown in Figures 21 and 22 follows the typical trend reported in the literature. The current initially reaches a peak and then decreases to a minimum value; it then stabilizes to a steady state value from there on. Typical peak and steady state current density values for anodization of polycrystalline aluminum are shown in table IV. The stable current density regime involves formation of pore channels as oxide forms and dissolves simultaneously with an established equilibrium.

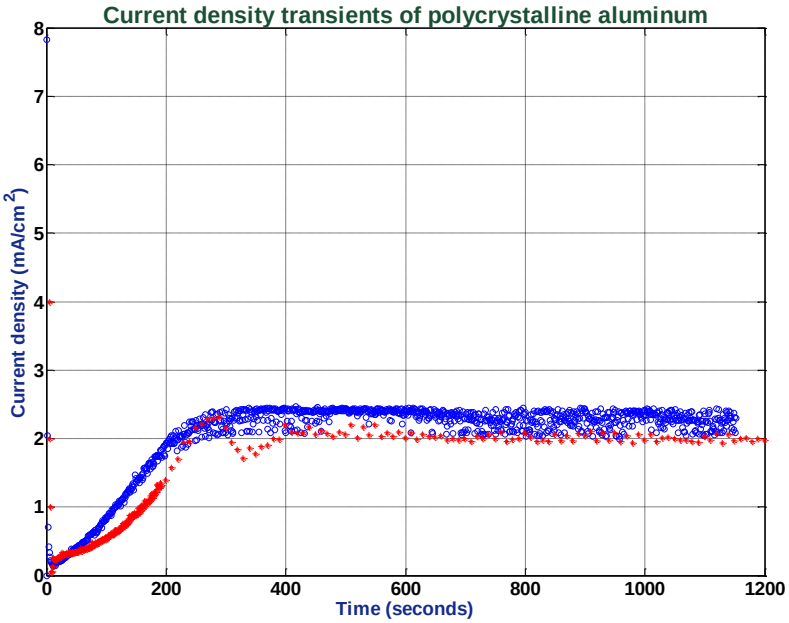

Figure 21 Short time current density transients of polycrystalline alumina

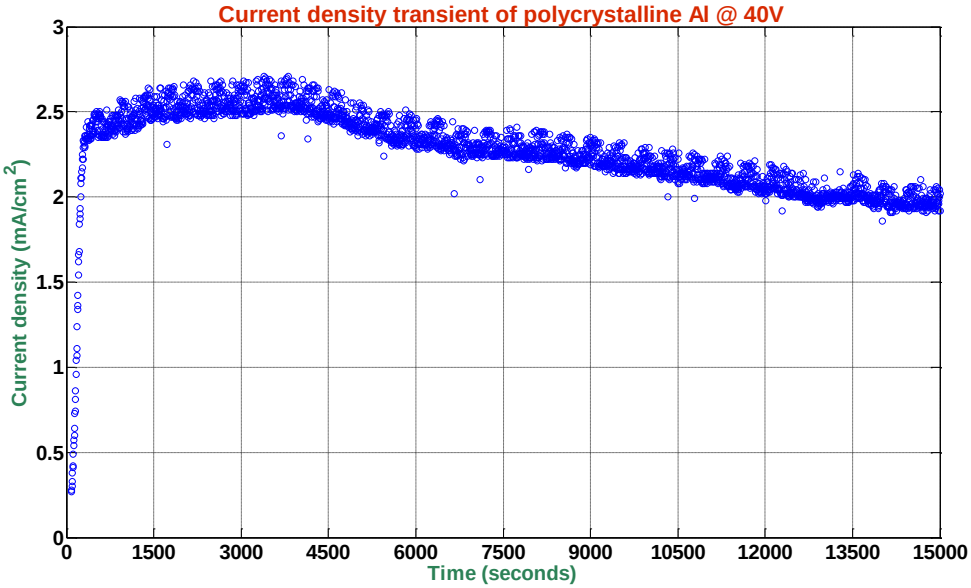

Figure 22 Long-time current density transients of polycrystalline alumina

Sample ID	Peak Current (mA)	Steady State Current (mA)
PCAA-01	7.83	2.2
PCAA-02	4	1.8

Table IV Peak and steady-state current density values

2.9.6 Experimental Setup for Anodization of Aluminum

Anodization was performed by packing the electro-polished aluminum in a PFA reducing union during anodization (Figure 23). The PFA reducing union held the aluminum disc inside. The main advantage of using a reducing union was that there were no leakage problems of any sort during anodization. The back side of the aluminum disc also was protected all the time.

Aluminum disc of ½" diameter (12.7 mm) shown in figure 24 was mechanically polished and then electro-polished before transferring to the PFA union. Fine metallic wool was used to contact the aluminum disc from its back side to the anode. Aluminum disc packed in the PFA union was used as anode with platinum as cathode in an electrochemical cell shown in Figure 25. Anodization was carried out in 0.3 M oxalic acid at 40 V under potentio-static conditions (constant voltage) and 7^{o}C for 24 hrs to obtain polycrystalline anodic alumina.

Figure 23 PFA fitting

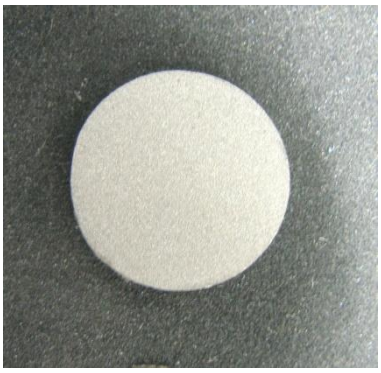

Figure 24 Mechanically polished aluminum disc

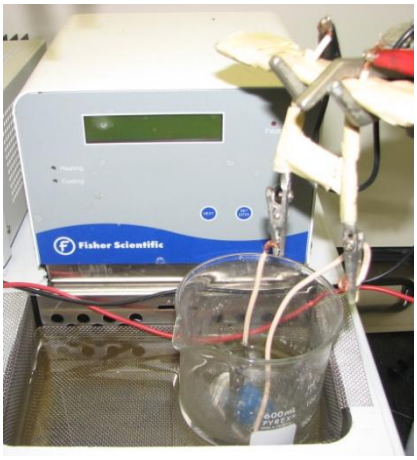

Figure 25 Electrochemical set-up for anodization of aluminum

2.9.7 Aluminum Oxide Retrieval by Metal Dissolution

Alumina or aluminum oxide fabricated from poly crystalline aluminum (PCA) will be referred to as PCAA (poly-crystalline anodic alumina). PCAA formed after anodization was detached from the aluminum metal using chemical etching in a mixture of copper chloride and HCl (100 gms of 37 wt% HCl, 270 gms of H_2O and 13.38 gms of $CuCl_2$).

Copper precipitates via an exothermic reaction as porous metal on the surface of the oxide during the chemical treatment process. We have noticed that if this precipitated metal is not washed off during the process of metal etching it tends to deposit as impurities on the surface of the membrane. Hence we have incorporated the process of ultrasonically washing the membrane while holding the sample vertically using tweezers. The membrane was intermittently removed and washed to remove excess deposits of copper. The metal dissolution occurs with gas evolution at the metal and oxide interface; the gas evolution (bubbling) stops once all the aluminum metal is consumed and copper precipitated. The membrane is then removed and carefully washed in distilled water in an ultrasonic bath. This membrane material is a free standing aluminum oxide film with open pores on one side and closed caps on the other side where metal/oxide interface existed before aluminum metal dissolution.

2.9.8 Pore Cap Barrier Layer Dissolution Using Chemical Treatment

The cap side of the above obtained alumina has a thin barrier layer oxide which needs to be dissolved and opened-up to produce through thickness pore channels. Our initial experiments involved barrier layer dissolution by attaching the membrane

obtained after metal dissolution on a glass surface. The membrane was affixed such that the pore side was contacting the glass surface. The cap side or the barrier layer side was facing upwards and this surface was exposed to 5 wt% H_3PO_4 for a time of about 90 minutes. The barrier layer on the pore caps start to open up at 60 minutes and majority of the pore caps opened for a time of treatment at 85 minutes a shown in figure 26. The barrier layer completely dissolved after between 90 minutes to 120 minutes. Star like regions appeared on the surface after 120 minutes, while 90 minute treatment yielded good open pores as shown in figure 27.

However initial problems with membrane cap opening and retrieval from a glass slide included lift-off from the glass surface and surface cracking over large dimensions as shown in the figure 28. The other problem associated with this technique was that the membrane could not be obtained as a clean and complete intact membrane since small portions of the membrane were found to break and detach from the membrane. This could be possibly due to the expansion of the alumina membrane affixed to the glass slide during pore cap opening as the weak acid penetrated through the pore caps and dissolved the barrier layer. Hence we have adapted the technique of physically holding the membrane vertically using tweezers while chemically exposing the membrane to the 5 wt% phosphoric acid.

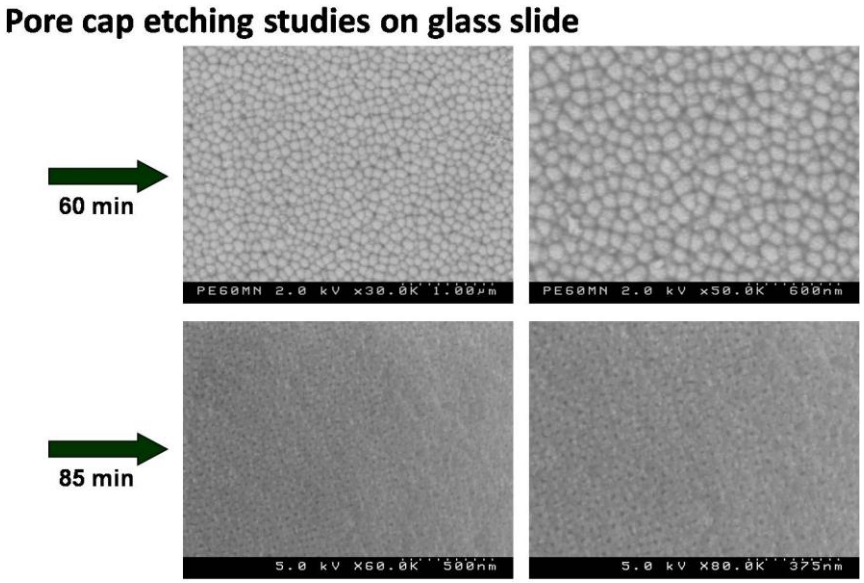

Figure 26 Barrier layer dissolution at 60 minutes and 85 minutes

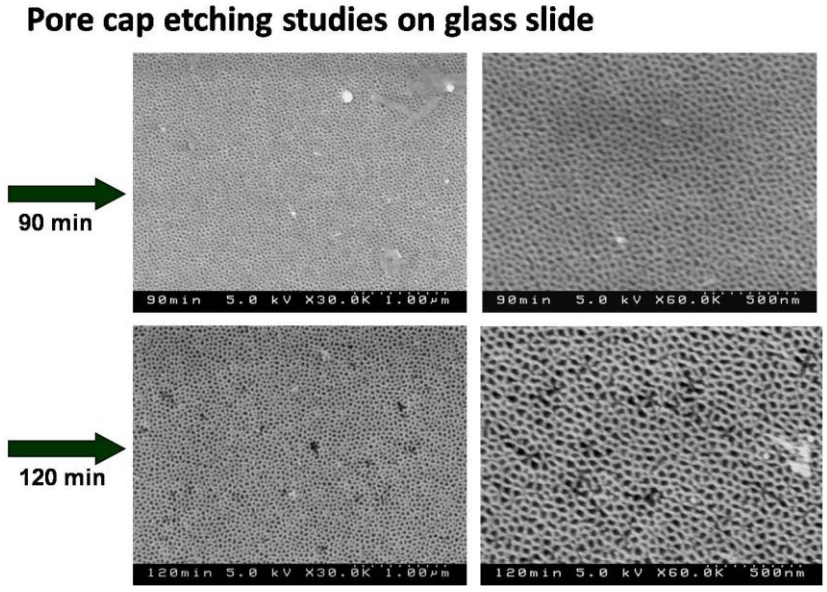

Figure 27 Barrier layer dissolution at 90 minutes and 120 minutes

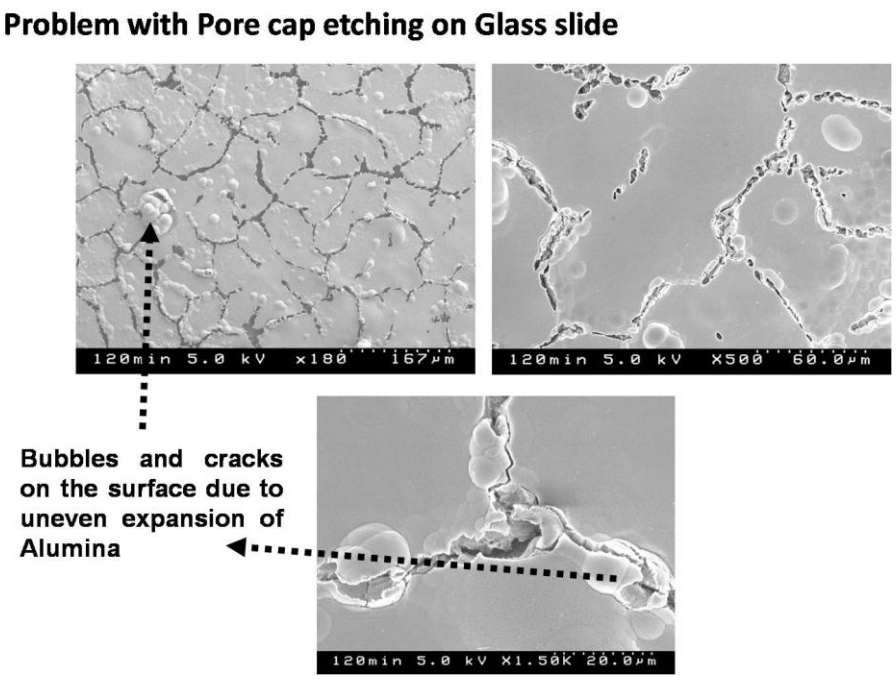

Figure 28 Problems with pore cap opening with membrane on the glass slide

2.9.9 Successful Pore Cap Opening Using Wet Chemical Etching while Protecting the Pore Side

When left un-protected on the pore side of the membrane during the barrier layer dissolution using 5 wt% H_3PO_4 the pore structure was damaged; the channels coalesced to form bundles which resulted in 'macro porosity' rather than 'micro porosity' as shown in figure 29. A protective layer was required to cover the pore side of the PCAA which had to possess the following characteristics:

(a) Non-invasive and non-reactive to the pore structure

(b) Uniform coating to completely cover the surface of the template material

(c) Easily removable after barrier layer dissolution leaving no traces on the surface

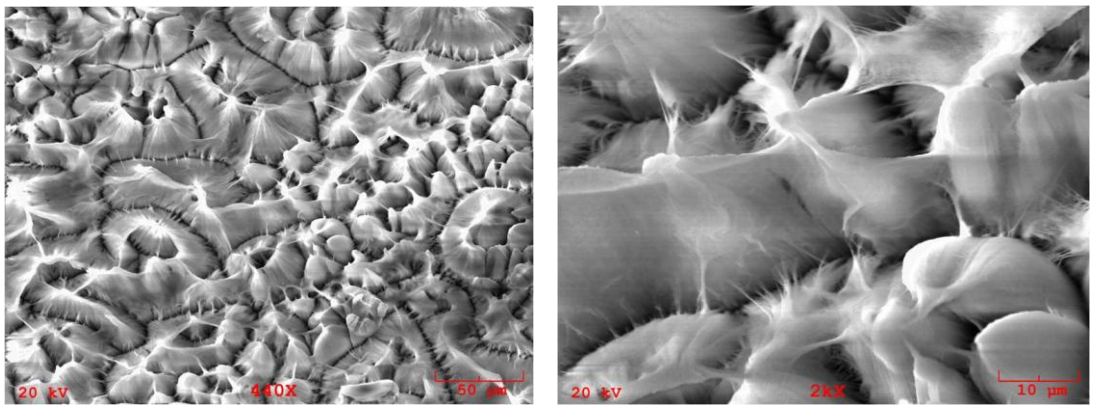

Figure 29 Un-protected pore structure of PCAA damaged after exposure to 5 wt% H_3PO_4

After experimenting with different kinds of organic and resin coatings we have found Silver paint (Ag particles suspension in acetone – SPI Supplies® brand conductive silver paint) to satisfy (a) through (c) above. After coating PCAA on the pore side using silver paint the template material was allowed to air dry for 1 hour. After air-drying the barrier layer was dissolved by chemically exposing to 5 wt% H_3PO_4. After barrier layer dissolution, silver paint on the pore side was washed off ultrasonically using acetone followed by subsequent washing steps with DI water. Successful PCAA with thru-porosity, i.e open and intact pore structure on both sides of the membrane material were thus obtained, as shown in figure 30.

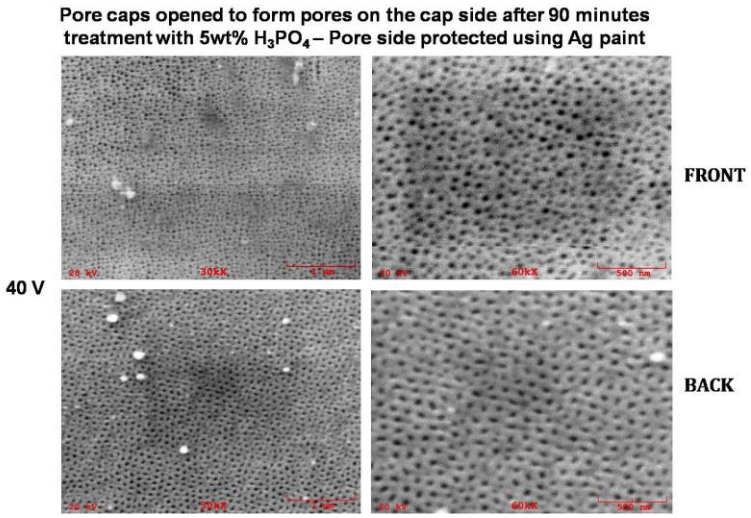

Figure 30 Successful pore cap opening while pore side was protected using Ag paint

2.9.10 Summary of Experimental Anodization Conditions

A summary of experimental conditions used in the various processes to fabricate free standing porous alumina templates is shown in table V

Anodization sub-process	**Electrolytic mixture**	**Temperature**
Electro-polishing	20.25 ml Perchloric acid	6.5°C
	20.85 ml water	
	109.5 ml Ethanol	
Anodization	0.3 M oxalic acid	7.0° C
Al Metal dissolution	100 g of 37 wt% HCl	25°C
	270 g of water	(Room temperature)
	13.38 g of $CuCl_2$	
Barrier layer dissolution	5 wt% H_3PO_4	25°C
		(Room temperature)

Table V Summary of experimental conditions – Fabrication of free standing PCAA

2.10 Micro-structural Characterization Using Electronic Image Analysis and Statistical Tools

Since the efficiency of a PCAA template for nano-device fabrication depends largely on the uniformity of pore characteristics, such as their size, inter-pore spacing and their ordering these parameters were characterized by using statistical image analysis techniques. Sigmascan-pro from SPSS Inc was used to locate and record the pore center of mass coordinates cm(x, y) on SEM images of the pore-side/ and cap-side surface of these membranes. Pore spacing was determined from the minimum-spanning-tree (MST) analysis and the number of nearest pore neighbors was determined by using voronoi polygon analysis. Nearest neighbor spacing was also determined using the center of mass coordinates.

2.10.1 Minimum Spanning Tree (MST) and VORONOI Polygon Mapping Using IDL and Sigmascan Pro

2.10.1.1 Obtaining cm(x) and cm(y) from SEM Micrograph Images:

The SEM image of a typical alumina membrane as shown in figure 31 was first edited in a software such as Paint-Shop-Pro to eliminate irrelevant materials, such as, micron markers etc from the image. The length of the micron markers was used to obtain the “pixel” to “nm” conversion factor for these images before removing the micron-markers from the image. Figure 31 after removing the micron marker would look like figure 32.

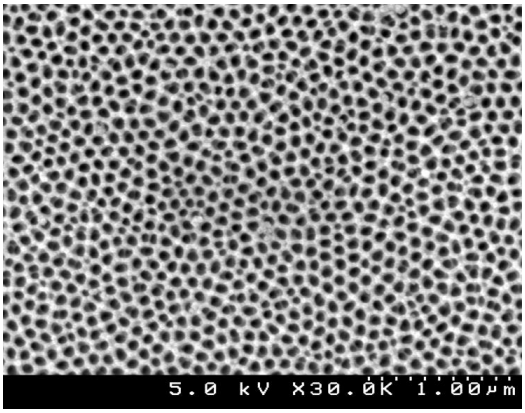

Figure 31 SEM image of a PCAA fabricated at 40V in 0.3 M oxalic acid

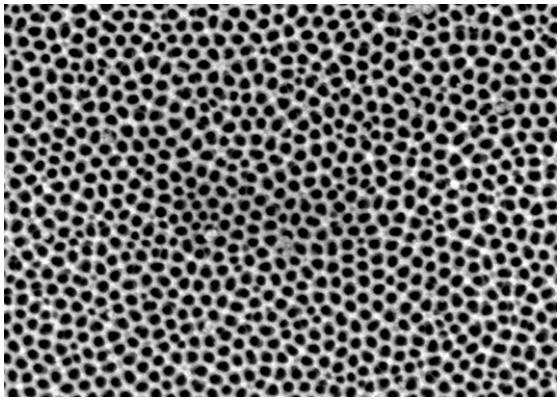

Figure 32 SEM image after removing the micron marker

After the micron marker is removed from the SEM image, care must be taken that there are no broken features or artifacts such as disjoined pores in this case as this may lead to incorrectly identifying two regular pores as one large pore. Analysis can be done by first opening the .TIF or .BMP file in Sigmascan Pro and then using the intensity threshold feature. The beginning and the ending intensities can be specified to place an overlay of a certain color on the image which will result in filling the desired features. This is a trial and error procedure and the user can experiment with varying ending intensities until all the features of interest are overlaid with the specified color overlay. Figure 33 is a typical snapshot of image from figure 32 analyzed in Sigmscan Pro. After Intensity filling step the user would go to: *File-*

>SaveAll which would save the analyzed image and the overlay as a file with '.ov1' extension. The Sigmascan pro can then be used to open this overlay file and analyze it to obtain the cm(x, y) data and also the areas of the features. It is important to specify the characteristics to be measured using the Measurement settings in Sigmascan pro. Typical measurement features of interest are binary cm(x, y), area and shape factor. Mean pore diameter can be obtained by calculating the area of the shaded portion in the overlay and number of features obtained from the analysis using Sigmascan pro.

Once these features have been specified to be measured, the "Count Objects" button on Sigmascan pro shown by the green arrow in figure 34 can be clicked on which would result in a feature count and measuring the specified characteristics displayed in a separate spreadsheet obtained as output shown in figure 35.

The cm(x, y) obtained from the Sigmascan pro 5 are saved as a text file in ASCII format which will later be used as input into the IDL program platform to create the MST diagrams and VORONOI polygons.

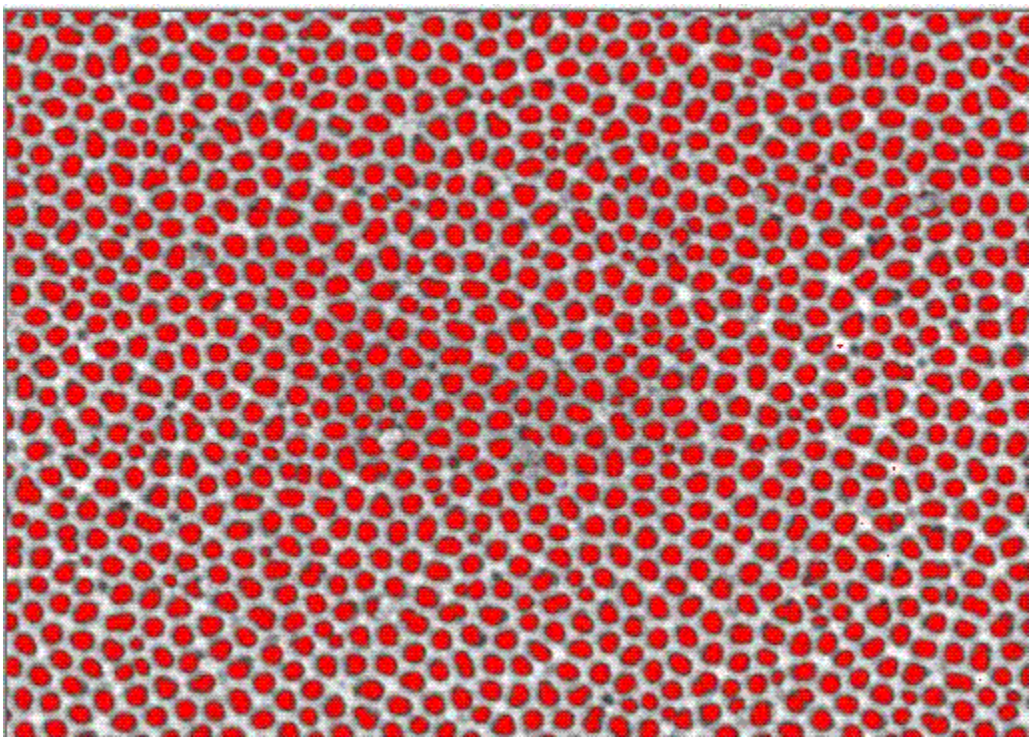

Figure 33 Snapshot of a SEM image filled with an overlay of red color

Figure 34 'Measure objects' button in Sigmscan pro

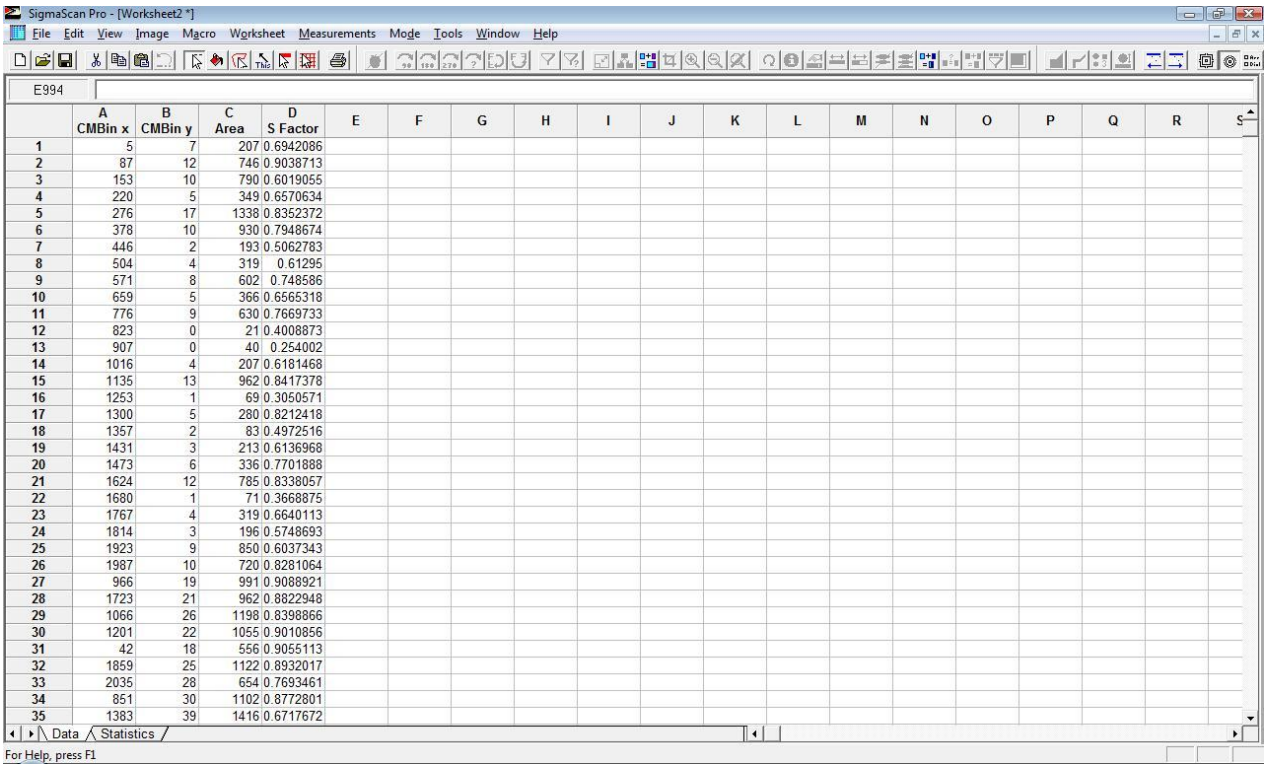
SigmaScan Pro - [Worksheet2 *]

File Edit View Image Macro Worksheet Measurements Mode Tools Window Help

E994

	A CMBin x	B CMBin y	C Area	D S Factor	E	F	G	H	I	J	K	L	M	N	O	P	Q	R	S
1	5	7	207	0.6942086															
2	87	12	746	0.9038713															
3	153	10	790	0.6019055															
4	220	5	349	0.6570634															
5	276	17	1338	0.8352372															
6	378	10	930	0.7948674															
7	446	2	193	0.5062783															
8	504	4	319	0.61295															
9	571	8	602	0.748586															
10	659	5	366	0.6565318															
11	776	9	630	0.7669733															
12	823	0	21	0.4008873															
13	907	0	40	0.254002															
14	1016	4	207	0.6181468															
15	1135	13	962	0.8417378															
16	1253	1	69	0.3050571															
17	1300	5	280	0.8212418															
18	1357	2	83	0.4972516															
19	1431	3	213	0.6136968															
20	1473	6	336	0.7701888															
21	1624	12	785	0.8338057															
22	1680	1	71	0.3668875															
23	1767	4	319	0.6640113															
24	1814	3	196	0.5748693															
25	1923	9	850	0.6037343															
26	1987	10	720	0.8281064															
27	966	19	991	0.9088921															
28	1723	21	962	0.8822948															
29	1066	26	1198	0.8398866															
30	1201	22	1055	0.9010856															
31	42	18	556	0.9055113															
32	1859	25	1122	0.8932017															
33	2035	28	654	0.7693461															
34	851	30	1102	0.8772801															
35	1383	39	1416	0.6717672															

Data Statistics

For Help, press F1

Figure 35 Output from Sigmscan pro after counting the objects

2.10.1.2 Obtaining the MST and VORONOI Polygons

Construction of a minimum spanning tree begins by selecting a point and joining it to its nearest neighbor. This forms the first branch of the tree. Points that are nearest to a tree branch node are then joined to the respective nodes in successive steps creating the MST. Mean branch length and its distribution is therefore one measure of nearest neighbor distance distribution of features. Various steps involved in obtaining a minimum spanning tree from the SEM images (BMP or JPEG) are described in the following sections.

In order to form VORONOI polygons nearest neighbors are identified for any given point. Perpendicular bisectors are drawn on the lines joining this point to its nearest neighbors. Polygons created by these perpendicular bisectors are called

VORONOI polygons. The number of sides of each VORONOI polygon corresponds to the number of nearest neighbors for that point. A perfectly hexagonal arrangement of pores for example will result in every pore having six nearest neighbors.

Minimum spanning tree and VORONOI polygons were generated by using an IDL program which was written by an earlier student at Cleveland State University [67]. The various steps involved in obtaining the MST using the (cmx, cmy) data are as follows:

(a) Initiate IDL program in the Sun Solaris Work Station

(b) Save (cmx,cmy) data obtained from sigmascan pro 5 as ASCII text file

(c) Loading the (cmx,cmy) data into the IDL platform to obtain MST and Voronoi polygons

(i) Open unix shell from the desktop using the following commands in the command prompt: */usr/people/lu>>cd training:* This command changes the directory to training folder as IDL program is in this folder

(ii) Open avor.PRO, ***minspant.pro*** and ***slidescr.pro*** from the command dialog box by looking for any programs with the .PRO extension: Open - *.pro and all programs with the .PRO extension in that folder will be displayed. Select ***avor.pro*** from the list to open it. Similarly minspant.pro and slidescr.pro can also be opened by looking for programs with .pro extension.

(iii) Once the IDL program is open compile the following programs already present in the training folder: avor.PRO, minspant.pro and slidescr.pro*;* Note that all these programs have to be open before they are compiled

(iv) Commands – *compile avor.pro; compile minspant.pro and avor.PRO*

(v) Once the programs are compiled, IDL_ANALYSIS program can be executed to calculate the voronoi polygons and the MST diagrams

(vi) IDL_Analysis.txt program and relevant code interpretation

Openr, lun, 'half.txt',/get_lun :**half_txt is the file name to be read**

array=flatarr(2,1119) **:1119 represent the number of data points**

readf,lun,array

xx=array[0,]*

yy=array[1,]*

blank=replicate(0,1024,1024) **:This image resolution is (x,y) size of analyzed image in Sigmascan pro 5**

blank[xx,yy]=255

window,0,xsize=1024,ysize=1024,retain=2

tv,blank

z=tvrd()

write_png, 'center_1.png',z

freq=fft(z,-1)

power=shift(alog(abs(freq)),512,512)

```
tvscl,power

z1=tvrd()

write_png, ‘fft_1.png’,z1

triangulate,xx,yy,tr,conn=con

/compile “avor.pro”

x_size=1024

y_size=760

avor, xx, yy, n_elements(xx), con,x_size,y_size

t=tvrd()

tv,t

write_png, ‘voronoi_1.png’,t
```

:The file name desired for the voronoi polygon image can be assigned here

```
/compile ‘Minspant.pro” and “Slidescr.pro”

x=xx

y=yy

Tree = MinspanTree(x,y)

M = Moment(sqrt((x[Tree[0,*]]-x[Tree[1,*]])^2+$


(y[Tree[0,*]]-y[Tree[1,*]])^2, SDEV=SDEV)

PRINT ,M[0],’ = Mean Branch Length’

PRINT, SDEV,’ = Standard Deviation of Branch length’

PRINT, M[2] ,’ = Skewness of Branch length’

PLOTMST,x, y, Tree, TITLE= ‘Minimum Spanning Tree’, $
```

XTITLE= ‘X position’, YTITLE= ‘Y Position’ ,XRANGE=[MIN(X) ,MAX(X)],$

YRANGE=[MIN(y) ,MAX(y)] ,PRINTER=0

tt=tvrd()

write_png, ‘mst_1.png’ ,tt **:The file name desired for the MST diagram image can be assigned here**

After writing the png files, the MST diagram and Voronoi polygons are recorded in the desired folder. After executing the above IDL_Analysis program either as a complete program or as individual parts to generate the MST diagrams and Voronoi polygons, the following information is relevant which can be recorded as output from the IDL as shown in Tables VI and VII.

MST

Parameter	Value
Mean Branch Length	
SDEV	
Skewness	

Table VI MST output information recorded from IDL

VORONOI Polygon

Number of sides of polygon	Number of features
3	
4	
5	
6	
7	

Table VII VORONOI polygon output information recorded from IDL

2.10.2 Nearest Neighbor Distance for Pores

The mean nearest neighbor distance for pore was calculated using the following program compiled in Microsoft Visual studio. The program calculates the mean and standard deviation for the nearest neighbor distances for each of the (x, y) points.

```
/* Program to calculate the mean neighbor spacing  */

#include <stdio.h>
#include <conio.h>
#include <stdlib.h>
#include <math.h>
#define DATASIZE 2939  /*( Number of features in a picture) */
#define MAGNIFICATION 1  /* For 50x (1000micro-m/358) */
#define NEAREST 1


void main()
{
      float xValue[DATASIZE], yValue[DATASIZE];
      int i = 0,j = 0,l,m, dataPoints =0, value;
   float distance =0,dist[DATASIZE],sum,temp;
   char c;
   FILE *fInput;
   FILE *fOutput;
   FILE *fNearest;
   /* File containing data points of the centre of mass from Sigma
scan*/
   fInput = fopen("X_Y.txt","r");
   /*  file containing distances between  points for an image*/
   fOutput = fopen("dist.txt","w");
   /* file which acts as the source file for distances in the
program to get the frequency distribution*/
   fNearest = fopen("dist.txt","r");

   if (fInput == NULL) /* Checking error in the input data file*/
      printf("\n The Input Data File does not exist");
   else
   {
            while (fscanf(fInput,"%f
%f",&xValue[i++],&yValue[j++])!=EOF)
      {
         dataPoints++;
         printf("%6.1f\t%6.1f\n",xValue[i-1],yValue[j-1]);
      }
    } fclose(fInput);
    if (NEAREST >= dataPoints)
      value = dataPoints-1;
    else
      value = NEAREST;
    for (i=0;i<=dataPoints-1;i++)
    {
```

```
      //fprintf(fOutput,"\n\nFor the #%d DataPoints
(%6.1f\t%6.1f)\n", i+1,xValue[i],yValue[i]);
      //      fprintf(fNearest,"\n\nFor the #%d DataPoints
(%d,%d)\n", i+1,xValue[i],yValue[i]);
      for(j=0,l=0; j<=dataPoints-1;j++)
      {
            distance = (MAGNIFICATION) * sqrt((((xValue[j]-
xValue[i])*(xValue[j]-xValue[i]))+ ((yValue[j]-
yValue[i])*(yValue[j]-yValue[i]))));
         if (distance != 0)
         dist[l++]= distance;
//                fprintf(fOutput,"%.2f\n",distance);

      }

      for ( l=0,sum =0; l< value; l++)
      {
            for (m=l+1; m< dataPoints-1; m++)
            {
                  if( dist[m]< dist[l])
            {
                  temp = dist[l];
                  dist[l] = dist[m];
                  dist[m] = temp;
            }
            else;
         }

       fprintf(fOutput,"%.2f\n",dist[l]);
       sum = sum + dist[l];
     }
     fprintf(fNearest,"%.2f\n",(sum/value));
     //fprintf(fOutput,"\n%.2f\n\n",(sum/value));
    }

    fclose(fOutput);
    fclose(fNearest);
}
```

The program when compiled using the cm(x, y) and data size as input, yields a table of nearest neighbor distances. The mean and standard deviation of data set was calculated using Sigmastat; this will be denoted as mean nearest neighbor spacing.

CHAPTER III

RESULTS AND DISCUSSION

3.1 Porous Alumino-Silicate Films on Metallic and Non-metallic Substrates

Sections 3.2 thru 3.6 discuss the results of:

(a) Growth of zeolites and mesoporous silica on various metallic and non-metallic substrates and characterization of the growth

(b) Electro-deposition of metal into the pores of alumino-silicates and characterization for presence of metal

3.2 Faujasite and Silicalite Growth on Sintered Copper

Figure 36 shows that silicalite tends to grow in a much more uniform fashion covering the entire copper substrate as compared to Faujasite. Faujasite particles ranging in size from 2 to 3 microns prefers to deposit on the top of the individual sintered copper particles, leaving some copper particles uncovered with faujasite.

The silicalite crystals are large, ~ 40 microns x 30 microns, more uniformly distributed, well inter-grown and creating a complete coverage of the sintered copper sample.

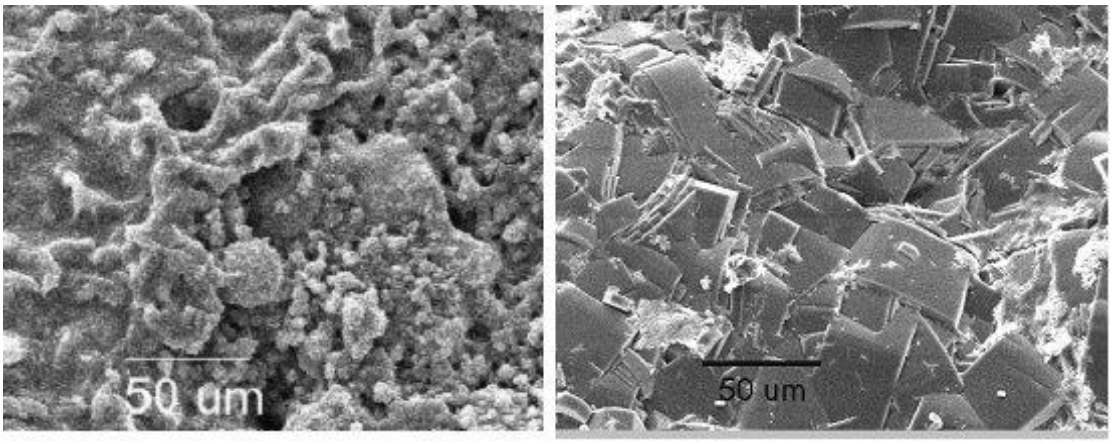

Figure 36 Faujasite and silicalite growth on sintered copper

3.3 Faujasite and Silicalite Growth on Anodized Aluminum/NaOH Treated Titanium

Silicalite grows well on anodized titanium as well as NaOH treated titanium compared to faujasite as seen in figures 37 and 38. Silicalite was found to grow uniformly on all the three substrates. Faujasite tends to grow in the form of uniformly distributed individual particles.

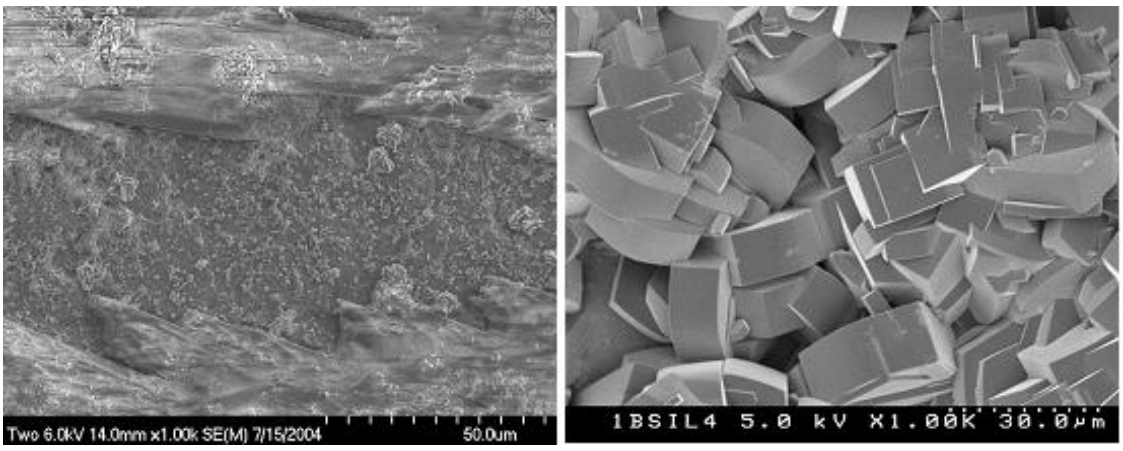

Figure 37 Faujasite and silicalite growth on anodized titanium

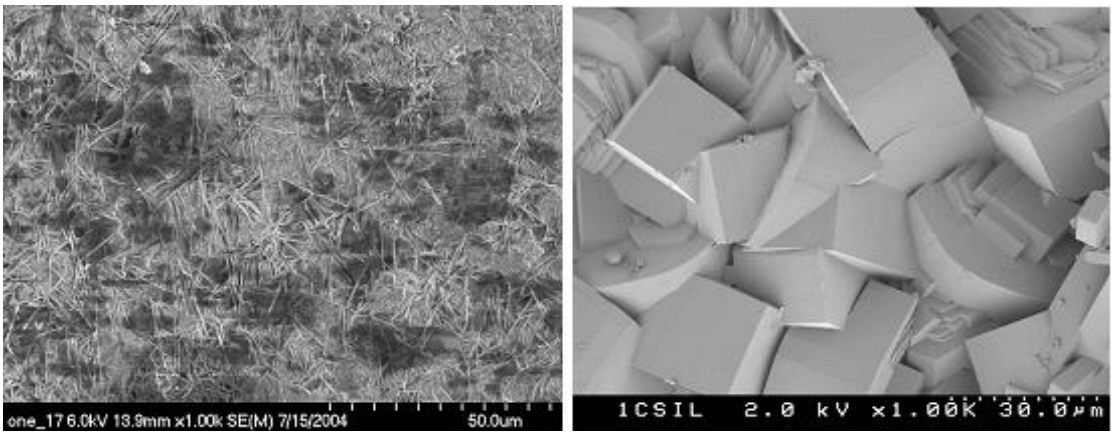

Figure 38 Faujasite and silicalite growth on NaOH treated titanium

3.4 Effect of reaction chemistry on the microstructure of zeolites

Reaction chemistry was investigated as an experimental variable for zeolite film growth on sintered copper. It was found that diluting the reaction chemistry four-fold resulted in more uniform particle distribution for faujasite. Faujasite particles still tended to grow from top of the copper particles, but appeared to provide more uniform coverage all over the substrate.

Silicalite reaction chemistry diluted four-fold resulted in the increased aspect ratio of silicalite crystals by two-fold and the crystal size decreased 5 fold in length and 10 fold in width. Intergrowth of crystals was more in the case of dilute reaction chemistry. SEM viewgraphs are shown in Figure 39.

Faujasite

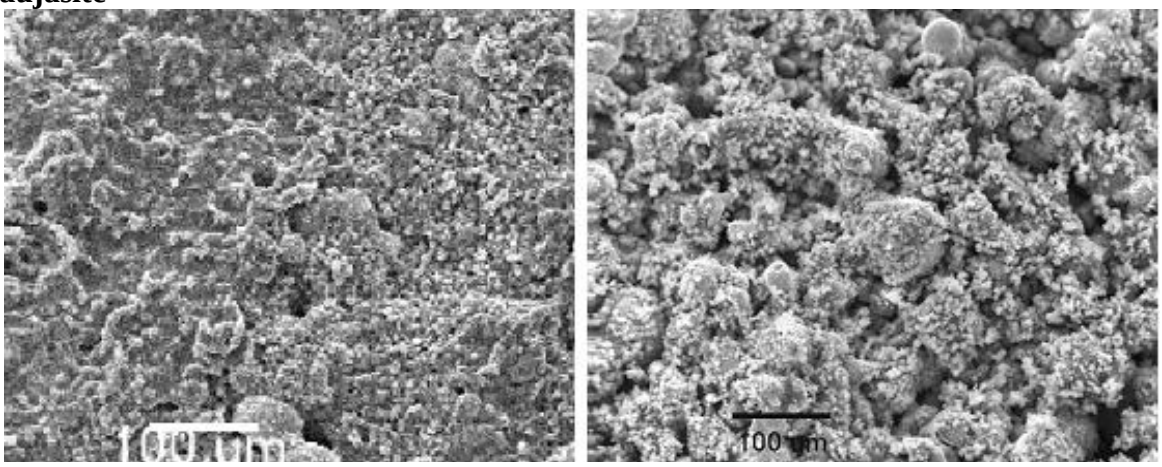

Regular reaction chemistry **Dilute reaction chemistry**

Silicalite

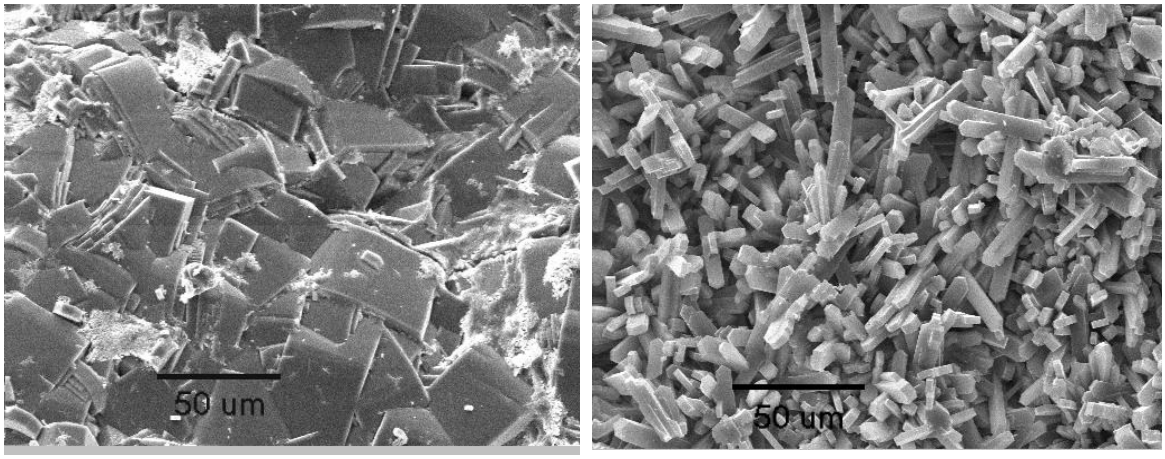

Regular reaction chemistry **Dilute reaction chemistry**

Figure 39 Effect of dilute reaction chemistry on crystalline structure of zeolite

3.5 Metal Phase Growth in Faujasite Deposited on Anodized Titanium

Copper was grown into the pores of faujasite synthesized *in-situ* on anodized titanium. Copper rich sites were evident both in EDAX and HRTEM analysis shown in figure 40. The "mushrooms" seen in the figure are copper overgrowth. Region A in thin faujasite film shows substantial amount of copper growth. This experiment led to the conclusion that metal phase growth into the pores of a zeolite synthesized *in-situ* is possible.

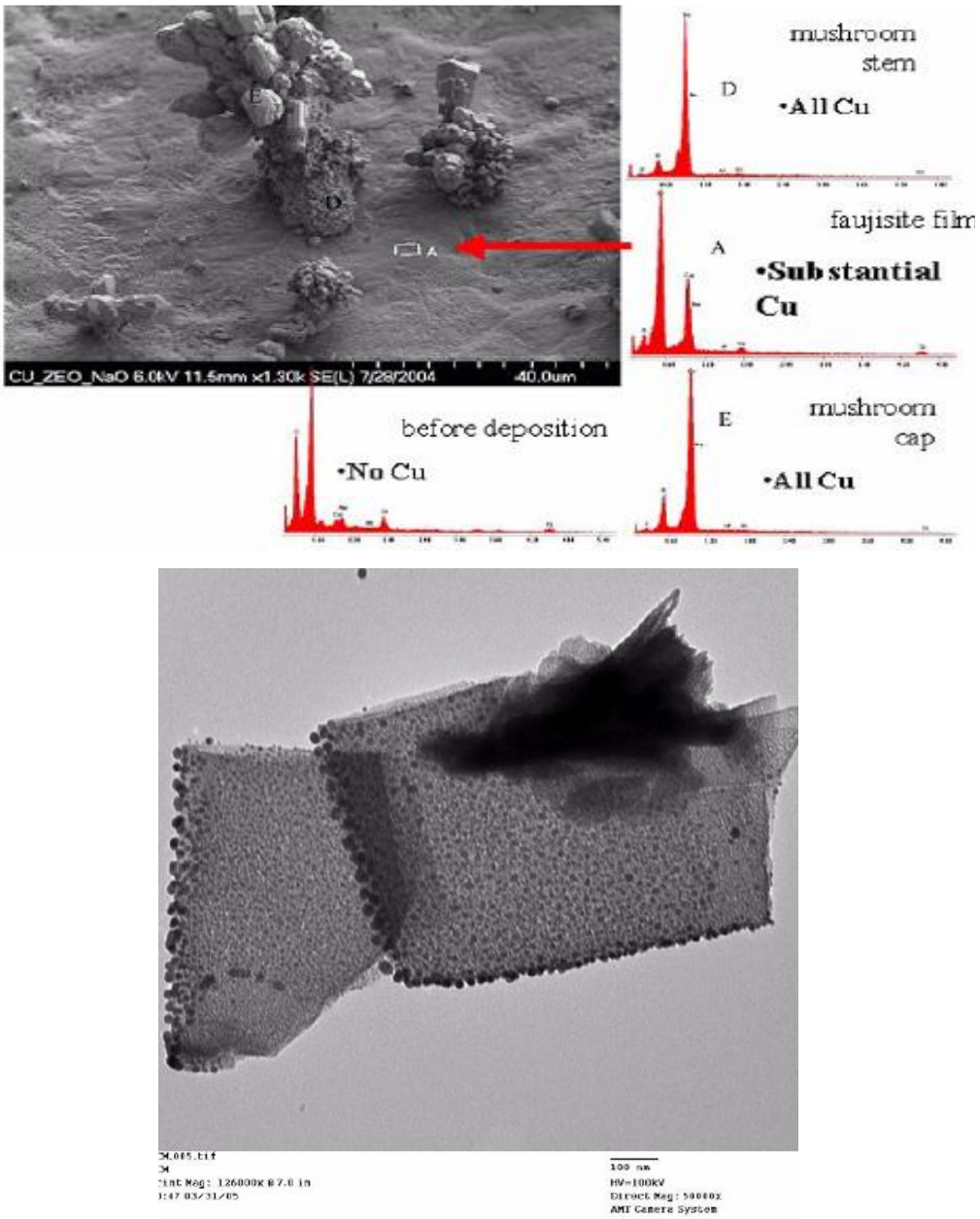

Figure 40 EDX and HRTEM of copper growth in faujasite

3.6 Mesoporous Silica Growth On Metallic and Non-Metallic Substrates

3.6.1 MPS Growth on Sintered Copper:

Mesoporous Silica was grown on sintered copper substrates. The substrate was then ultrasonically washed in DI water to remove any unattached particle debris. Mesoporous silica deposited in the form of a thick layer (figure 41) on the copper particle surfaces and also in the voids between the neighboring sintered copper particles.

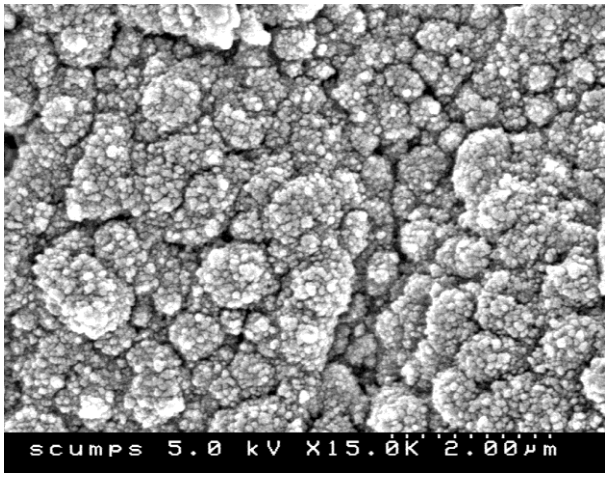

Figure 41 Mesoporous silica coated sintered copper

MPS coated sintered copper was then used to electro deposit nickel metal into the pores of the mesoporous silica layer. Very fine metallic growth on the surface was observed throughout (figure 42). The surface also showed larger metallic overgrowth regions.

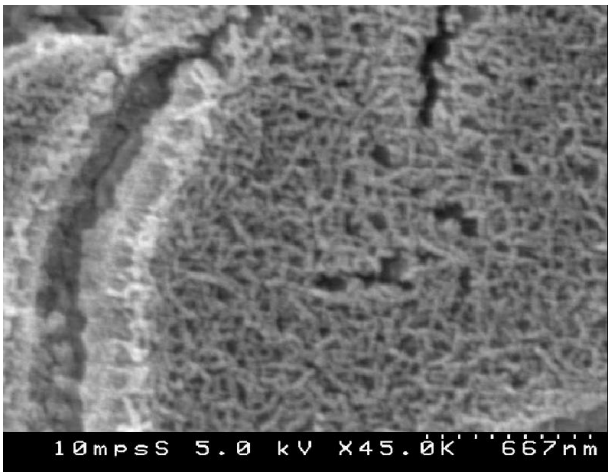

Figure 42 Fine metallic growth on the surface of MPS coated sintered copper

After metallic growth of nickel, mesoporous silica was dissolved in a low concentrated alkali solution. The SEM analysis showed that nickel features in the size range of 10 nm to 20 nm were found on the surface. The EDX analysis (figure 43) shows strong presence of nickel and very little amount of silicon. Copper is obtained due to the signal scattered from the sub-surface of sintered copper. The nickel presence is due to the nickel sulfate electrolyte used during electro-deposition.

The nickel grown MPS material after alkali dissolution was flaked off from the surface of the substrate and a high resolution TEM analysis was performed for metal growth evidence. The results show metal presence, however the features of nickel found were much smaller than what was seen in SEM.

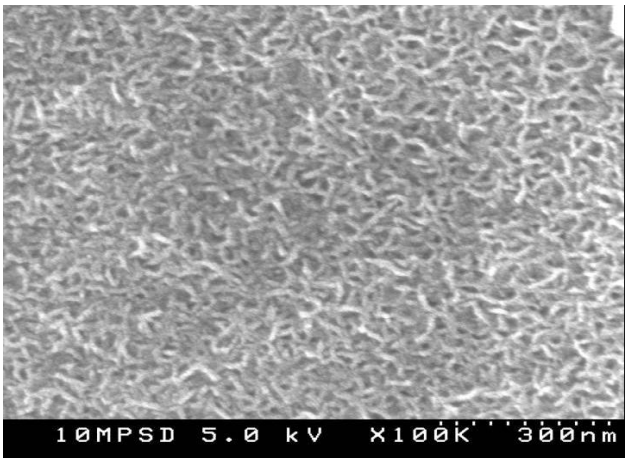

Element	Atom wt%
O	39.7
S	3.97
Ni	34.21
Cu	21.14
Si	0.98

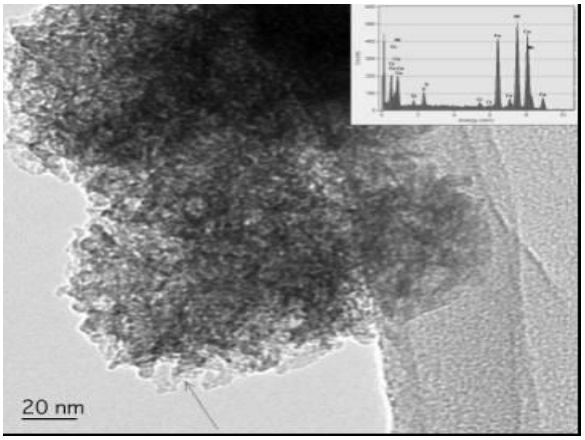

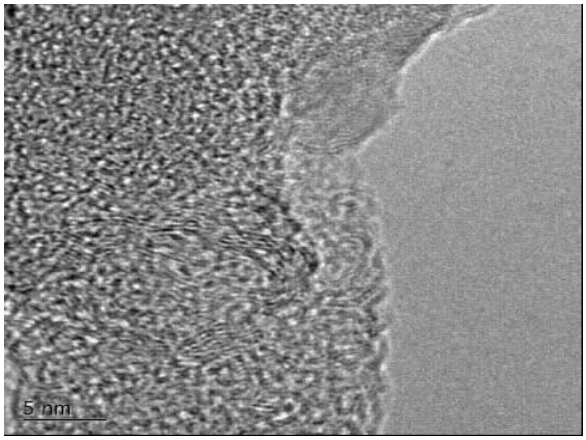

Figure 43 EDX analysis and HRTEM analysis of nickel growth in mesoporous Silica

3.6.2 MPS Growth on Anodized Titanium

Anodized titanium was used to grow MPS *in-situ* and then the substrate was washed ultrasonically. This was followed subsequently by nickel growth into the pores of MPS. Anodized titanium grows in the form of a very thin layer on the anodized titanium surface as compared to growth on sintered copper. Since most of the anodized surface remains exposed during metallic growth, Nickel grew preferentially on this surface. EDX analysis of the surface shows predominantly

nickel presence and very little silicon presence due to a very fine layer of MPS as seen in figure 44. Nickel growth was also seen in many areas on the surface of anodized titanium.

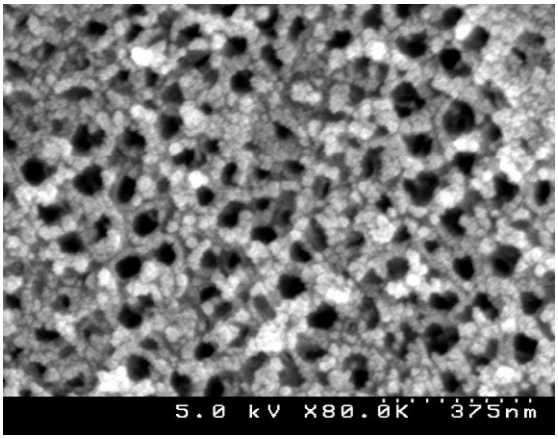

MPS coated anodized titanium

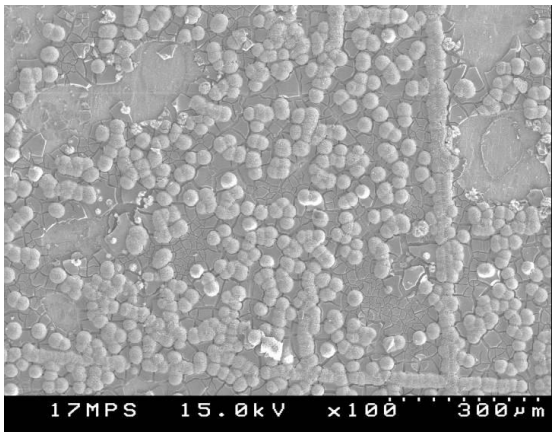

Metal growth into MPS

Element	Atom Wt%
Ni	38.80
Si	0.09
O	51.60
Ti	1.73
S	7.78

Figure 44 Mesoporous silica on anodized titanium and Nickel growth

3.6.3 MPS Growth on Anodized Aluminum

Mesoporous Silica was also grown on anodized aluminum with pores of 50 nm and pore walls about 20 nm thick in dimension. This system has provided the best coverage so far as MPS has deposited in the form a thick layer and the pores of anodized aluminum were not visible on the surface after MPS deposition. Some regions show worm-like overgrowth which is a characteristic of MPS growth as

shown in figure 45. However, metal could not be grown into the pores since anodized aluminum oxide is an electrical insulator.

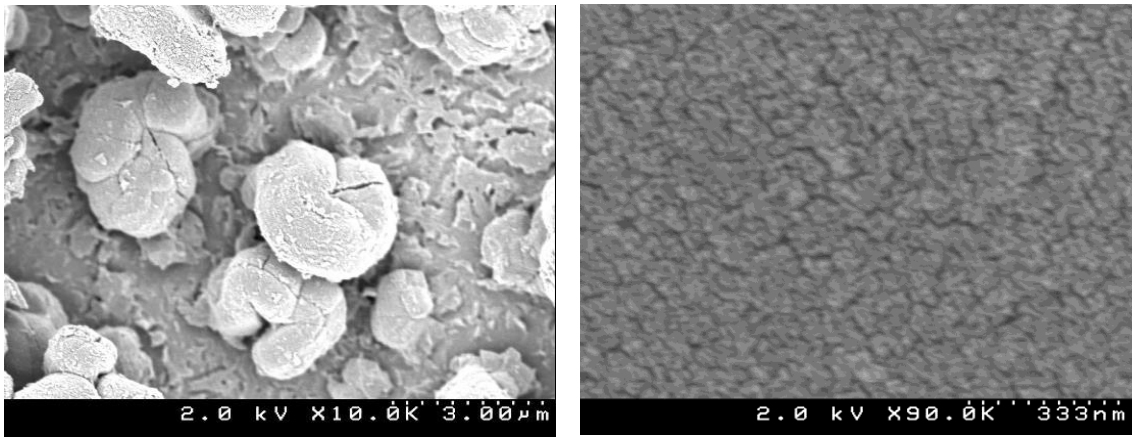

Figure 45 Mesoporous silica growth on anodized Aluminum

3.6.4 MPS Growth on Anodisc®

We have observed that coating the Anodisc twice results in a much better coating than coating only once (figure 46). MPS has covered more than half of the porous alumina membrane. Pores and pore walls are covered more and an average over various locations showed that more than 50 nm of the pore gets coated with MPS. SEM view graphs of the bare membrane and a MPS coated Anodisc are shown in figure 46.

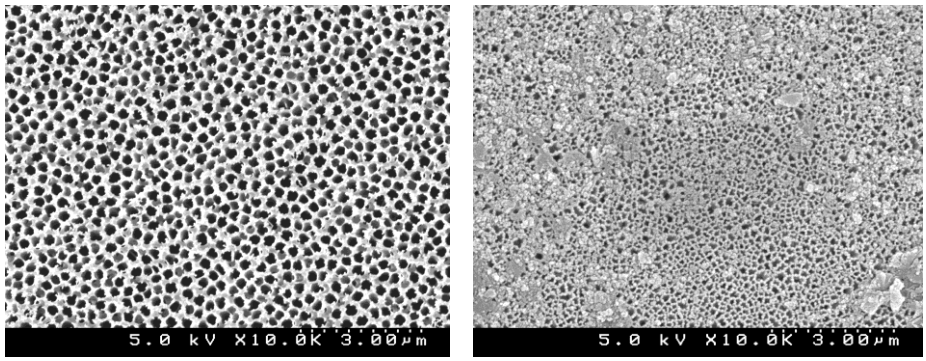

Bare Anodisc membrane **MPS coated Anodisc**

Figure 46 Mesoporous silica growth on Anodisc®

3.7 Nano-porous Anodic Alumina Membranes

Sections 3.8 thru 3.11 discuss the following:

(a) Fabrication of porous anodic alumina membranes at various voltages and characterization using statistical and image analysis techniques

(b) Anodization of single crystal aluminum and examining the dependence of pore morphology and distribution on the orientation of single crystal materials.

3.8 Microstructure of PCAA

PCAA or poly-crystalline anodic alumina was made in our lab from commercially obtained 99.999% pure Al and anodizing it in 0.3M oxalic acid followed by subsequent steps of metal dissolution and barrier oxide dissolution to obtain porous anodic alumina membrane materials with thru porosity.

Pore morphology of (PCAA) fabricated at various voltages of 30V, 40V, 60V and 80V was examined using scanning electron microscopy. These materials were fabricated with open pore structure on both sides using the standard anodization in a 0.3 M oxalic acid electrolyte at 7^{o}C, metal dissolution and barrier layer dissolution techniques described in Section 2. Alumina material has two surfaces of interest namely the pore side and the cap side. Pore side of the alumina material refers to the surface of the oxide exposed to the electrolyte where the oxide forms and dissolves due to the imposed electric field. Cap side refers to the bottom surface of the oxide layer where the barrier layer oxide is present at the metal/oxide interface. Metal is continually oxidized at this interface to form aluminum oxide. Figure 47 (a), (b), (c) and (d) show typical morphology of the pores on the anodization (pore side) and the

barrier layer oxide (cap side) sides of the samples anodized at 30V, 40V, 60V and 80V.

(a) Pore Morphology – Pore side of PCAA

The pore side of the aluminum oxide at various voltages consists of uniformly distributed pores arranged in a lattice with certain ordering. Pores formed due to anodization at voltage of 40 V appear to be most uniformly distributed compared to the pores formed due to anodization at 30V, 40, 60V or 80V. Pore spacing and pore wall thickness are also uniform. The pores on the pore side of PCAA formed at 40V are organized in domains of a few microns in size. Since the pores on the pore side of PCAA are formed by self-organization during anodization of aluminum the pore morphology parameters on this side are only the function of the anodization voltage (electrolyte, concentration of the electrolyte and temperature of anodization are all fixed).

(b) Pore Morphology – Cap side of PCAA

The pores on the cap side of the PCAA were formed by opening the caps or the bottom barrier layer oxide of the pore channels by chemical etching in a 5 wt% H_3PO_4. The purpose of opening the pore channel caps on the barrier layer oxide of PCAA is to create through thickness open pore channels. The time required to open these pore caps was determined by progressively increasing the time of exposure to acid and SEM observation. The time required to open the barrier layer oxide for 30V, 40V, 60V and 80V anodization was found to be about 70, 90, 210, and 275 minutes respectively. The apparent pore diameter and wall thickness directly depend on the time of etching; higher etching times create a larger pore with thinner oxide wall. The

apparent pore morphology parameters on this side are therefore directly dependent on the time of etching. However, for a given etching condition the pores on the cap side also appear to be uniformly distributed and have uniform pore diameter and wall thickness across the entire disk surface.

(a) 30V – pore and cap

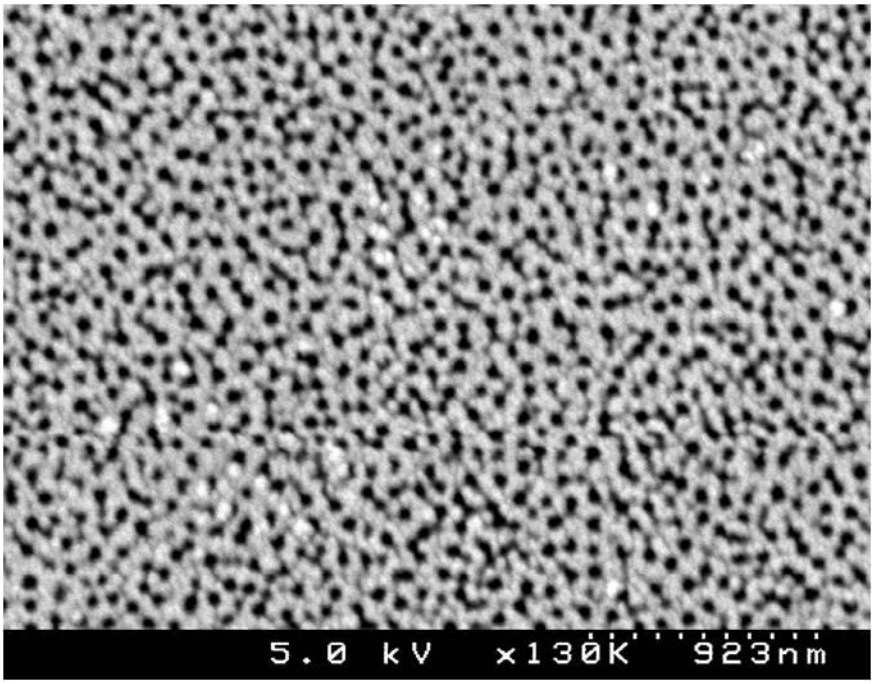

Pore side

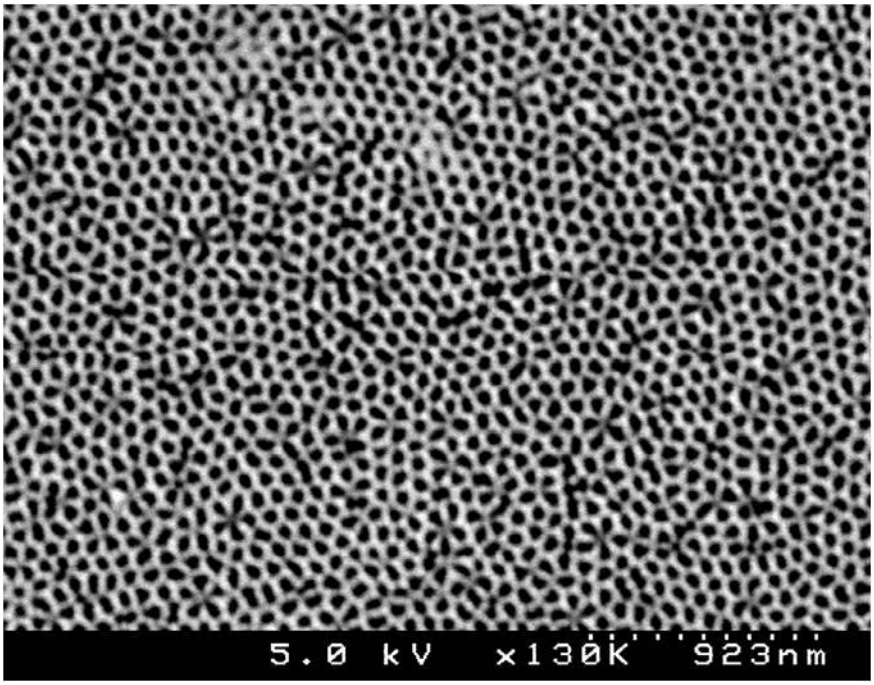

Cap side

(b) 40V – pore and cap

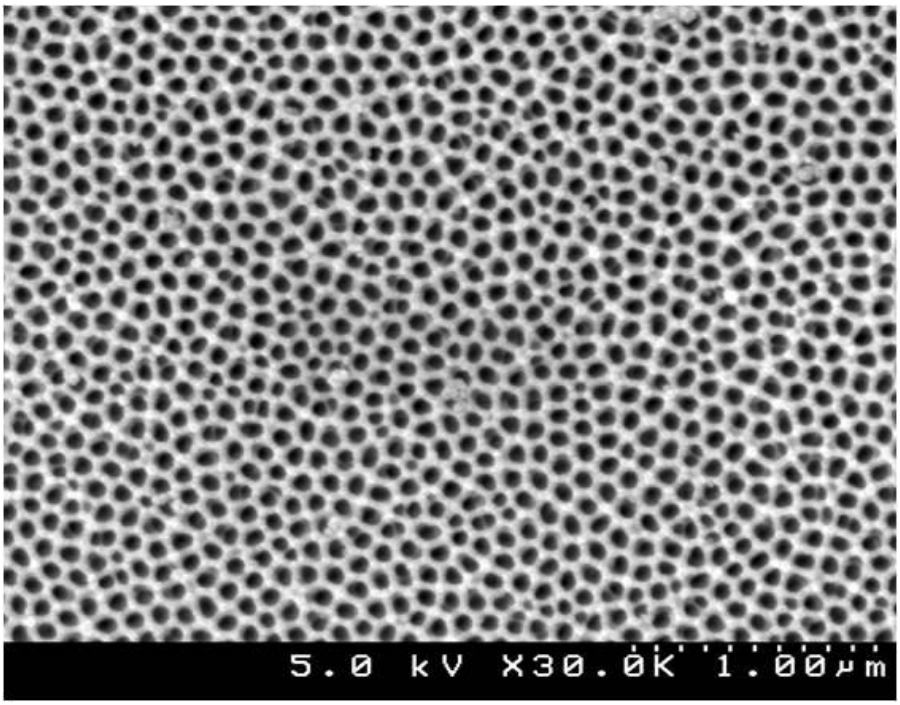

Pore side

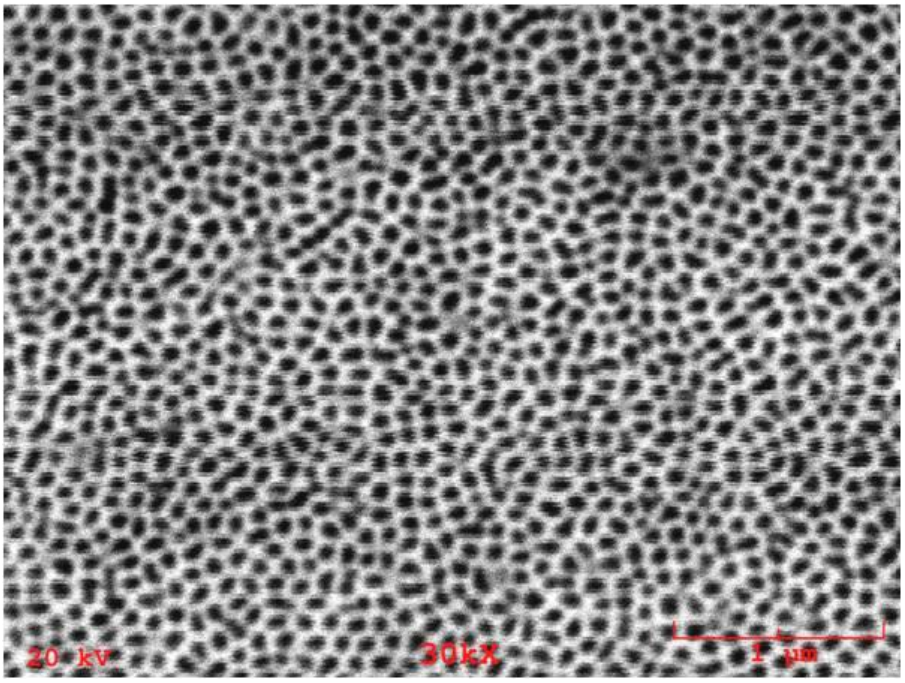

Cap side

(c) 60V – pore and cap

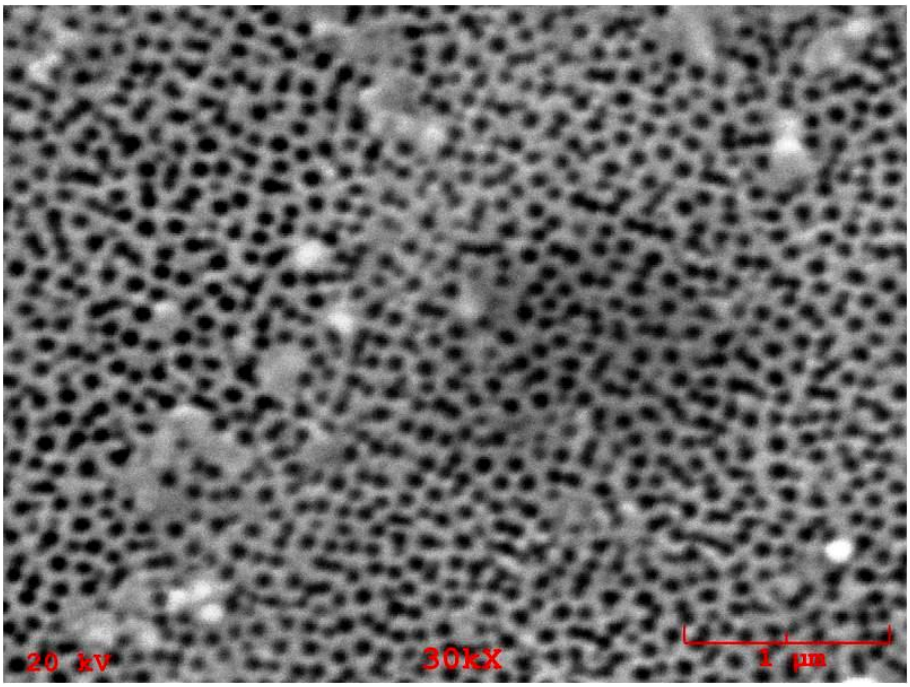

Pore side

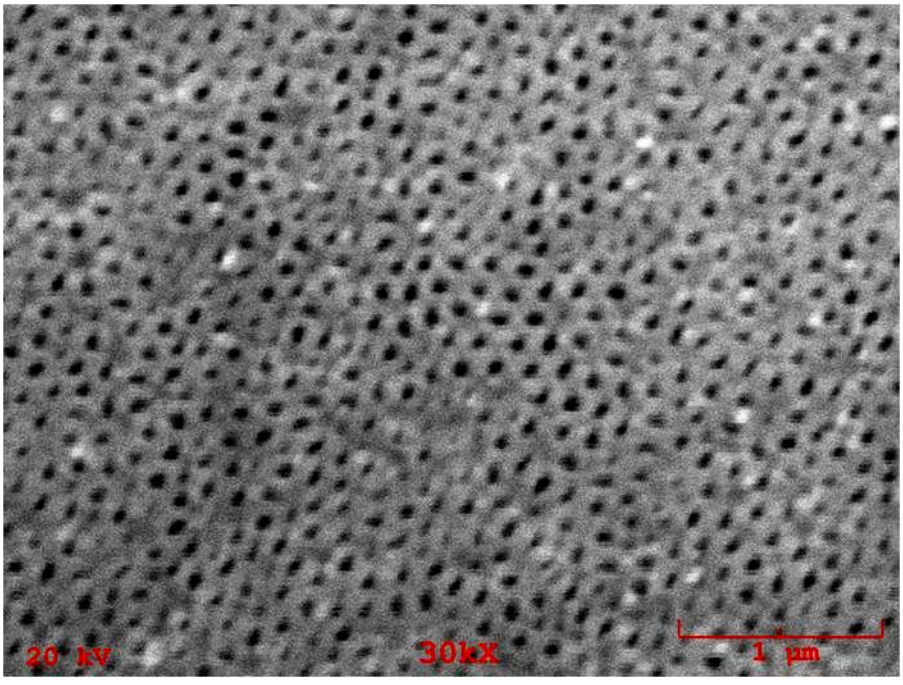

Cap side

(d) 80V – pore and cap

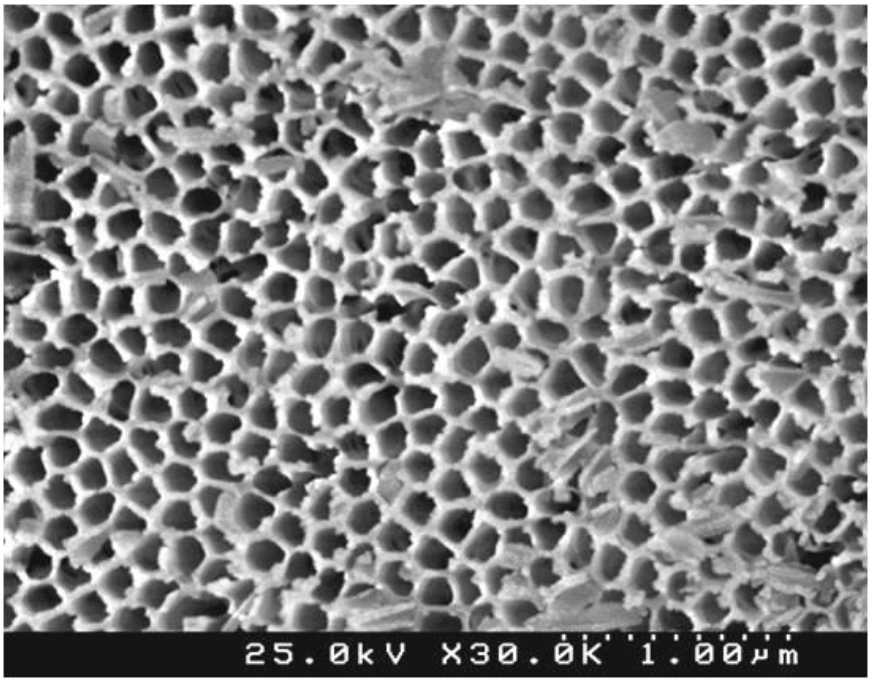

Pore side

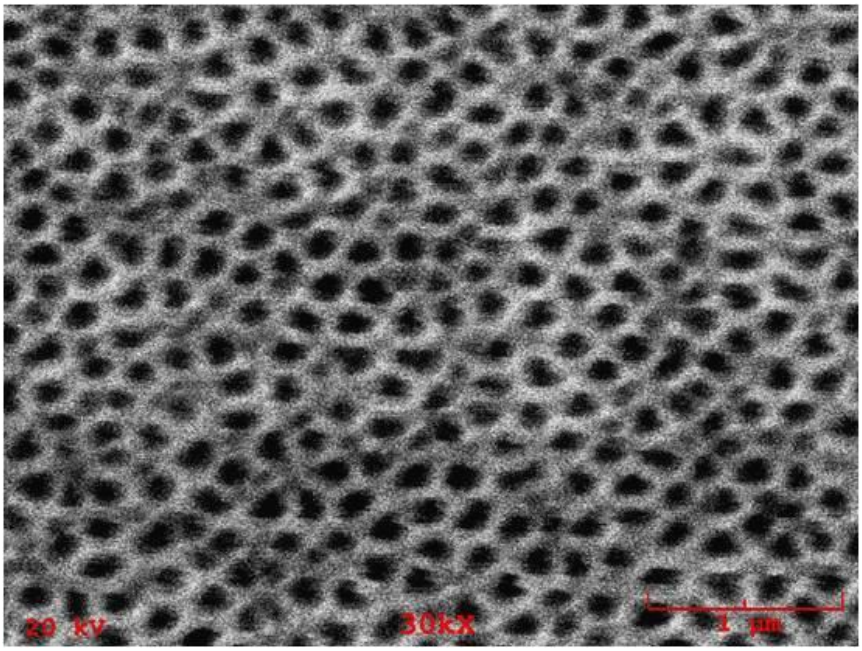

Cap side

Figure 47 Free standing PCAA at (a) 30V (b) 40V (c) 60 V and (d) 80 V

3.8.1 Effect of Anodization Voltage on Pore Morphology in Poly-Crystalline Anodic Alumina

We have performed statistical analysis of the pores at various voltages to quantitatively determine the effect of anodization voltage on pore parameters such as pore diameter, inter-pore spacing and uniformity of pore distribution. This observation is in agreement with results reported in the literature by Sulka et al. [62] indicating that pore diameter increases linearly with increase in anodization voltage. It was found that the pore size, and inter-pore spacing of the anodic alumina increases with increase in anodization voltage. Pore ordering was found to be most uniform at anodization voltage of 40V.

Wall thickness was calculated as the difference between the mean nearest neighbor pore spacing and the pore diameter since this is geometrically true for the hexagonal pore arrangement in PCAA materials.

$$D_{spacing} = D_{pore} + WT \tag{5}$$

Schematics of cell morphology and structural geometry of two neighboring cells are shown in figure 48. $D_{spacing}$ refers to the mean nearest neighbor spacing, D_{pore} refers to the pore diamater and WT refers to the wall-thickness.

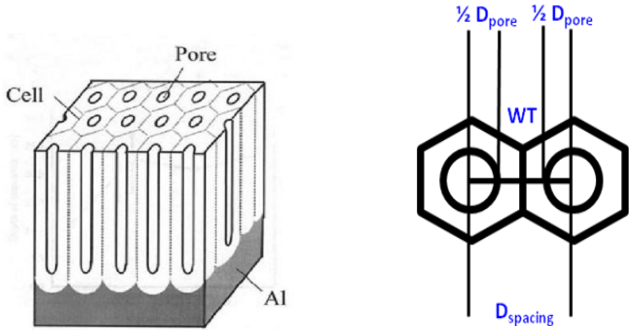

Figure 48 Structural morphology of anodic alumina

3.8.2 Typical Statistical Analysis of Pore Morphology and Distribution in PCAA

It is important that the pore parameters primarily pore diameter, pore spacing and wall thickness be statistically determined in order to characterize nanoporous alumina films. Typical microstructural analysis to determine the minimum spanning tree and voronoi polygon parameters is shown in figure 49. Figure 49 (a) shows the pore microstructure for a PCAA formed at 30 V. Figure 49(b) shows the corresponding center of mass locations for the pores. These centers of mass were used to determine the Mimimum Spanning Tree shown in figure 49(c), which is used to determine the distribution of nearest neighbor distances. Figure 49(d) shows a predominance of six-sided polygons in the corresponding voronoi distributions suggesting a hexagonal ordering of pores.

Appendix A lists the various MST and VORONOI polygon images generated for the microstructural analyses of the PCAA formed at various voltages. It is very important that the quality of SEM micrographs and the arrangement of pores have a distinct contrast without any visual artifacts in order for them to be analyzed using sigmascan pro. In case of any visual artifacts or large disconnected pores, the image analysis tends to pick up large cm (x, y) values which would result in erroneous calculation of pore parameters. SEM images for the PCAA formed at 80V showed large number of joined adjescent pores and hence were not used for microstructural analysis.

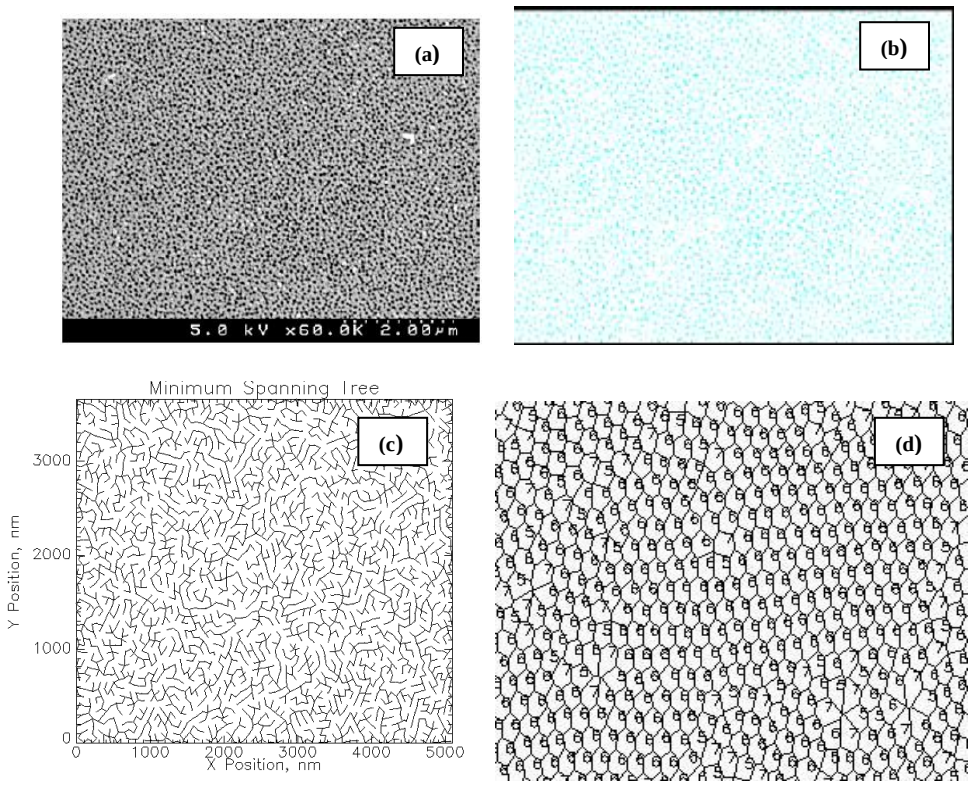

Figure 49 (a) SEM image and corresponding (b) cm(x,y) from sigmascan pro 5

(c) MST and (d) VORONOI polygon for PCAA formed at 30V

3.8.3 Effect of Anodization Voltage on Pore Characteristics – Pore Side of PCAA

Effect of anodization voltage on the pore parameters on the pore side of PCAA prepared with oxalic acid as the electrolyte is shown in table VIII. Table VIII lists the pore diameter, interpore spacing and pore wall thickness for the anodized alumina formed at 30 V, 40 V and 60 V on the pore side.

Voltage	Pore diameter (nm)	Mean Nearest Neighbor Spacing (nm)	Wall Thickness (nm)
30V	44.5±10.5	72.6±12.1	28.1±22.6
40V	51.4±12.1	91.7±11.4	40.3±23.5
60V	56.3±29.0	101.0±30.2	46.0±59.2

Table VIII Pore parameters of PCAA materials on the pore side of alumina

As shown in figure 50 the pore diameter, pore spacing and wall thickness (on the pore side of anodic alumina) all linearly increase with increase in anodization voltage. The linear dependence of pore parameters on anodization voltage is mainly due to the enhanced electric field at higher anodization voltages. The enhanced electric field results in dissolution of large areas of formed barrier layer oxide which results in large pore diameters and pore spacings on the surface of the aluminum oxide. The simultaneous formation of bulk aluminum oxide and hence the dissolution due to the application of an electric field are enhanced at higher voltages which results in formation of pore parameters of higher dimension.

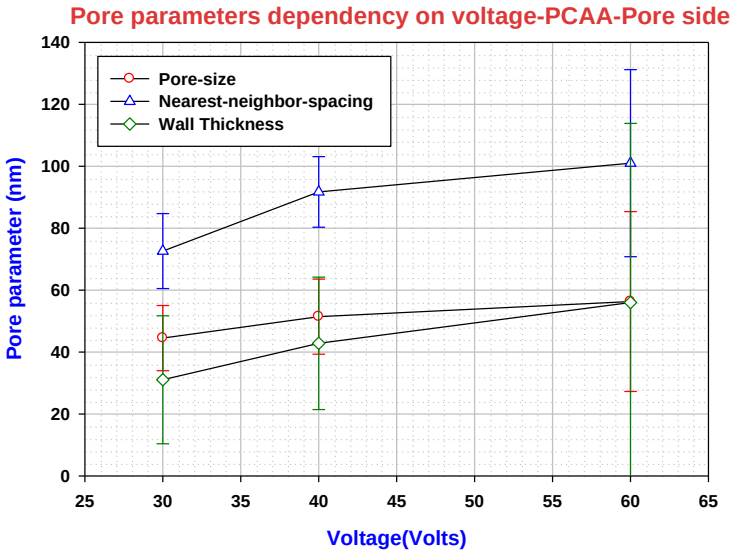

Figure 50 Effect of forming voltage on pore parameters

3.8.4 Effect of Anodization Voltage on Pore Characteristics – Cap Side of PCAA

Table IX shows the effect of anodization voltage on the pore morphology parameters of PCAA on the cap side of the material. Unlike the pore side behavior presented in 3.6.3 the pore diameter, pore spacing, wall thickness and mean nearest neighbor spacing on the cap side do not appear to correlate with anodization voltage. This may be because of the artificiality introduced by varying etching time and its reproducibility.

Voltage	Pore diameter (nm)	Mean Nearest Neighbor Spacing (nm)	Wall Thickness (nm)
30V	34.55±12.5	80.1±19.9	52.60±30.9
40V	37.56±13.3	73.2±28.6	51±36.2
60V	32.01±11.0	75.52±14.8	41.44±24.4

Table IX Pore morphology parameters on the cap side of PCAA

3.8.5 Influence of Anodization Voltage on the Number of Nearest Neighbors

Voltage dependence of the frequency distribution of the number of nearest neighbors obtained from voronoi polygons is shown in figure 51. The data correspond to the pore-side of the anodized disks. The corresponding regression fit to the modified three parameter gaussian distribution is shown by the dotted lines.

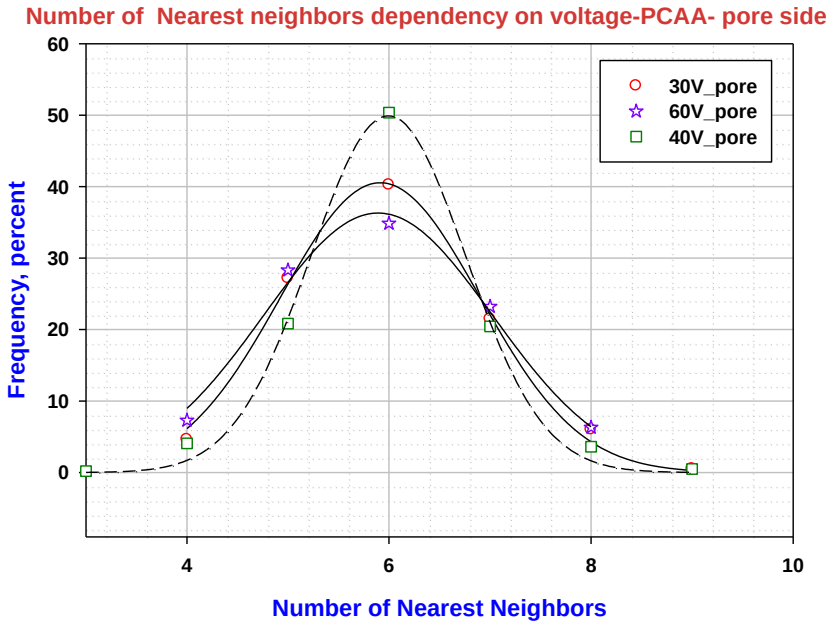

Figure 51 Number of nearest neighbor distribution for PCAA

This figure shows a predominance of six nearest neighbors. The hexagonal ordering is most prominent for the anodization voltage of 40V. It was qualitatively pointed out by Gosele et al. [46] that the 'self-ordering' regime for anodizing aluminum using 0.3 M oxalic acid as electrolyte is at 40V. Figure 51 confirms the same observation statistically.

3.8.6 Influence of Anodization Voltage on Pore Ordering

The mean branch length m* obtained from MST analysis and the corresponding standard deviation σ* were used to obtain the "m" and "σ" parameters as indicated below. Here, 'A' refers to the total cross-sectional area of the sample and 'N' refers to the number of pores.

So $m = m^* \cdot \sqrt{\frac{N-1}{A}}$ and $\sigma = \sigma^* \cdot \sqrt{\frac{N-1}{A}}$ (6)

	m* (nm)	σ* (nm)	N	A (nm^2)	m	σ
30V	75.55	10.15	2939	1.9E+07	0.94	0.12
40V	94.23	9.26	4201	4.2E+07	0.94	0.092
60V	111.3	28.81	1031	1.9E+07	0.82	0.31

Table X m and σ values for PCAA fabricated at 30V, 40V and 60V

Table X lists the experimentally observed m and σ values for the PCAA's fabricated at 30V, 40V and 60V. Figure 52 shows an 'm' vs. 'σ' plot. The solid line in this figure shows the corresponding m-σ behavior expected for a hexagonal lattice with varying degrees superimposed disorder [63]. The corresponding disorders are indicated at 10% increment along the solid line. This figure indicates that pore ordering in PCAA fabricated at various voltages is similar to a hexagonal tessellation with some superimposed random noise. The sample anodized at 40V has the least amount of disorder, about 35% with respect to a perfect hexagonal lattice. The sample anodized at 60V has the highest superimposed noise, more than 80%.

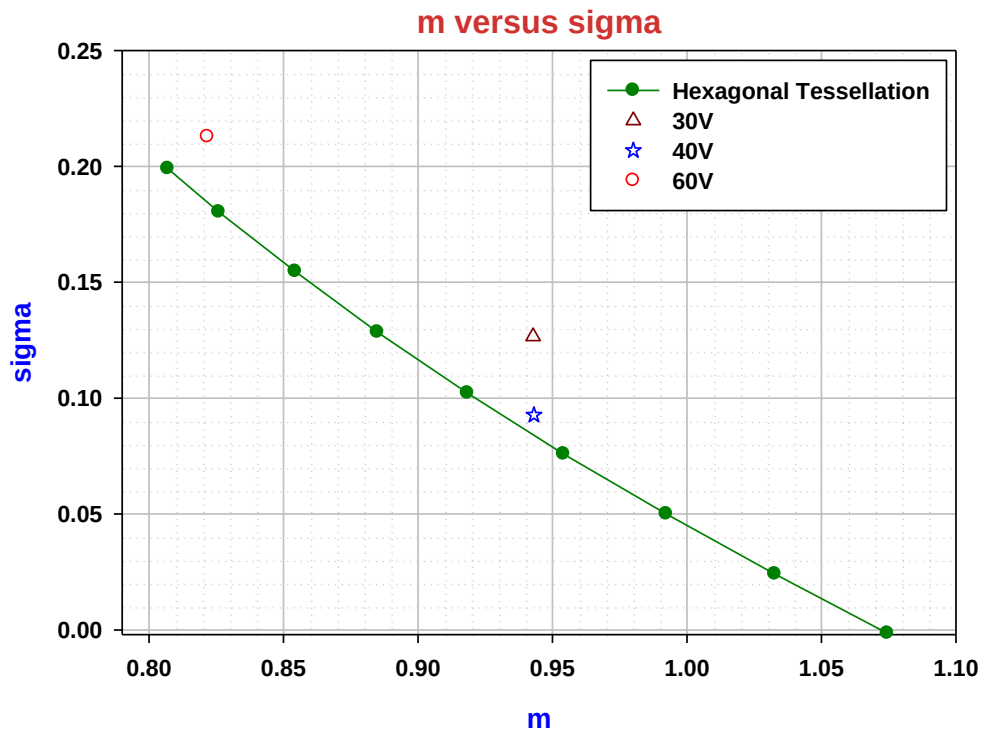

Figure 52 *m* versus σ for alumina materials formed at different voltages

3.9 Statistical Analysis of the Experimental Reproducibility (40 V Anodization)

A series of six PCAA samples were anodized in oxalic acid at a forming voltage of 40 V to examine the experimental reproducibility of the pore morphology and distribution. Based on outstanding experimental reproducibility as discussed below these disks were then used as template materials for the fabrication of metallic nano-wires.

3.9.1 Estimation of Pore Diameter, Inter-Pore Spacing and Nearest Neighbor Distributions

Figure 53 shows the frequency of pore diameter distributions for PCAA samples. The highest percentages of pores have been found to be in the pore diameter range of 50 – 60 nm. The pore distributions for the PCAA samples were identical with comparable pore diameters. Figure 54 shows the number of nearest neighbor distribution indicating that the pores in PCAA formed at 40 V in 0.3 M oxalic acid have predominantly hexagonal ordering. Both these figures confirm our experimental ability to reproduce reliably the PCAA samples with uniform pore parameters and hexagonal ordering so that they can be used with confidence as template materials for fabrication of nano-wires. Appendix B contains the corresponding SEM, MST, and Voronoi polygon images and the frequency distribution plots of the pore diameters for samples PCAA01, PCAA02, PCAA 03 and PCAA 06.

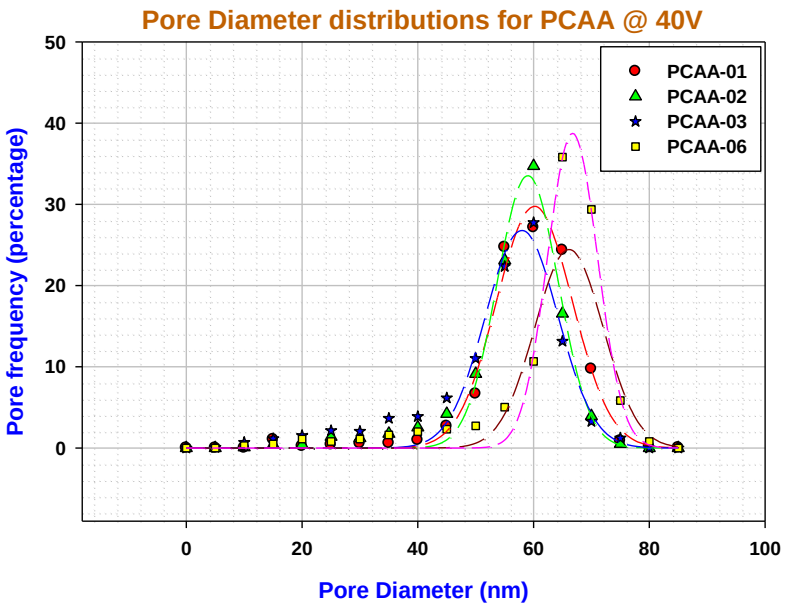

Figure 53 Pore diameter distribution for PCAA (40V anodization)

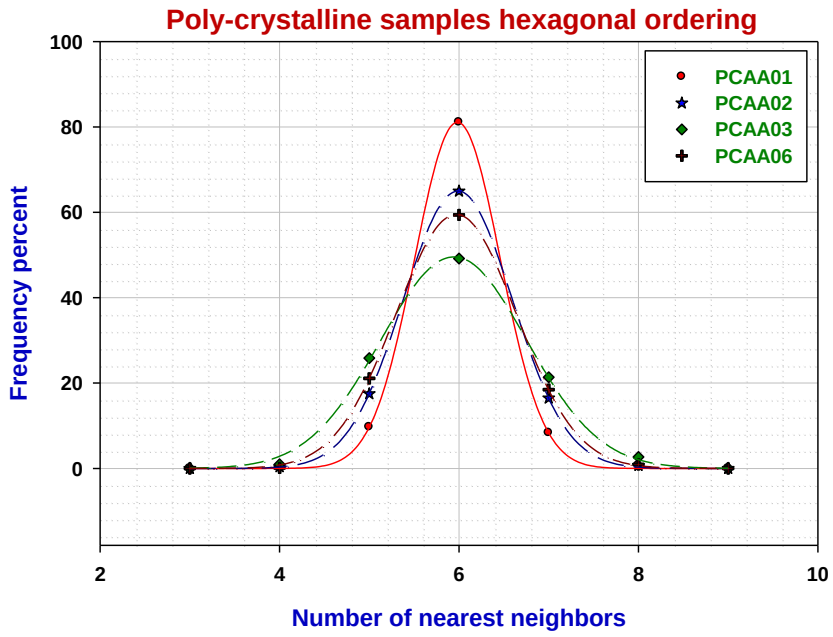

Figure 54 Number of nearest neighbor distribution for PCAA (40V anodization)

Table XI shows the mean pore size, mean pore spacing and nearest neighbor spacing for PCAA samples. Mean of the nearest neighbor spacing is very close to the spacing obtained from the mean branch length of the MST diagram identified as mean pore spacing in Table 11. Pore parameter values for the four different samples are comparable suggesting an excellent experimental reproducibility for 40V anodization.

Sample ID	Mean pore size (nm)	Mean Nearest neighbor spacing(nm)
PCAA-01	60.17±2.56	94.7±8.7
PCAA-02	59.02±2.13	90.3±9.5
PCAA-03	57.98±2.50	70.4±9.5
PCAA-06	66.75±2.08	91.4±10.9

Table XI Pore parameters of PCAA formed in oxalic acid at 40V

The weighted average of the data shown in Table XI was calculated as:

$$X_{WM} = \frac{\sum n_i . x_i}{\sum n_i} \qquad (7)$$

where X_{WM} refers to the weighted mean for a set of samples with a mean of x_i and the sample size being n_i. The weighted mean of the pore size thus calculated was 60.2 nm and the nearest neighbor spacing was 89.6 nm. These values are in good agreement with the values reported in literature by Lee et al. [64].

3.9.2 Pore Ordering for PCAA at 40V

Table XII shows the m and σ values. Figure 55 plots m versus σ values for samples PCAA-01, PCAA-02, PCAA-03 and PCAA-06, all anodized at 40V. They all fall quite close to the expected hexagonal tessellation with about 30 to 40% superimposed noise. This is in agreement with the mean nearest number of neighbors being six as indicated by the VORONOI polygons (Figure 54).

	m*(nm)	σ*	N	A (nm^2)	m	σ
PCAA-01	97.3	7.38	4201	4.2E+07	0.97	0.073
PCAA-02	92.94	8.36	2938	2.8E+07	0.95	0.085
PCAA-03	73.8	9.09	1321	8925504	0.89	0.110
PCAA-06	94.26	9.46	992	9733630	0.95	0.095

Table XII m – σ correlation for PCAA materials fabricated in the self-ordering regime

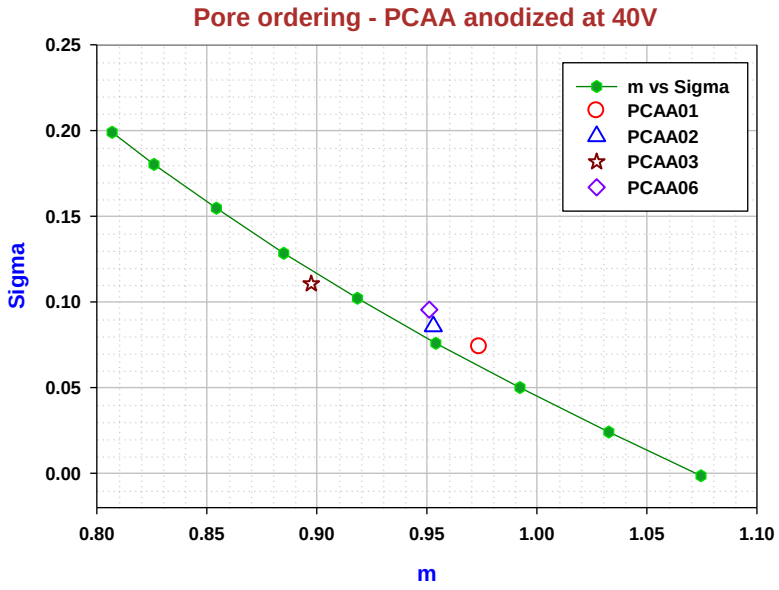

Figure 55 m versus σ for PCAA samples anodized at 40V (self-ordering regime)

3.10 Typical Microstructure of Metallic Nano-wires Formed Using Alumina Templates

Pore opened PCAA were used as molds to fabricate pure metallic nano-wires via electroplating. PCAA was procured commercially with trade name Anodisc® and was also fabricated in-house for this purpose. Metallic nano-wires were deposited using slow potentiostatic electro deposition of pure metal such as Copper and Nickel. These nano-wires were synthesized by another member of our group, Asli Ertan.

Anodisc® membranes have through pores, but the pores are not isolated along their entire length across the membranes. They apparently develop side branches and join frequently with neighboring pores as shown in Figure 56(a). In addition these membranes have about 150-200 nm diameter pores on the pore side and only 80-100 nm diameter pores on the cap side, as indicated in Figure 57. They are therefore not suitable as mold material to fabricate metal nano-wires with large surface area to volume ratio. This was the major driving force for us to develop anodization techniques suitable for yielding un-branched continuous small diameter nano-pore channels spanning across the entire membrane thickness (as shown in Figure 56(b)).

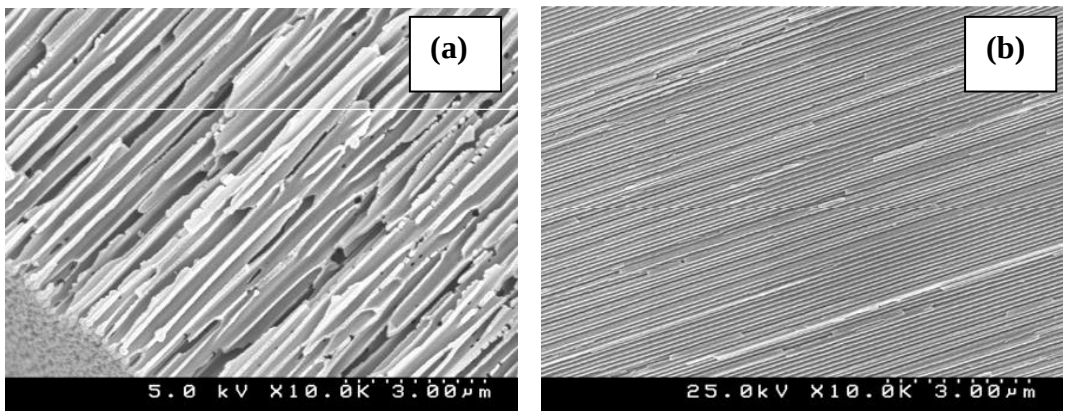

Figure 56 Cylindrical channels in (a) commercial versus (b) lab-synthesized alumina

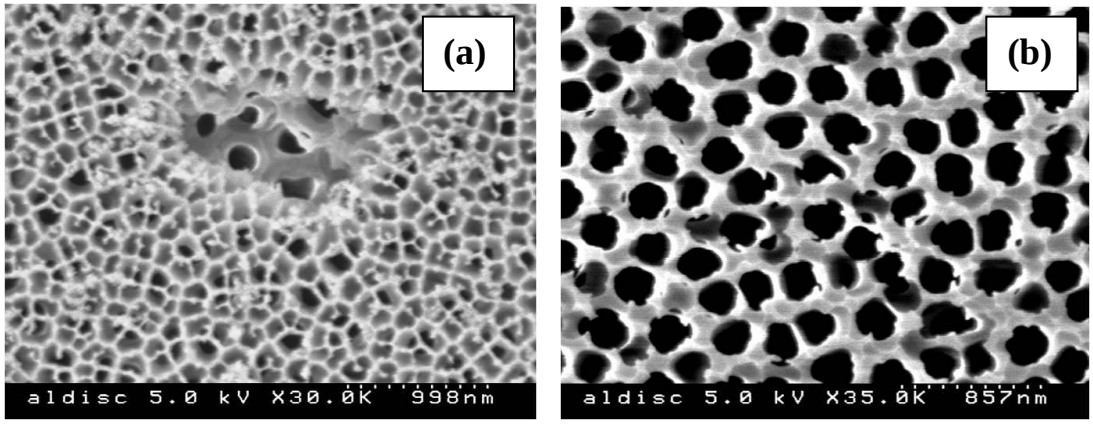

Figure 57 (a) Side a of Anodisc – 80 – 100 nm (b) Side b of Anodisc – 150 – 200 nm

3.10.1 Electro Deposition of Nickel Metal into Pore Channels of Alumina Templates to Fabricate Nano-wires

The electro-deposition process involved using pure nickel as anode and 40 V anodized alumina membrane backed with a conducting metal sheet, typically copper, as the cathode. The back of the alumina membrane was sputtered with gold in order to provide electrical conductivity between the copper sheet and the aluminum. Nickel was electrodeposited for 30 minutes using galvanostatic electro-deposition at room

temperature with an applied current density of 10mA/cm^2. The electrolyte used was 0.3 M nickel sulphate. The template material containing deposited nickel in its pore channels was rinsed and washed in NaOH to dissolve the aluminum oxide and obtain the Nickel fibers shown in Figure 58. These nano-fibers have an aspect ratio which reflects the aspect ratio of pore channels in the PCAA. Large volumes of these fibers with high surface-area to volume ratio were fabricated by Asli Ertan and used for studying hydrogen adsorption and desorption kinetics for her DRE Thesis.

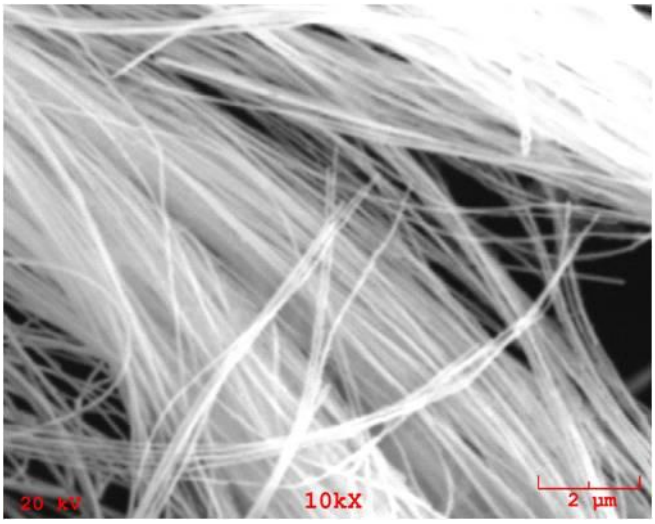

Figure 58 Nickel nano-fibers formed by slow galvanostatic electro-deposition

3.11 Fabrication of Single Crystal Anodic Alumina (SCAA)

Single crystal aluminum bars with crystallographic orientations in the [111], [110] and [100] directions were grown in our laboratory. About 125 μm thick disks were sliced from these bars. These were mechanically polished, electro-polished and anodized in 0.3M oxalic acid at 7^{o}C for 24 hrs in the manner described earlier. These single crystal anodic alumina materials will be referred to as SCAA in sections below. Pore morphology and their ordering have been examined in these SCAA samples only on the pore-side of the membrane. Konavolov et al [68] have examined the effect of crystal orientation on the electro-polishing patterns of aluminum single crystals. They concluded that the variation in patterns may be explained by a different adsorptivity of alcohol molecules on different crystalline faces. Purpose of this study was to examine the pore distribution and morphology of alumina membranes fabricated by using single crystal aluminum disks with their surface normal oriented along [100], [110] and [111] directions.

3.11.1 Pore Morphology of SCAA

3.11.1.1 Pore Morphology of SCAA [111]

Figure 59 (a) and (b) shows the typical pore morphology observed on the pore side of the anodized SCAA oriented in [111] direction. The lower magnification view shows a uniform distribution of pores. But a closer examination reveals that pores are not growing in a direction normal to the disk surface, i.e., along [111] direction. Instead they appear to grow along two or three directions that are oblique with respect to the [111] direction. This is more clearly evident in Figure 59(b) which contains

tetrahedral looking over etched cavities. The walls of these cavities have gotten anodized creating pores that have similar oblique orientations as those located on most of the disk-surface. Figure 59 (c) shows closer snapshots of several typical pore channels on the sample surface, i.e., on (111) plane. It is interesting to note that often very next to each other the pores appear to form and grow along these oblique orientations. There appears to be a predominance of three such oblique directions.

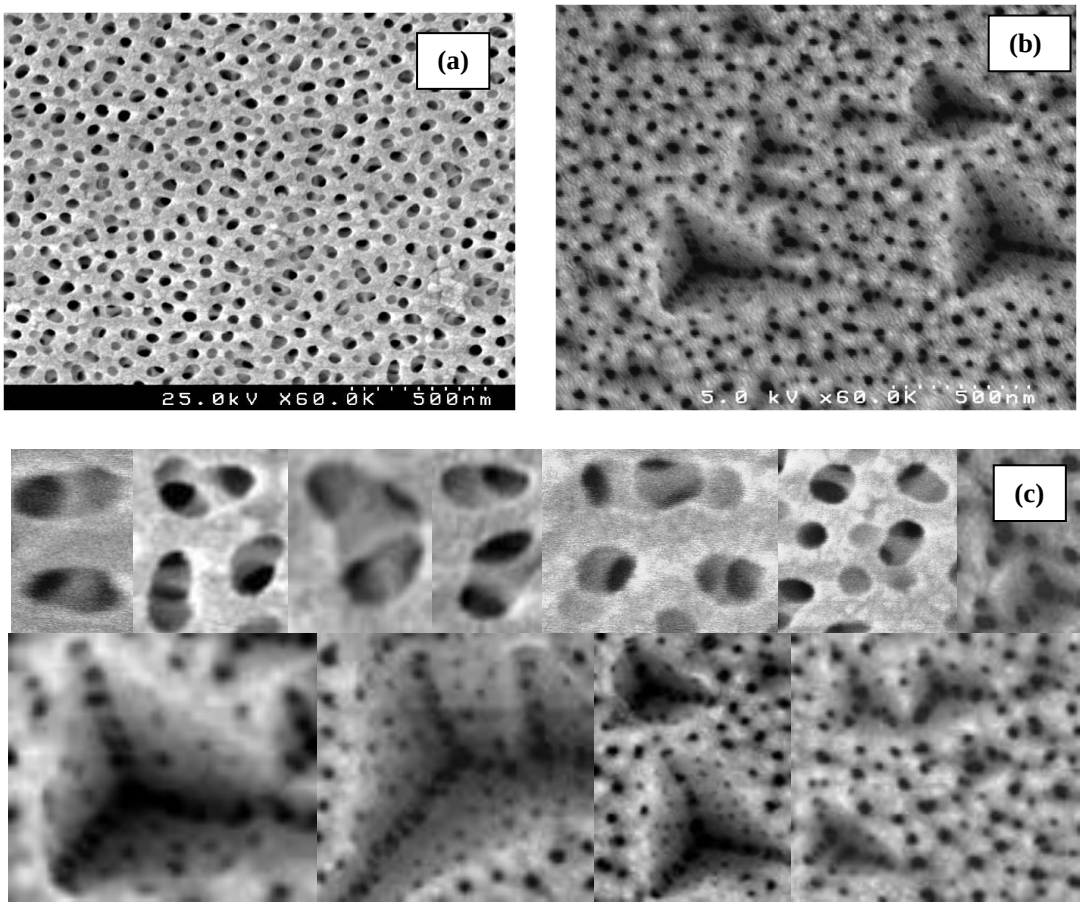

Figure 59 (a) Pore morphology (b) Over etching and (c) preferred growth direction of pore channels of SCAA oriented in [111] direction

3.11.1.2 Pore Morphology of SCAA [100]

Figure 60 shows the typical pore-side microstructures of an as-anodized SCAA disk oriented along [100] direction. It shows some initiated but uncompleted pores. Most of the sample surface area shows uniformly distributed pores. Unlike the above described [111] oriented disks where three oblique directions were the preferred directions for the pore growth, here the pore channels grow along random directions that are quite close to the [100] direction of [100] oriented samples. This strongly suggests that preferred pore growth direction for [100] oriented samples is along [100] direction.

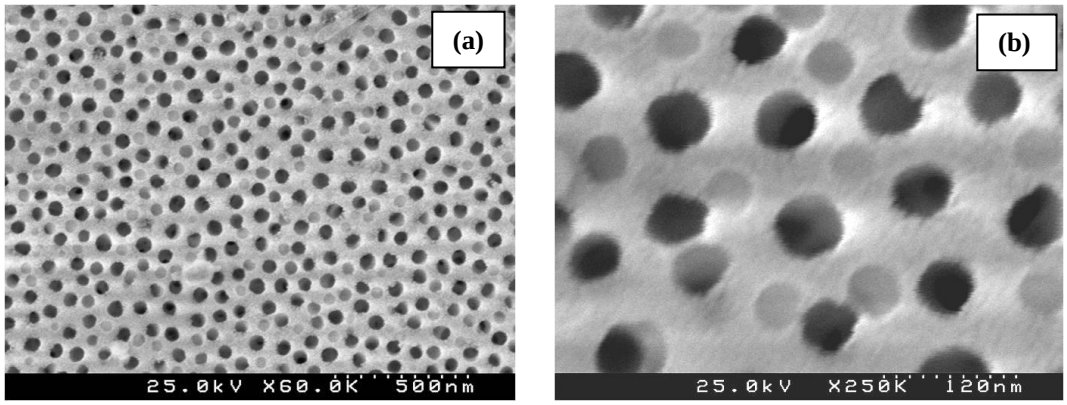

Figure 60 (a) Pore morphology (b) Close-up of the microstructure of of SCAA oriented in [100] direction

3.11.1.3 Pore Morphology of SCAA [110]

Pore morphology of SCAA oriented in [110] direction after anodization (figure 61) shows a uniform distribution of pores on the surface. However, they all appear to be elongated along one direction indicated by an arrow. This indicates the presence of a single preferred pore growth direction that is oblique to the [110] disk-normal.

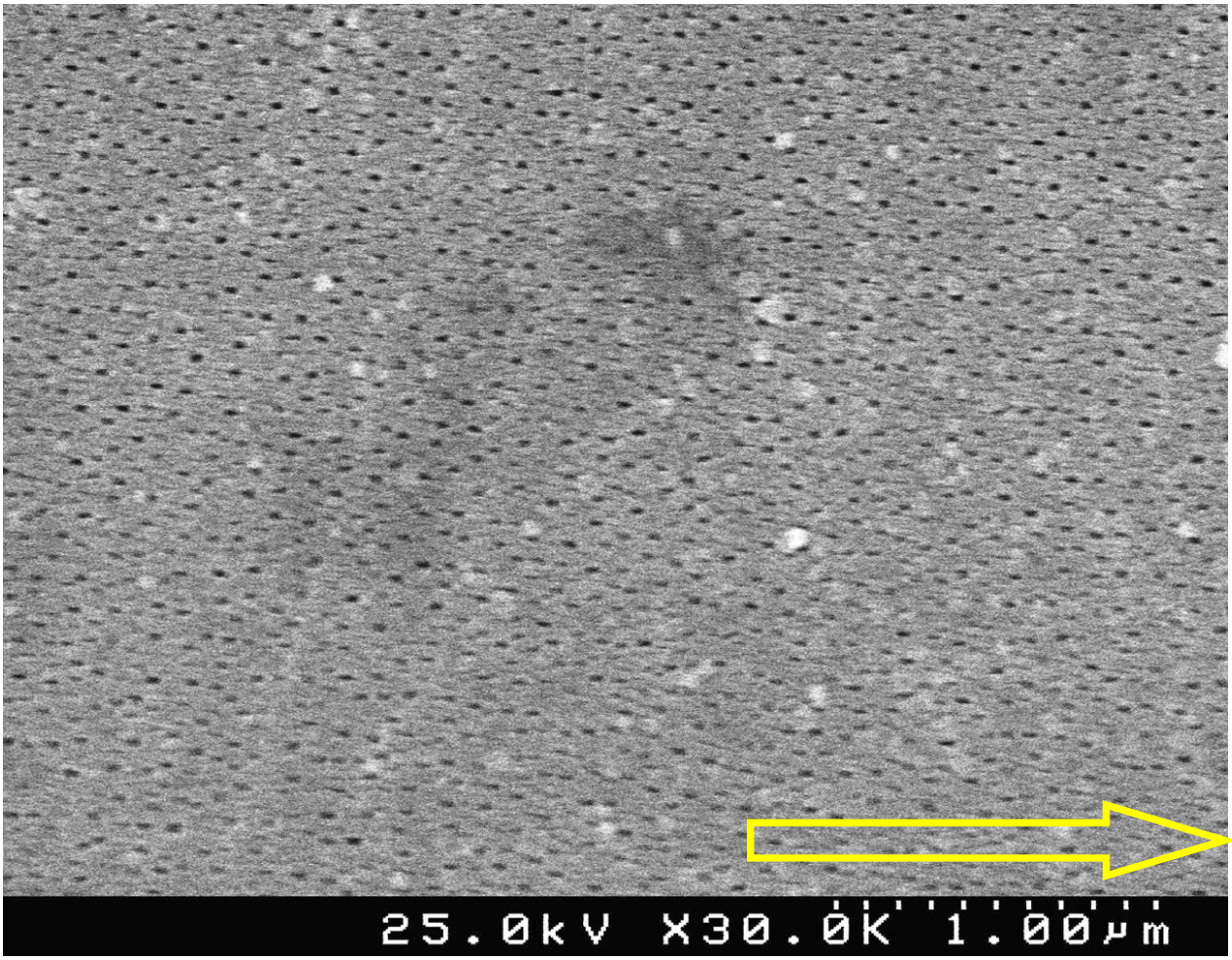

Figure 61 Pore morphology of SCAA oriented in [110] direction

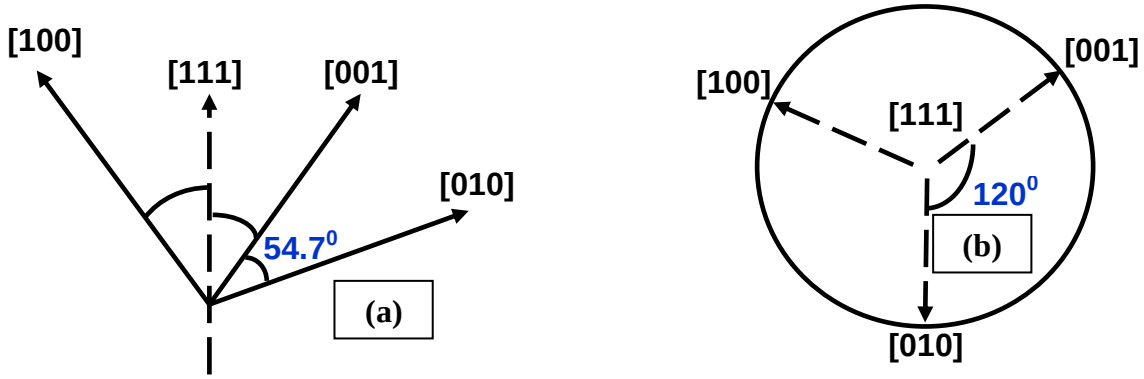

Figure 62 (a) Stereographic view of <100> directions and (b) Projections of <100> directions on (111) plane

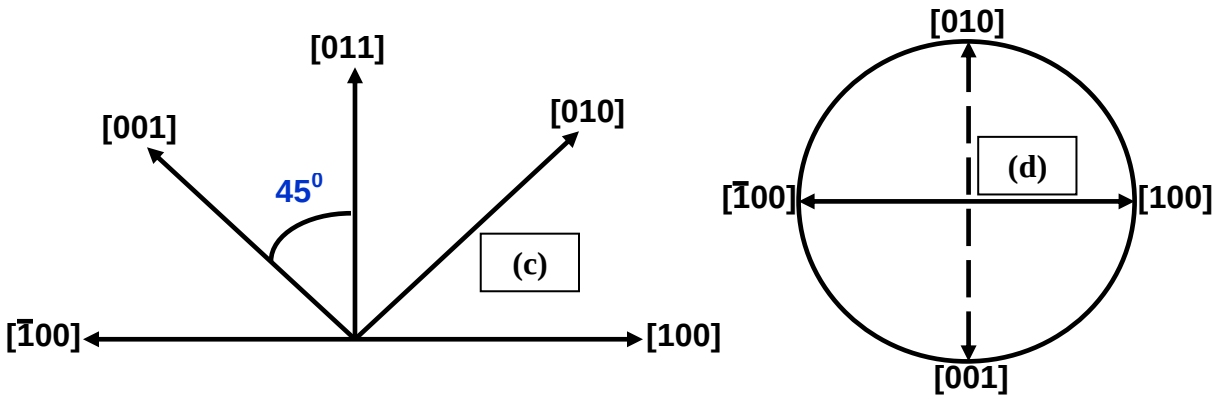

Figure 62 (c) Stereographic view of <100> directions and

(d) Projections of <100> on (011) plane

The schematic views shown in Figure 62 are based on the assumption that [100] direction is the preferred pore growth direction during anodization of aluminum. For a disk with its pore surface being (111) plane the three [100], [001] and [010] directions will be oriented at 54.7^{o} from the [111] directions like "spokes" of an umbrella, as shown in Figure 62 (a). Projections of these "spokes" on the (111) plane will appear to be at 120^{0} from each other. This is similar to the appearance of the three preferred directions on the anodized surface shown in Figure 62(b).

Figure 62 (c) shows the appearance of <100> directions for a sample that is orientated with its surface normal being parallel to [110] direction. Here the [001] and [100] "spokes" will form 45^{o} angle with respect to the [110] direction, and would produce projections on the (110) plane that runs along one line as schematically shown in Figure 62 (d). This is similar to the appearance of one preferred orientation of the pore growth on the anodized surface of the [110] anodized sample (Figure 60). The pores on the (100) plane will not show any preferred growth directions that are

significantly oblique to [100] direction. This is experimentally observed as shown in Figure 59.

3.11.2 Anodization Current Transient and Correlation to Pore Morphology

Physical processes occurring during anodization of aluminum are reflected in the time dependence of the anodization current. Figure 63 shows a schematic plot of the current density changes occurring during anodization [65].

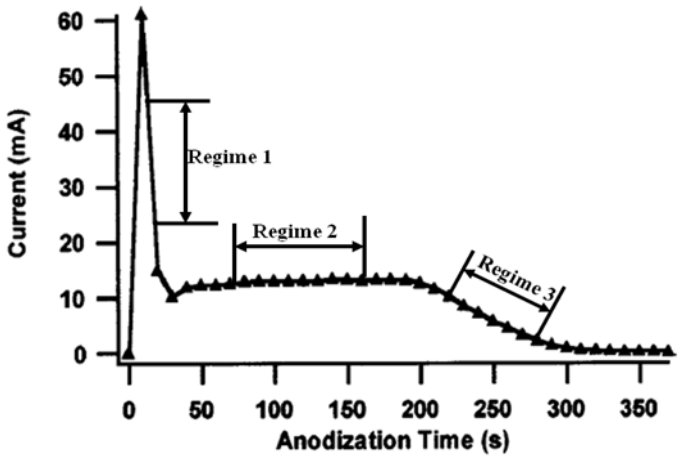

Figure 63 Typical current transient of aluminum during anodization

The Current initially peaks to a maximum value, and then it decreases to a minimum before reaching a steady-state value. The physical processes occurring during these three regimes are schematically shown in figure 64 [66]. During regime 1 a barrier layer of aluminum oxide forms on the surface of aluminum. Regime 2 is associated with localized dissolution of this aluminum oxide layer to form pores that are distributed on the surface of the oxide. By the end of the regime 2 an equilibrium is achieved between the rate of oxide formation and that of its dissolution. The pore spacing, their ordering and distribution get established by the end of regime 2. During regime 3 the pore channels elongate and grow into the aluminum metal.

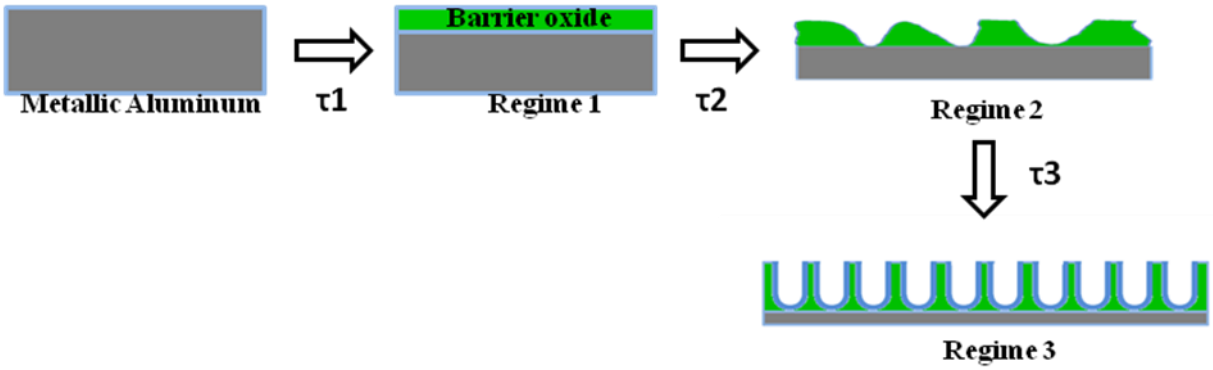

Figure 64 Formation of porous aluminum oxide from metallic aluminum

3.11.2.1 Current Density Transient Behavior of SCAA

Figure 65 shows the current density transients for the various SCAA samples. The current density values were obtained from the experimentally measured anodization current at 1-second interval and the corresponding sample cross-section areas; the area of SCAA 100 and SCAA110 samples was 0.9056 cm^2 while that of the SCAA 111 samples was 0.089 cm^2.

The three regimes mentioned earlier are identified in figure 63. The SCAA100 and SCAA110 samples typically exhibit the expected anodization current transient behavior while the SCAA111 samples show frequent spikes in regime 3. These current spikes were seen even during the rest of the regime-3 not shown in this figure; they were absent in SCAA100 and SCAA110. The frequent noise in current density for SCAA111 may be due to the etching of pore channels in more than one direction. Let us recall that <100> directions were attributed to be the preferred growth direction for aluminum anodization and pore formation (Section 5.1). Apparently the

anodization proceeds along one of the three <100> directions till another <100> direction gets kinetically favored for further anodization and pore growth. This process will make the pore formation (anodization) and growth process slower and energetically less favored for the [111] oriented samples. This is also evident by the observation that the current densities for the [111] oriented samples are higher as compared with those of the [100] and [110] directions (as shown in Figure 65).

Table XIII shows the measured values of the steady state current density (in regime three) and the total charge that has been used during the entire anodization process. The charge was calculated from the current versus time plots (Figure 66) for the various single crystalline samples by using the trapezoidal rule.

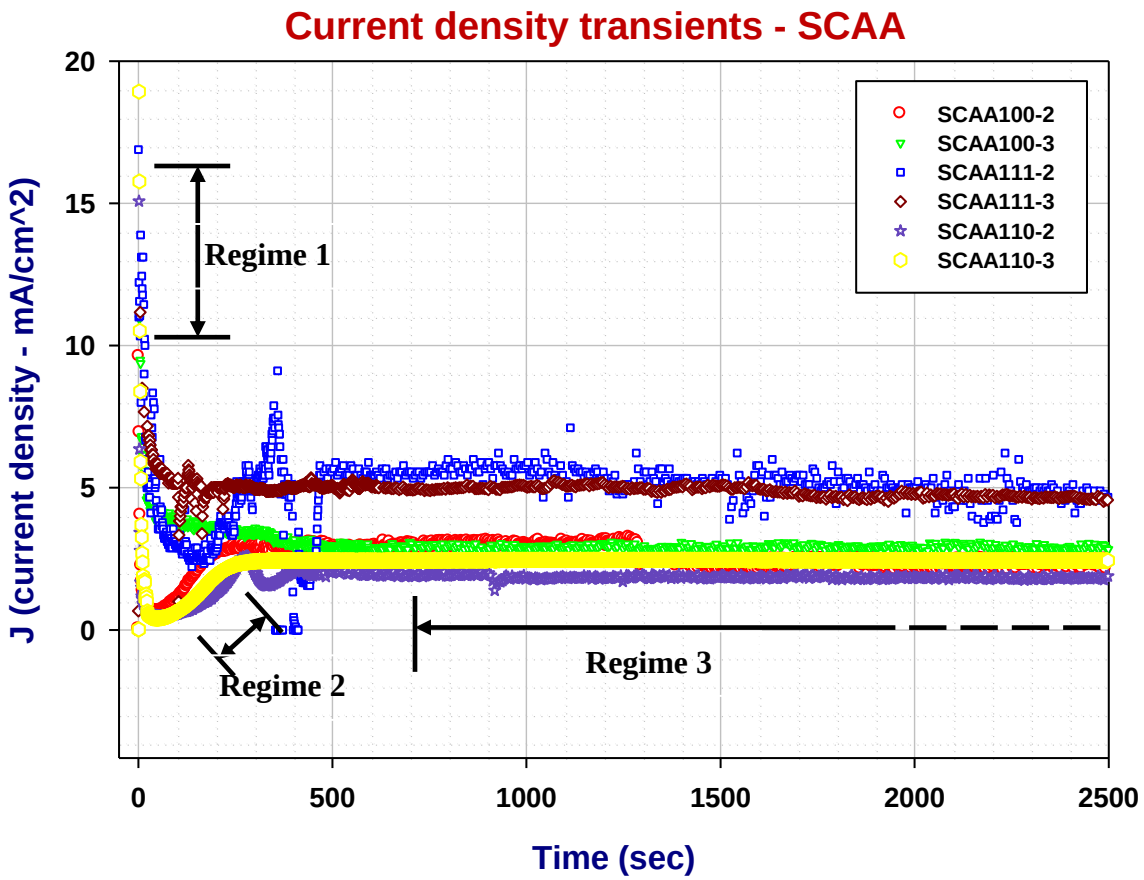

Figure 65 Current density transients SCAA – short time

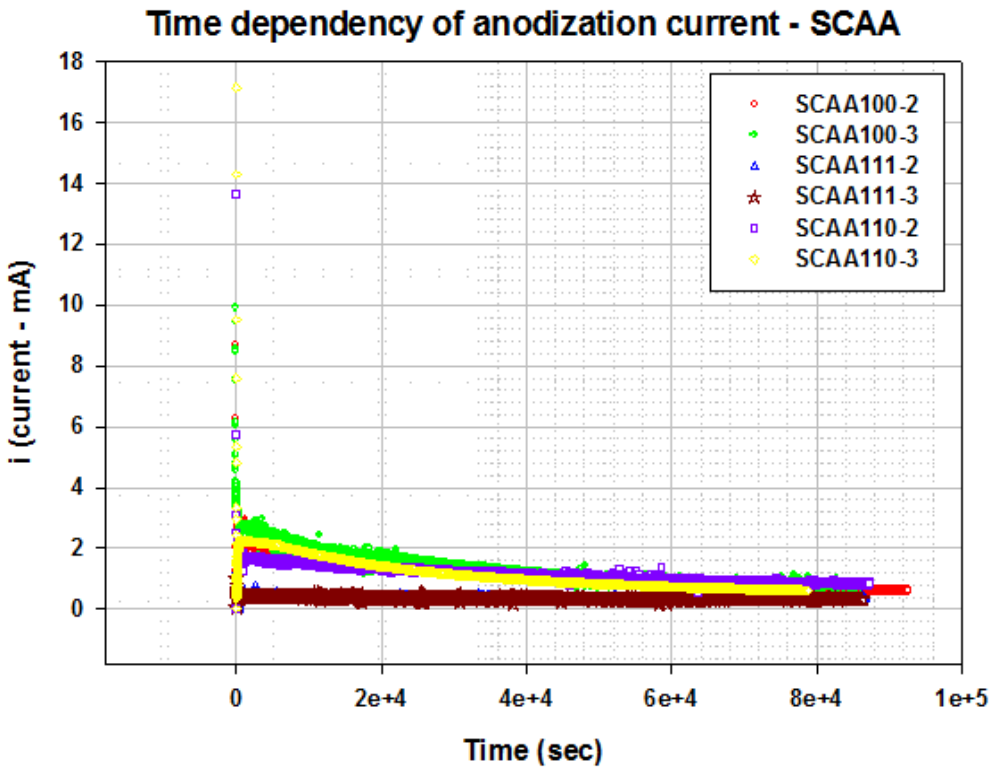

Figure 66 Current density transients SCAA – long time

Sample ID	Steady state Current density(mA/cm^2)	Area under curve (Coulombs)
SCAA100-2	1.2	109.12
SCAA100-3	1.4	119.37
SCAA110-2	0.8	105.64
SCAA110-3	0.9	111.22
SCAA111-2	4.2	36.03
SCAA111-3	3.5	24.96

Table XIII Current density parameters for SCAA, [100], [110] and [111]

The [111] oriented samples have the highest steady state current densities. The [110] and [100] oriented samples have similar current density values. Higher steady-state current density indicates more oxide volume formation per second.

3.11.2.2 Correlation of Current Density Behavior to Affinity of Anodization

Current density transient regions of increase and decrease were numerically fitted to an exponential time dependence curve to identify the "time constants" involved in these transients. Regimes 1, 2 and 3 were thus assigned characteristic time constants (τ_i) and the pre-exponential term (j_i) as given below.

$$j = j_1.\exp\left[\frac{-t}{\tau_1}\right] \tag{8}$$

$$j = j_2.\exp\left[\frac{-(t-t_1)}{\tau_2}\right] \tag{9}$$

$$j = j_3.\exp\left[\frac{-(t-t_2)}{\tau_3}\right] \tag{10}$$

The data close to the peak and valley locations were ignored to be able to fit the exponential curves. Figures 67 (a), (b) and (c) show the exponential fits obtained for the three crystal orientations. Table XIV lists the corresponding pre-exponential time constant values. Table XIV-a shows the crystallographic orientation dependence of the mean time constant τ parameters

Regime 1

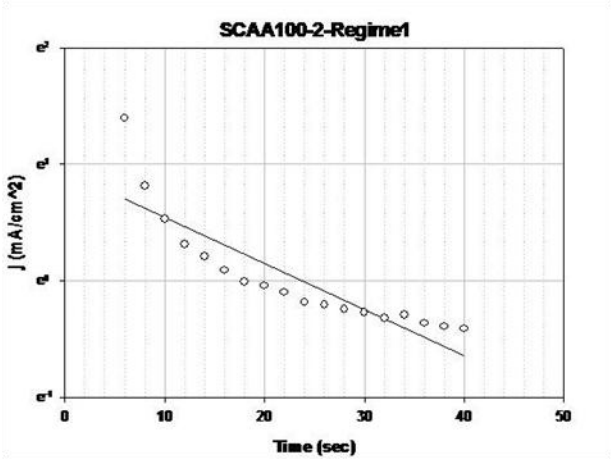
SCAA100-2-Regime1
J (mA/cm^2)
Time (sec)

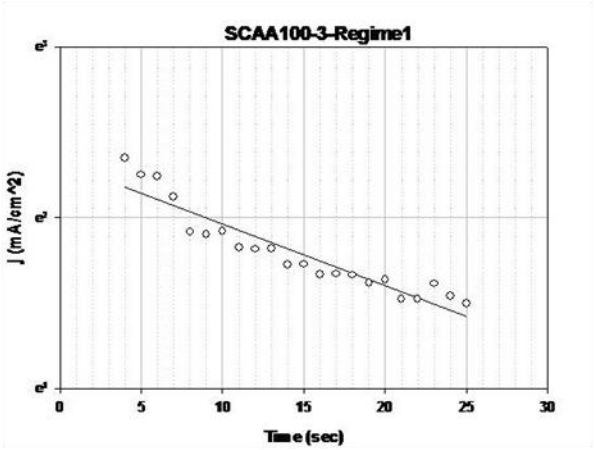
SCAA100-3-Regime1
J (mA/cm^2)
Time (sec)

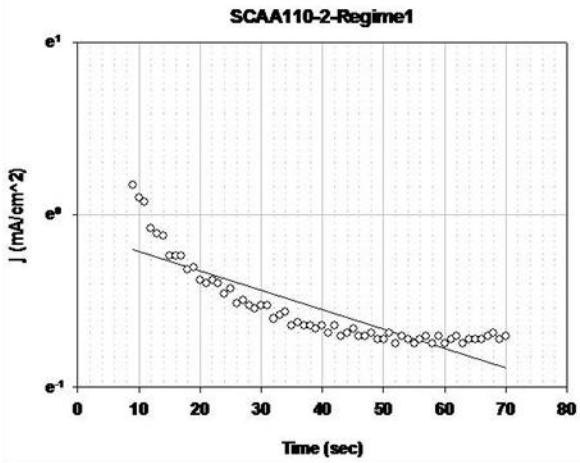
SCAA110-2-Regime1
J (mA/cm^2)
Time (sec)

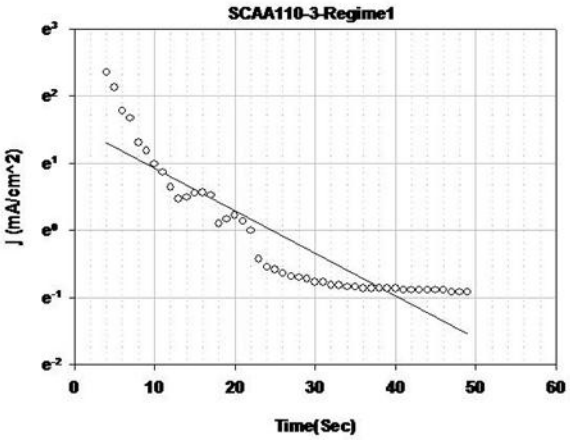
SCAA110-3-Regime1
J (mA/cm^2)
Time(Sec)

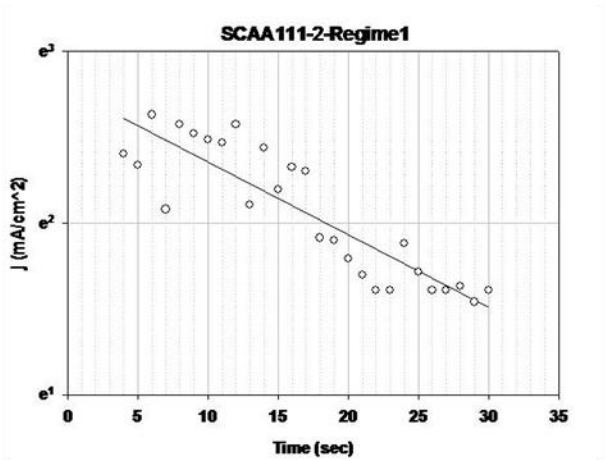
SCAA111-2-Regime1
J (mA/cm^2)
Time (sec)

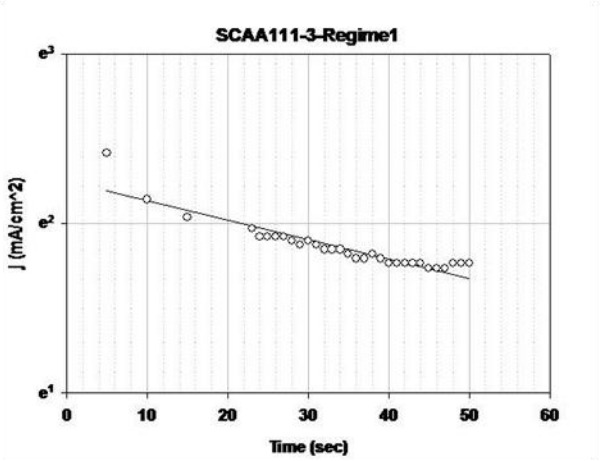
SCAA111-3-Regime1
J (mA/cm^2)
Time (sec)

(a) Regime 2

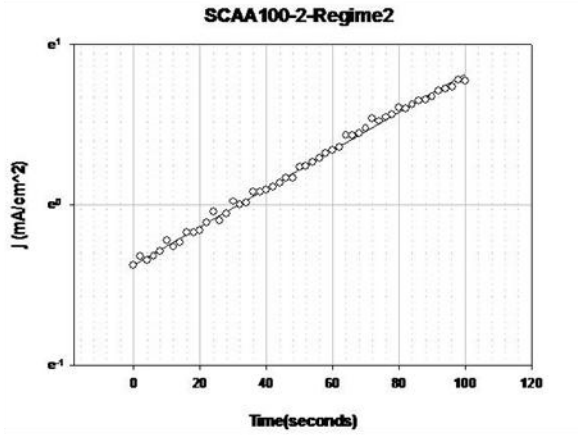
SCAA100-2-Regime2
J (mA/cm^2)
Time(seconds)

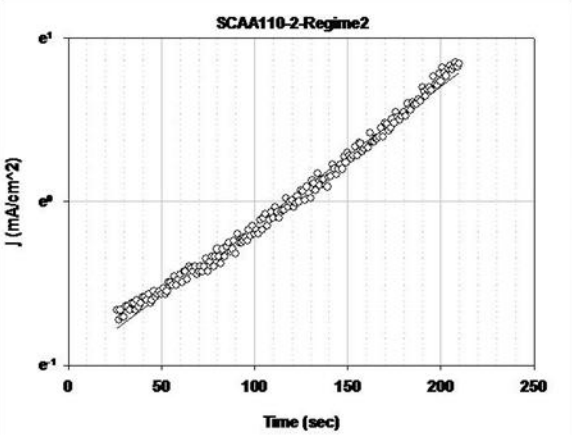
SCAA110-2-Regime2
J (mA/cm^2)
Time (sec)

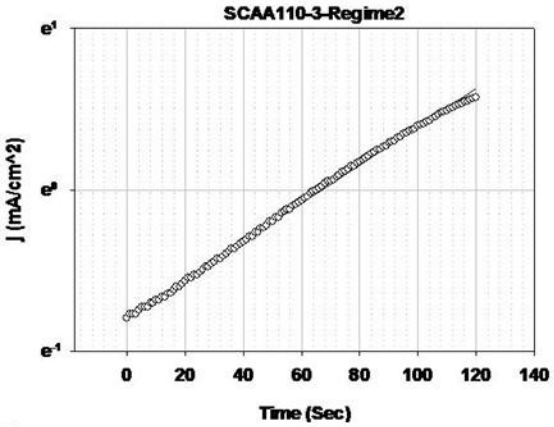
SCAA110-3-Regime2
J (mA/cm^2)
Time (Sec)

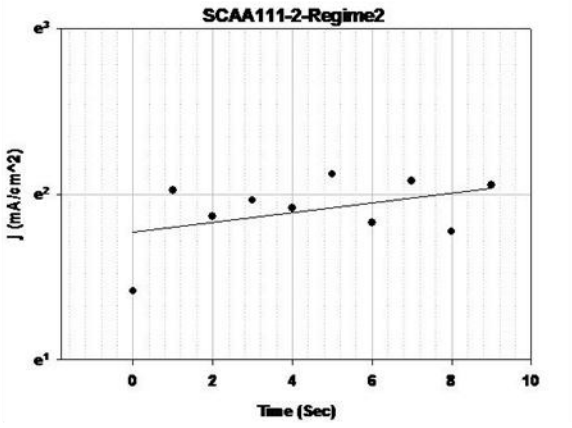
SCAA111-2-Regime2
J (mA/cm^2)
Time (Sec)

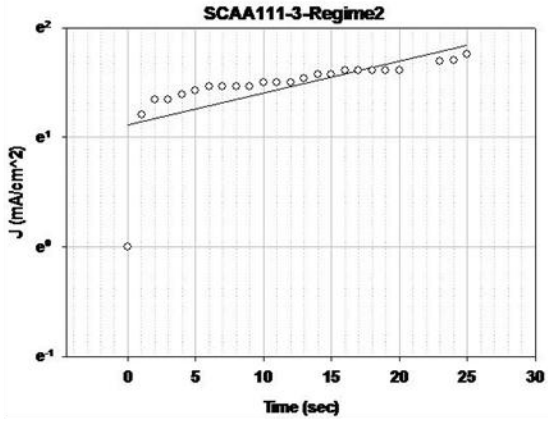
SCAA111-3-Regime2
J (mA/cm^2)
Time (sec)

(b) Regime3

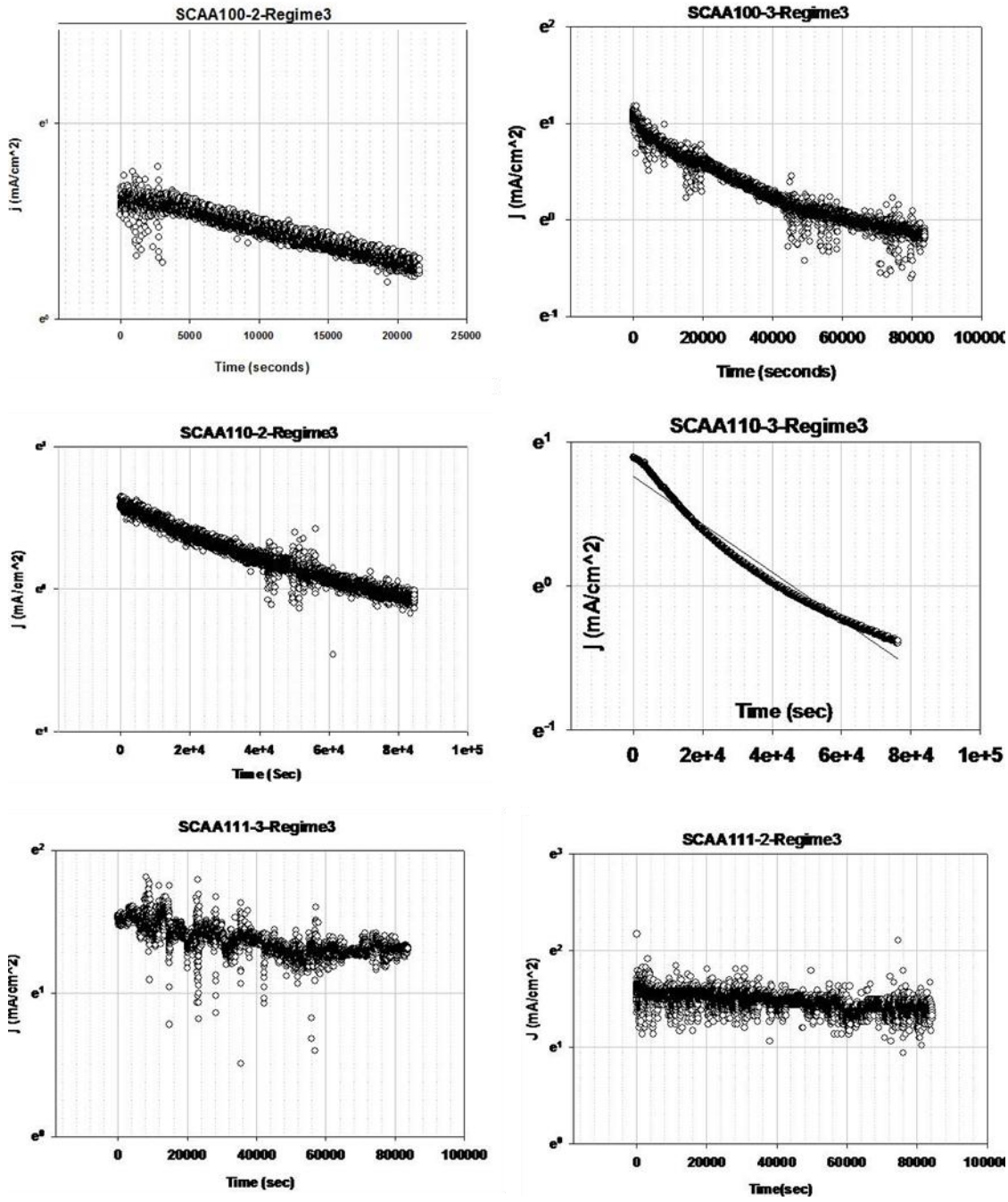

Figure 67 Curve fitting of current transient data - SCAA

Sample ID	τ_1(sec)	τ_2(sec)	τ_3(sec)	j1(mA/cm^2)	j2(mA/cm^2)	j3(mA/cm^2)
SCAA100-2	25.4	178.6	72568.94	2.5	0.9	2.3
SCAA100-3	27.6	-	74074.07	10.1	-	2.3
SCAA110-2	52.6	123.7	128865.98	1.3	0.3	1.7
SCAA110-3	15.7	95.3	60161.23	4.7	0.4	2.1
SCAA111-2	33.5	33.8	416545.17	16.0	5.8	4.7
SCAA111-3	47.03	34.4	339213.03	9.4	3.0	4.4

Table XIV Current density time constants – SCAA

Sample ID	τ_1 (sec)	τ_2 (sec)	τ_3(sec)
SCAA100	26.6	178.6	73321.5
SCAA110	34.2	109.5	94513.6
SCAA111	40.3	34.2	377879

Table XIV-a Average Current density transient constants - SCAA

Surface barrier oxide forms on metallic aluminum during Regime 1. The value of τ_1 is the time required for the barrier layer oxide to form on the surface of aluminum. A lower value of τ_1 for a material indicates that it has a tendency to form aluminum oxide quickly. The time constants τ_1 for the three crystallographic orientations show the following order (Table XIV-a): $(\tau_1)_{100} < (\tau_1)_{110} < (\tau_1)_{111}$. It shows that aluminum single crystal disks oriented along the [100] direction have the highest tendency to anodize while those along [111] direction have the lowest tendency.

Formation of aluminum oxide and its dissolution are the two simultaneous processes which occur during oxidation in aluminum. Pore morphology will be dependent on the competition between the rates of these two processes. The rate of formation of oxide will be highest for SCAA100 and hence the localized dissolution

of the oxide will be slower. This behavior is shown by the following ordering of the time constants, τ_2, $(\tau_2)_{100} > (\tau_2)_{110} > (\tau_2)_{111}$. Time constant τ_2 is an indication of how quickly the oxide dissolves to form pores on the surface of the barrier layer oxide formed during regime-1. Since the [100] oriented samples form the oxide most readily they are also expected to dissolve most slowly; this is indicated by the above τ_2 ordering.

A steady-state competition is established between the processes of oxide growth and its dissolution occurring simultaneously during Regime 3 leading to a continued pore formation and its growth during most of the anodization process. Time constant τ_3 is an indication of thed time required for the pore channels to reach such a steady-state behavior. The order of τ_3 for the single crystal samples, $(\tau_3)_{100} < (\tau_3)_{110} < (\tau_3)_{111}$ showing the least τ_3 value for [100] oriented samples (Table XIV-a) also indicates that [100] direction is likely to be the preferred pore growth direction. The slower pore growth kinetics is expected from the SCAA [111] samples since pore channels have a tendency to grow along three oblique directions as seen in section 4.7.1 and Figure 58.

3.11.3 Statistical Analysis of Pore Parameters – SCAA

Pore parameters have been statistically determined using the weighted cm(x, y) technique as described earlier. All minimum spanning tree and voronoi polygons from the statistical analysis of SCAA materials are shown in Appendix C. Figure 68 shows the pore diameter frequency distribution fitted using a three-parameter modified Gaussian curve fit equation shown below:

$$y = a.\exp\left\{-0.5\left[\frac{|x - x_0|}{b}\right]^2\right\} \qquad (11)$$

where, a is the peak height, x_0 represents the mean, and b represents the standard deviation.

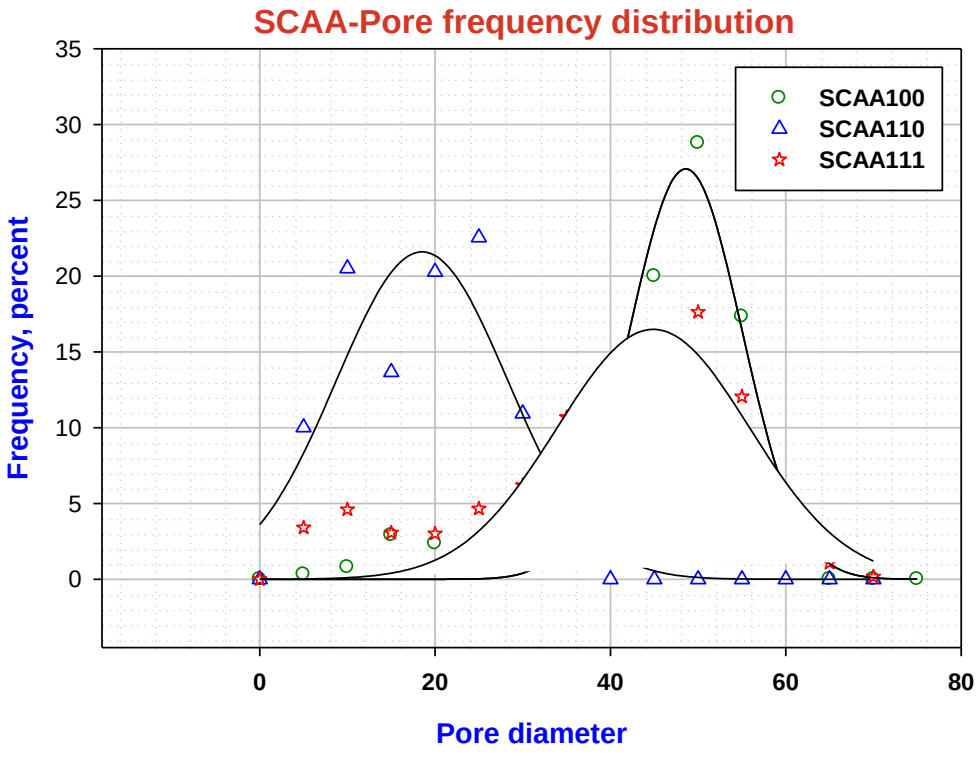

Figure 68 Pore frequency distribution of SCAA

Table XV shows the pore size, pore spacing, mean nearest neighbor spacing, porosity and pore density determined for all the anodized single crystal aluminum materials. The dependency of pore morphology and the distribution on the direction of crystallographic orientation was examined by comparing the values of pore parameters in Table XV. Table XVI shows the resultant increasing order of pore parameters for the single crystalline materials.

Sample ID	Pore size (nm)	MST Inter-Pore spacing(nm)	Mean nearest neighbor Spacing (nm)	Porosity (%)	Pore density (m^{-2})
SCAA100	38.03±11.13	70.87±14.58	63.24±14.3	15.18	2.04E±14
SCAA110	21.19±7.01	44.36±9.56	45.72±11.36	2.8	6.29E±13
SCAA111	30.79±12.92	59.92±15.81	52.32±18.13	10.38	1.69E±14

Table XV Pore parameters evaluated from statistical analysis

Pore parameter	Order of crystallographic orientation
Pore size	[110]<[111]<[100]
Mean Nearest Neighbor spacing	[110]<[111]<[100]
Porosity	[110]<[111]<[100]
Pore density	[110]<[111]<[100]

Table XVI Effect of crystallographic orientation on pore parameters

All SCAA materials were fabricated under identical processing conditions except for the crystallographic orientations of the three types of samples. One-way ANOVA statistical tests performed on the pore size and nearest neighbor spacing showed that the [100], [110] and [111] directions data were significantly different from each other. This is shown in analysis in Appendix D. These results show that [100] oriented samples had the highest pore size, pore spacing, porosity and pore density followed

by the [111] and [100] oriented samples. This difference in pore morphology and distribution can be attributed to the hypothesis that [100] is the preferred growth direction for pores during anodization of aluminum as discussed in section 3.9.1.

3.11.3.1 Number of Nearest Neighbor Distribution for SCAA Materials

The number of nearest neighbor distribution was obtained for all single crystal alumina materials from the VORONOI polygons included in Appendix C. Figure 69 shows the nearest neighbor distribution for single crystal alumina materials SCAA100, SCAA110 and SCAA111 . Table XVII shows the values of a, b and x_0 for the Gaussian regression of the nearest neighbor distribution showing that the pore ordering is optimally hexagonal for [100] and [111] directions. The mean number of nearest neighbors for SCAA oriented in [110] direction is higher than six suggesting that the pore distribution significantly deviates from hexagonal ordering for the [110] oriented samples.

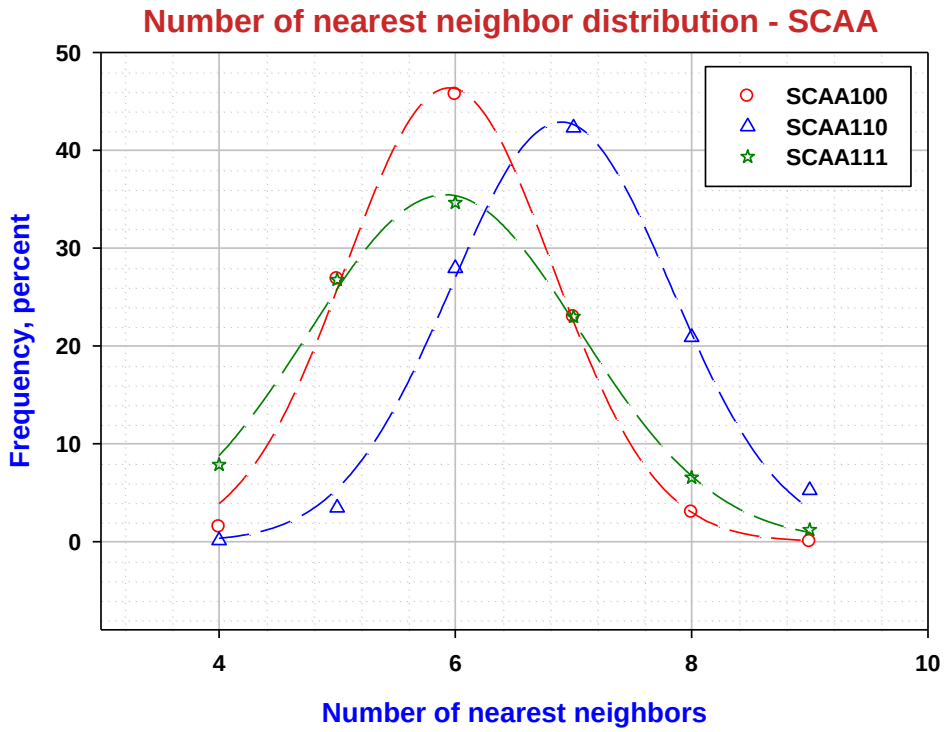

Figure 69 Number of nearest neighbor distribution for SCAA

Single crystal	a	b	x_0
[100]	46.36	0.875	5.94
[110]	42.87	0.932	6.89
[111]	35.44	1.14	5.91

Table XVII Gaussian peak parameters for SCAA nearest neighbor distribution

3.11.3.2 Pore Ordering for SCAA Materials

Table XVIII shows the values of m* and σ* for the SCAA materials oriented in the three directions [100], [110] and [111] obtained from the MST analysis of SCAA materials as described earlier. Figure 70 shows the plot of m versus σ for all SCAA. This figure demonstrates that SCAA100 and SCAA111 have the lowest degree of

disorder compared to the SCAA110. SCAA110 samples appear to have the lowest degree of hexagonal pore ordering since m-σ correlation for these materials lies farthest away from an ideal hexagonal tessellation.

	m*	sigma*	N	A	m	sigma
SCAA100	79.61	10.18	1276	10501800	0.87	0.112
SCAA110	39.56	10.21	925	2145653	0.82	0.211
SCAA111	58.66	10.06	2097	9541868	0.87	0.149

Table XVIII m, σ values of SCAA materials

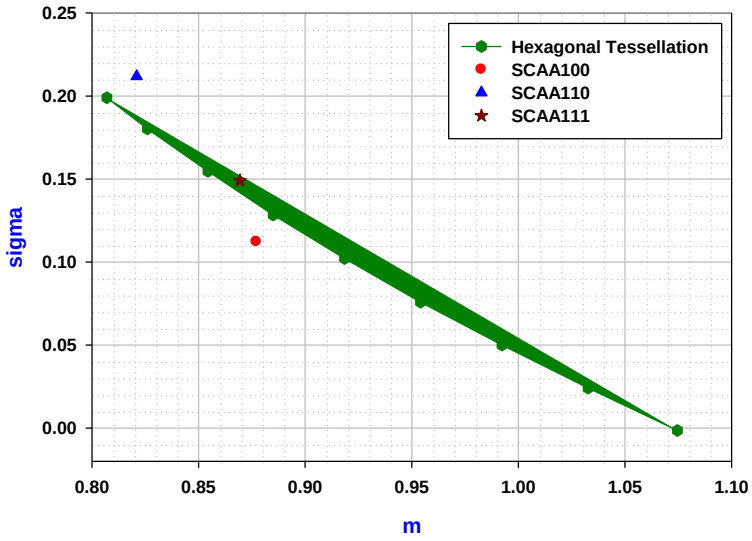

Figure 70 m versus σ plot of SCAA materials

CHAPTER IV

CONCLUSIONS

4.1 Growth of Porous Alumino-Silicates and Electro-deposition of Metal into Pores

Following are the conclusions for the growth of porous alumino-silicates on various metallic and non-metallic substrates:

(i) Silicalite grows in the form a uniform layer compared to the distributed particulate growth of faujasite on all metallic substrates.

(ii) Sintered copper showed better faujasite growth compared to the anodized titanium and NaOH treated titanium.

(iii) Metal phase was found to be growing in faujasite film grown *in-situ* on anodized titanium.

(iv) Diluting the reaction chemistry four-fold led to a two-fold increase in the aspect ratio of silicalite crystals and more distinct particle growth for faujasite.

(v) Mesoporous silica was found to grow in the form of a uniform film on anodized aluminum while it grows as a thin layer on both sintered copper and anodized titanium.

(vi) Commercial alumina Anodisc® was also shown to develop a uniform layer of mesoporous silica covering half the surface area.

4.2 Fabrication of Nano-porous Anodic Alumina Membranes and their Characterization

Polycrystalline anodic alumina (PCAA) and single crystalline anodic alumina materials (SCAA) oriented in three directions, [111], [100] and [110], were fabricated by anodization in 0.3 M oxalic acid at 7^0C. Free-standing PCAA with thru porosity were characterized for pore morphology parameters of the anodic alumina. Statistical analysis showed that PCAA has most uniform ordering at 40V. Following conclusions were obtained:

(i) Experimental reproducibility and reliability of fabrication of PCAA was established by statistical analysis of several samples fabricated under identical conditions.

(ii) Pore morphology examination on the pore side of SCAA revealed that [100] is the preferred growth direction.

(iii) Estimation of anodization current time constants and statistical analysis of pore morphology parameters for SCAA concluded that [100] orientation had the highest tendency to anodize and form porous aluminum oxide.

CHAPTER V

PROPOSED FUTURE RESEARCH

Aluminum and titanium metals have been reported to produce a surface oxide with porous morphology by oxidizing under a specific set of electrolytic conditions. It is likely that this technique can also be applied to other metals such as tantalum, niobium, molybdenum and tungsten to form nano porous surface morphology. There is a need to establish optimum anodization processing conditions for these other alloys also, as it would allow a range of substrate and oxide surfaces to be examined for many potential applications.

The “cap-side” of the single crystal [100],[110] and [111] anodized samples, and fractured surfaces along the disk-thickness should be examined in order to investigate whether the preferred pore growth tendency along the [100] direction is also retained along the entire anodization process.

BIBLIOGRAPHY

1. Toru Wakihara, Akira Sugiyama, Tatsuya Okubo, *Microporous and Mesoporous Materials*, Volume 70, 2004, p 7–13
2. IZA structure commission – *Database of Zeolite Structures* – online resource http://izasc.ethz.ch/fmi/xsl/IZA-SC/ft.xsl
3. J. S. Beck, J. C. Vartuli, W. J. Roth, M. E. Leonowicz, C. T. Kresge, K. D. Schmitt, C. T. W. Chu, D. H. Olson, E. W. Sheppard, *Journal of American Chemical Society*, Volume 114, issue 27, 1992, p 10834-10843
4. T Sano, Y Kiyozumi, K Marda, M Toba, *Journal of materials chemistry*, Volume 2, 1992, p 141-142
5. S.P Davis, E.V.R Borgstedt, S.L Suib, *Chemistry of Materials*, Volume 2, 1990, p. 712-719
6. E R Geus, Van Bekkum, *Zeolites*, Volume15, 1995,p. 333-341
7. Magdalena Lassinantti, Synthesis, Characterization and properties of Zeolite membranes, Thesis – Lulea university of technology, Lulea, Sweden
8. Jonas Hedlund, Brian J Schoeman, Johan Sterte, *Studies in surface science and catalysis*, Volume 105,1997, pp 2203-2210
9. Ann M Goossens, Gina Vanbutsele, Johan A Martens, *FOA6*, May 1998, p 24-28
10. JC Jansen, W Nugroho and H Van Bekkum, Proceedings of 9th International zeolite conference, Editors: R Von Ballmoos, J.B.Higgins and MMJ Treacy, Butterworth-Heinemann, Stoneham, MA, 1992, p.247
11. D Kashchiev, JC Jansen, A Erdem senatalar, *Stud in surface science and catalysis*, Volume 85, 1994, p. 215-250

12. Wan Cheong Wong, Louisa Tak Yin Au, Carlos Tellez Ariso, King Lun Yeung *Journal of Membrane Science,* Volume 191, 2001, p.143–161

13. Toshikazu Nishide, Takashi Hamatsu, Yoshimichi Kiyozumib and Fujio Mizukami, *Journal of Materials Chemistry,* Vol.12, 2002, p.1465–1468

14. S P J Smith, V M Linkov, R D Sanderson, L F Petrik, C T O'Connor, K Kieser, *Microporous Materials,* 1995,Volume4, pp 385-390

15. European Patent Applications

    (a) Bratton G J, Devilliers Naylor T, *EP 481658 Al,* 1992

    (b) Barri S A I, Bratton G J, Tomkinson J D, *EP 481659 Al,* 1992

    (c) Barri S A I, Bratton G J, Devilliers Naylor T, *EP 481660 Al,* 1992

16. M. J Cheng, W.S.Yang, , X. S Li, Y.S.Yang, Y.D Xu, L.W. Lin, *Cuihua Xuebao*, 1995,Volume16, p.8990

17. A. Sayari, Y. Yang, M. Kruk, and M. Jaroniec, *Journal of physical chemistry B*, Volume103, 1999, p.3651-3658.

18. Q. Huo, D. I. Margolese and G. D. Stucky, *Chemistry of Materials*,Volume 8, 1996,p.1147-1160.

19. Anjie Wang and Toshiaki Kabe, *The Royal society of chemistry*, 1999, p.2067–2068

20. Hong Yang, Gregory Vovk, Neil Coombs, Igor Sokolov and Geoffrey A. Ozin, *Journal of Materials Chemistry*, 1998, Volume 83, p. 743–750

21. Qisheng Huo, Jianglin Feng, Ferdi Schuth, and Galen D. Stucky, *Chemistry of Materials,* 1997,Volume9, 14-17

22. P.Yang, D.Zhao, B.F Chmelka, G. D Stucky, *Chemistry of Materials*, Volume 10, 1998, p. 2033-2036.

23. Q. Huo, D. Zhao, J. Feng, K. Weston, S.K Buratto, G.D Stucky, S. Schacht, F.Schuth,. *Advanced Materials,* Volume *9*, 1997, p. 974-979.

24. P. J.Bruinsma, , A. Kim, ,J. Liu,S. Baskaran, *Chemistry of Materials*,Volume 9, 1997, p.2507-2512.

25. Canon technology – Mesoporous materials – online resource http://www.canon.com/technology/canon_tech/explanation/mesoporous.html

26. M Ogawa. *Journal of American Chemical Society*, Volume *116*, 1994, p.7941-7942.

27. M Ogawa. *Chemical Communications*, 1996, p.1149-1150.

28. M Ogawa., T. Igarashi, K. Kuroda, *Bulletin of Chemical Society of Japan*, Volume *70*, 1997, p. 2833-2837.

29. M Ogawa, *Langmuir*, Volume 13, 1997, p. 1853-1855.

30. M Ogawa., H. Ishikawa, T. Kikuchi, *Journal of Materials Chemistry*, Volume 8, 1998, p. 1783-1786.

31. H Yang., A. Kuperman, N. Coombs, S. Mamiche-Afara,G.A Ozin, *Nature*, Volume 379, 1996, p. 703-705.

32. H Yang., N. Coombs, I.Sokolov, G.A Ozin, *Nature*, Volume *381*, 1996, p. 589-592.

33. H Yang., N. Coombs,O. Dag, I. Sokolov, G.A Ozin, *Journal of Materials Chemistry*, Volume 7, 1997, p.1755-1761.

34. H Yang., N. Coombs, G.A Ozin, *Journal of Materials Chemistry,*Volume 8, 1998, 1205-1211.

35. H Yang., G.A Ozin, C. Kresge, *Advanced Materials*, 1998, *10*, 883-887.

36. H Yang., N. Coombs,O. Dag, I. Sokolov, G.A Ozin, *Journal of Materials Chemistry*, 1997, *7*, 1285-1290.

37. I.A Aksay, M. Trau, S. Manne, I. Honma, N. Yao, L. Zhou, P. Fenter, P.M Eisenberger, S M. Gruner, *Science*, Volume 273, 1996, p.892-898.

38. S.H Tolbert, T.E Schaffer, J Feng, P.K Hansma, G.D Stucky, *Chemistry of Materials*, Volume 9, 1997, p.1962-1967.

39. S. Schacht, Q. Huo, I.G. Voigt-Martin, G.D Stucky, F. Schuth, *Science*, Volume 273, 1996, p.768-770.

40. C. J. Brumlik and C. R. Martin, *Analytical Chemistry*, Volume 64, 1992, p. 1201-1203

41. S. A. Gavrilov, V. V. Gusev, V. S. Dneprovskii, E. A. Zhukov, A. N. Syrnikov, I. V. Yaminskii, and E. A. Muljarov, *JETP Letters*, Volume 70, 1999, p.216-221

42. H. Masuda, M. Ohya, H. Asoh, M. Nakao, M. Nohtomi, and T. Tamamura, *Japan Journal of Applied Physics, Part 2*, Volume 38, 1999, L1403-L1405

43. P. R. Evans, G. Yi, and W. Schwarzacher, *Applied Physics Letters*, Volume76, 2000, p.481-483.

44.Guowen Meng, Anyuan Cao, Ju-Yin Cheng, Aravind Vijayaraghavan, Yung Joon Jung, Mutsuhiro Shima, and Pulickel M. Ajayan, *Journal of applied physics*, Volume 97, 2005, p. 064303-064303-5

45. D. Crouse, Y. H. Lo, A. E. Miller, and M. Crouse, *Applied Physics Letters*, Volume 76, 49-51, 2000

46. A. P. Li, F. Müller, A. Birner, K. Nielsch, and U. Gösele, *Journal of applied physics*, Volume 84, 1998, p.6023-6026,

47. H. Masuda, H. Yamada, M. Satoh, H. Asoh, M. Nakao, and T. Tamamura, *Applied Physics Letters*, Volume 71, 1997, p.2770-2772

48.Yufei Jia, Haihui Zhou, Peng Luo, Shenglian Luo, Jinhua Chen, *Surface & Coatings Technology*, Volume 201, 2006, p.513–518

49.C.Y.Han, Z.L.Xiao, H.H.Wang, G.A.Willing, U.Geiser, U.Welp, W.K.Kwok, S.D.Bader, G.W.CrabTree , *Plating and Surface Finishing*, Volume91, July 2004, p 40-45

50. Wei Chen, Jian-Shuang Wu, Jin-Hua Yuan, Xing-Hua Xia**,** *Journal of electroanalytical chemistry*, Volume 600, 2007, pp. 257-264

51. A. P. Li, F. Müller, and U. Gösele: *Electrochemical and Solid-State Letters*, Volume 3, 2000, p. 131-134

52.Y. T. Pang, G. W. Meng, W. J. San, L. D. Zhang, X. Y. Gao, A. W. Zhao, and Y. Q. Mao, *Applied Phyic. A: Material Science Process*, Volume 77, 2003, p. 717-719

53. H. Masuda and M. Satoh, *Japan Journal of Applied Physics*,Part 1, Volume 35, 1996, p.L126-L129,

54. Hideki Masuda and Kenji Fakuda, *Science*, Vol 268, June 1995, p. 1466 – 1468

55. Hideki Masuda and Fumio Hasegwa, *Journal of Electrochemical Society*, volume 144, No.5, 1997, p. L127-L130

56. O. Jessensky, F. Muller and U. Gosele, *Applied physics letters* volume 72, number 109 March 1998, p. 1173-1175

57. Smita Gohil, Ramesh Chandra, Bhagyashree Chalke, Sangeeta Bose and Pushan Ayyub *Journal of Nanoscience and technology*, Volume7, p.641-647, 2007

58. Long Ba and Wei Sang Li *Journal of Physics D: Applied Physics*, Volume33, 2000, p.2527–2531

59. Jörg J. Schneider, Jörg Engstler, Karl P. Budna, Christian Teichert and Steffen Franzka, *European Journal of Inorganic Chemistry*, 2005, p.2352–2359

60. Hongbin Xu – 'Synthesis of ZSM-5, silicalite, and X zeolite films under elevated gravity and their characterization' – Doctoral dissertation, Cleveland State Univeristy, Cleveland, OH.

61. Kruk M, Jaroniec M, Sakamoto Y, Terasaki O, Ryoo R, Ko CH, *Journal of Physical Chemistry B*, Volume 104, 2000, p. 292-301

62. G. D. Sulka, S. Stroobants, V. Moshchalkov, G. Borghs, and J.-P. Celis, *Journal of the Electrochemical Society*, Volume149, 2002, p. D97-D103

63. S.N. Tewari, Y-Hsuan Weng, G.L. Ding and R. Trivedi, *Metallurgical and Material Transactions A*, Volume 33A, 1999, pp.1229-1243

64**.** Woo Lee, Ran Ji, Ulrich Gosele, Kornelius Nielsch **,** *Nature Materials*, Volume5, September 2006, p 741-747

65. Paul G Miney, Paula E Colavita, Maria V Schiza *Electrochemical and Solid-State Letters*, Vol. 610, 2003, p.B42-B45

66. Jinsub Choi, Fabrication of Monodomain Porous Alumina using Nanoimprint Lithography and its Applications, Doctoral dissertation, Martin Luther University, Halle-Wittenberg, Germany.
67. "Morphology of Directionally Solidified Pb-Sb Alloys", Lu Yu, Doctor of Engineering dissertation, 2001, Cleveland State University, Cleveland, OH.
68. V. V. Konovalov G. Zangari, and R. M. Metzger, *Chemistry of materials*, Volume 11, 1999, p.1949–1951

APPENDIX

Appendix A

MST and VORONOI images for PCAA fabricated at various voltages

30V – Pore

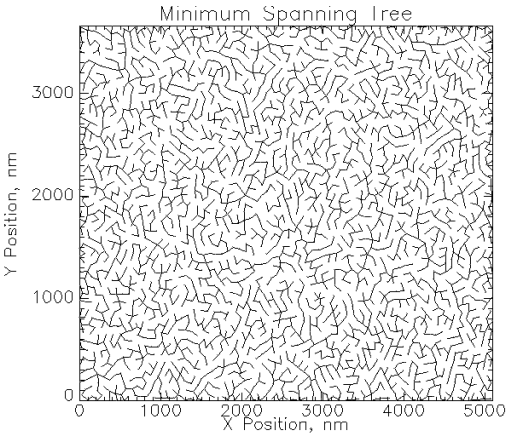

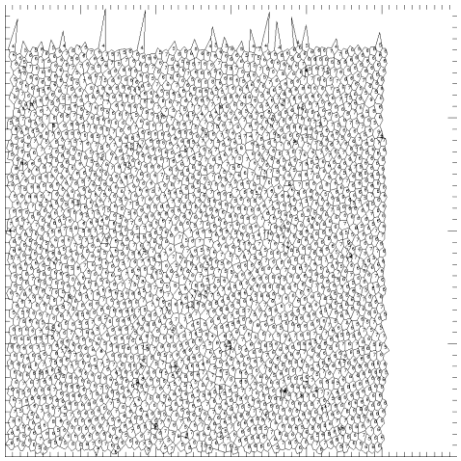

30V – Cap

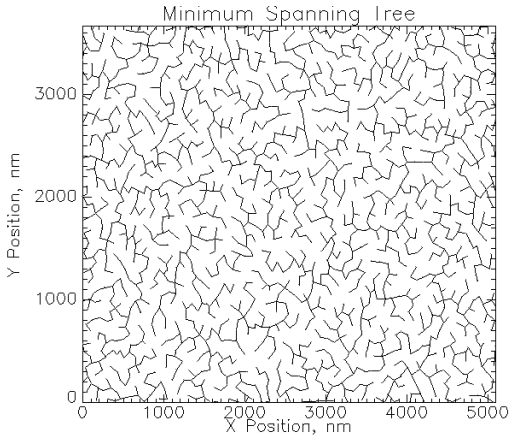

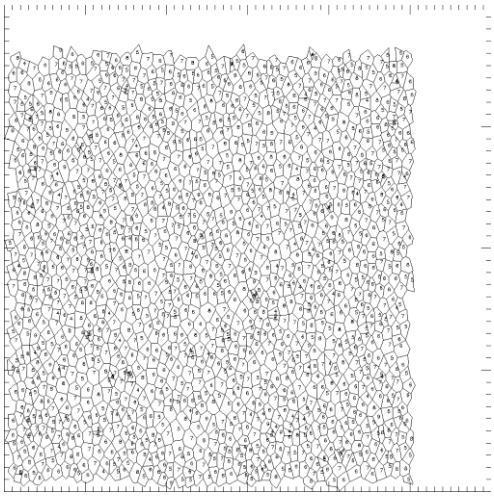

40V – Pore

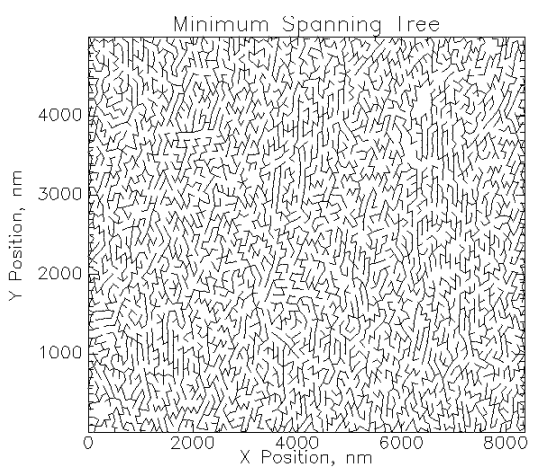

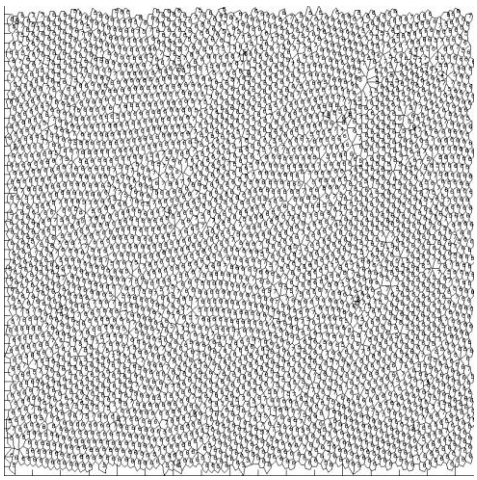

40V – Cap

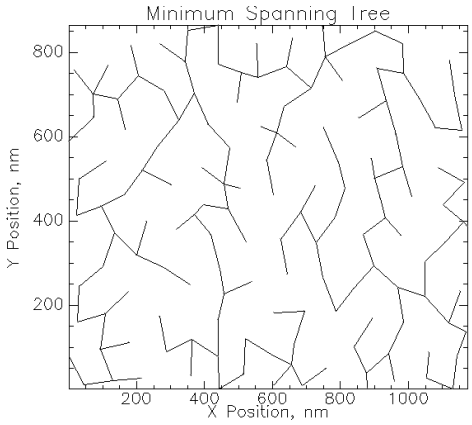

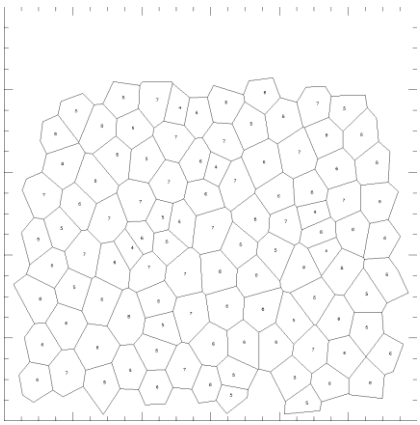

60V – Pore

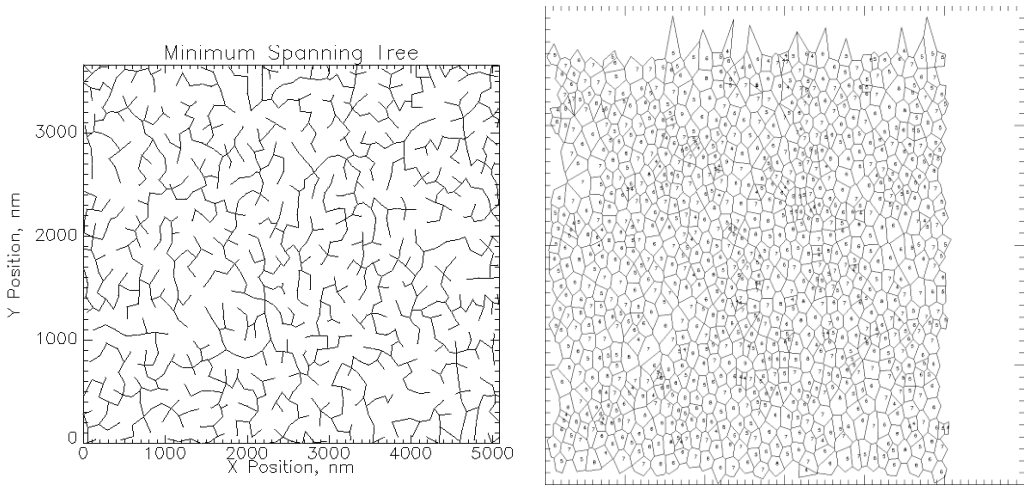

60V – Cap

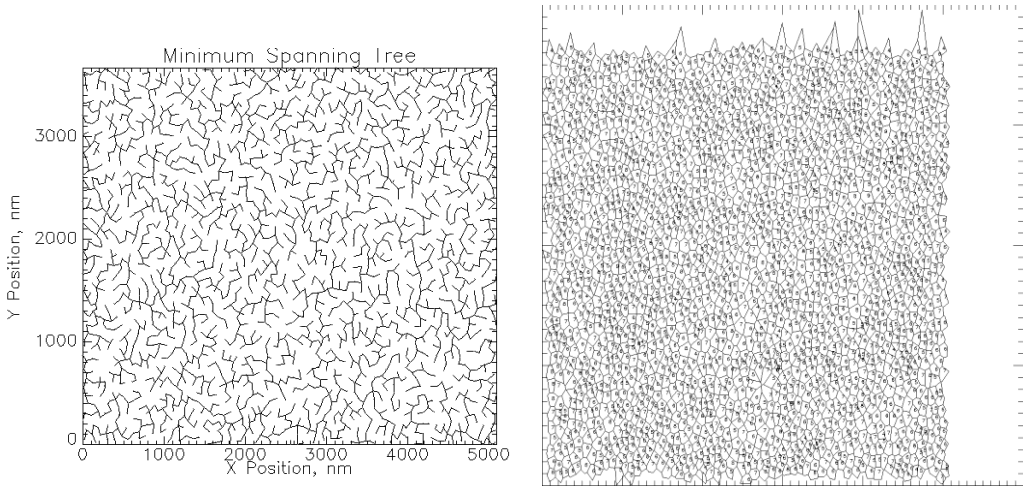

Appendix B

Polycrystalline anodic alumina – MST and VORONOI polygons

PCAA-01

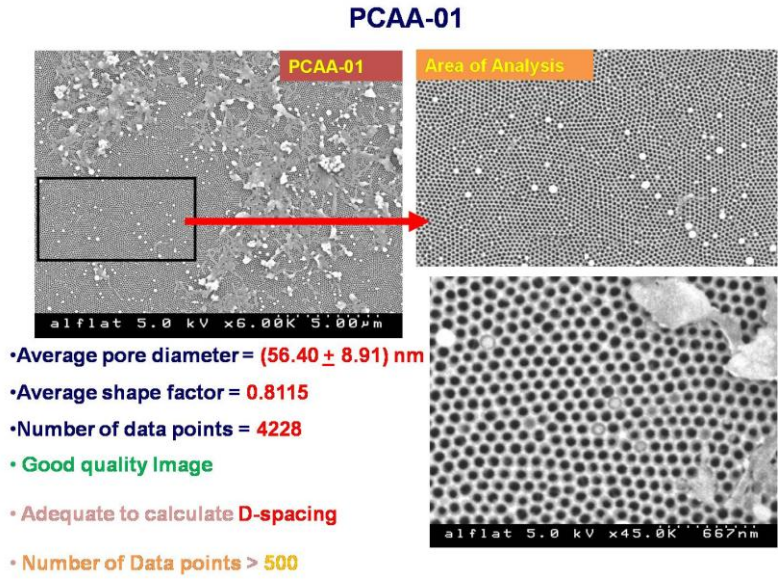

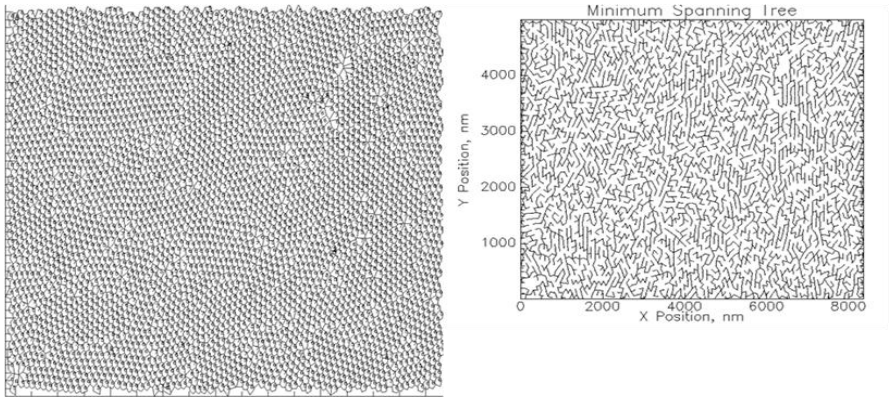

D-spacing = 97.3 ± 7.38 nm
Skewness = -1.46

PCAA-02

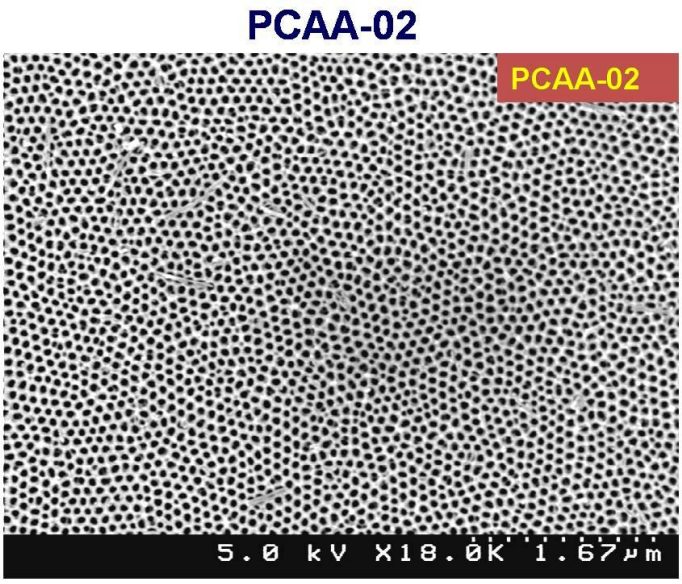

- Average pore diameter = (54.09 ± 9.19) nm
- Average shape factor = 0.935
- Number of data points = 2949

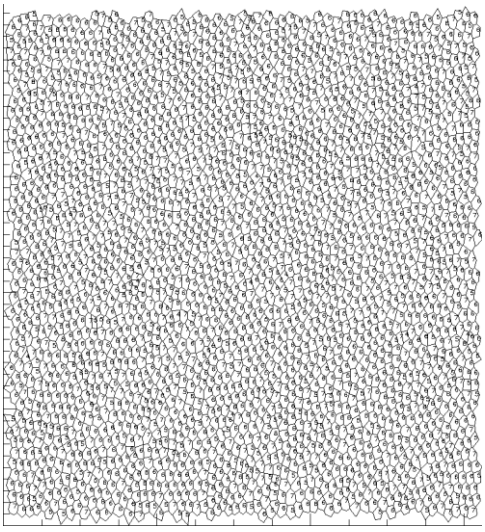

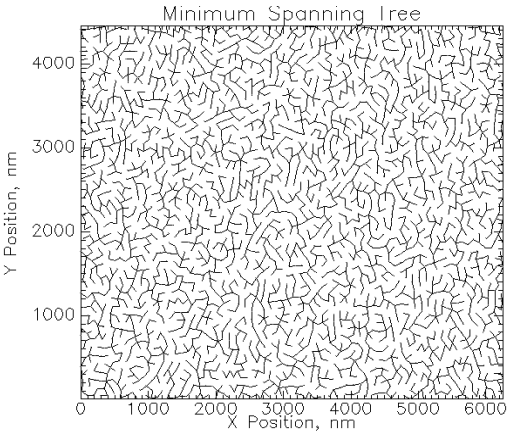

PCAA-03

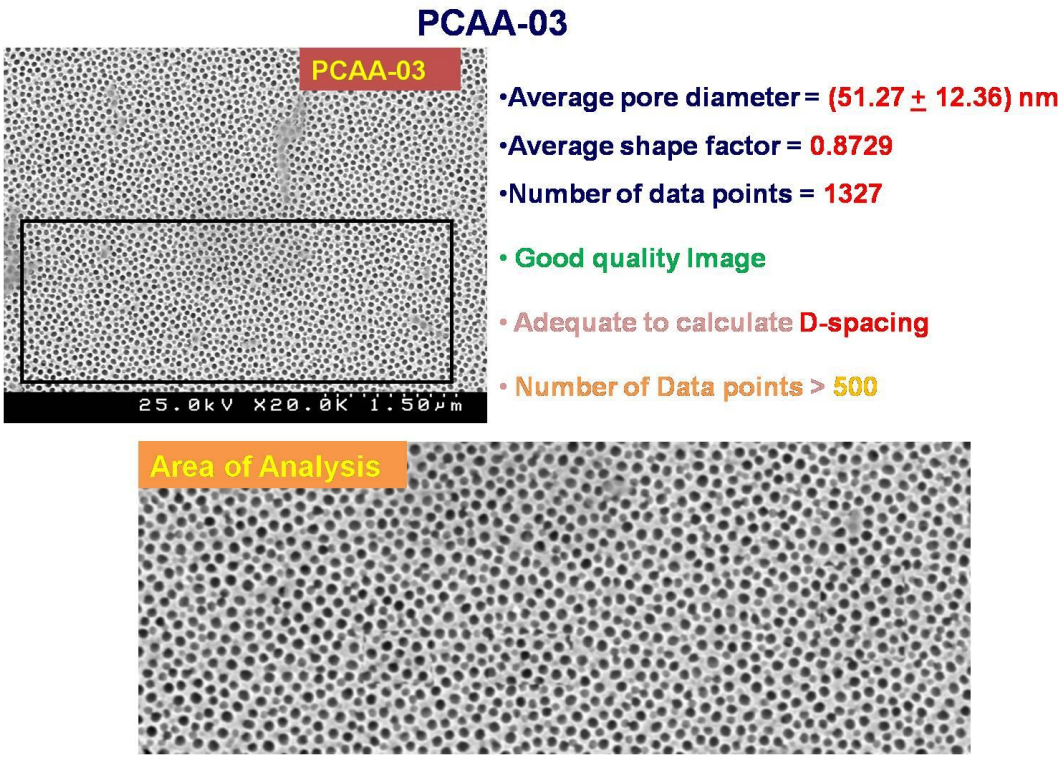
PCAA-03
•Average pore diameter = (51.27 ± 12.36) nm
•Average shape factor = 0.8729
•Number of data points = 1327
• Good quality Image
• Adequate to calculate D-spacing
• Number of Data points > 500
25.0kV X20.0K 1.50µm
Area of Analysis

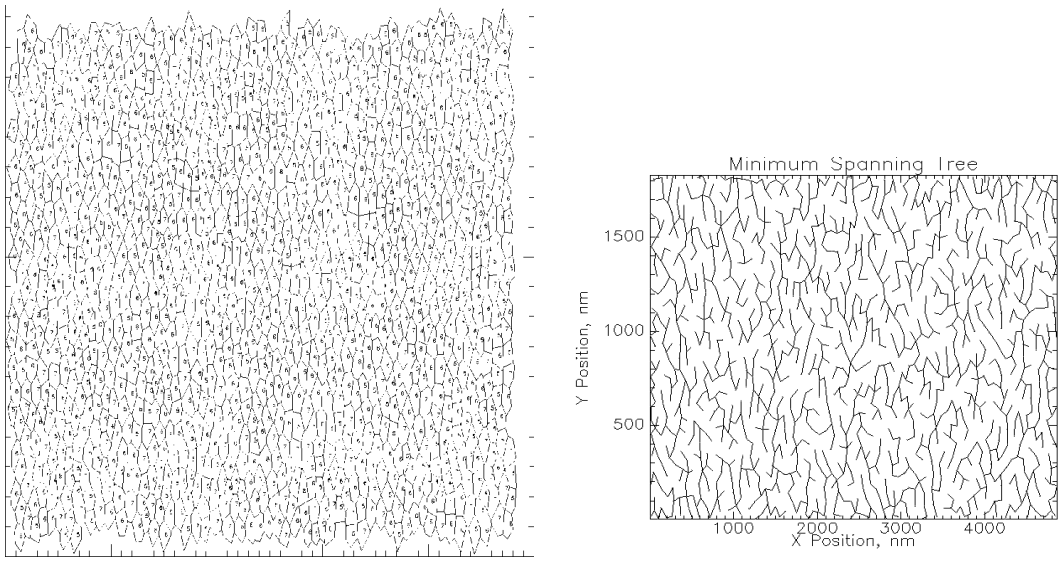
Minimum Spanning Tree
Y Position, nm
1500
1000
500
1000
2000
3000
4000
X Position, nm

PCAA-04

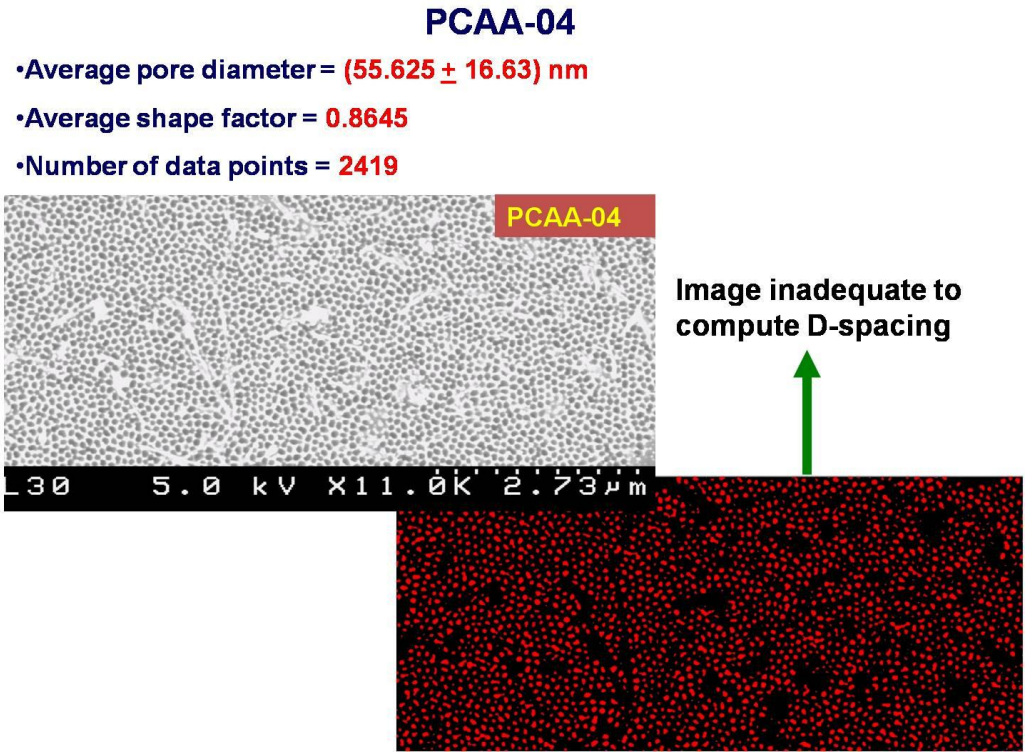

PCAA-05

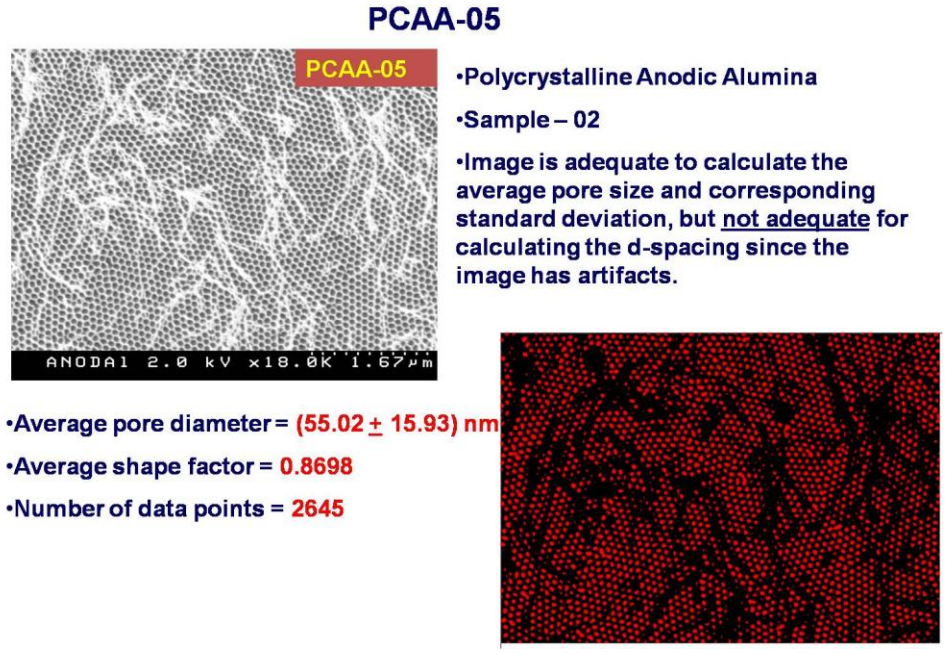

PCAA-06

PCAA-06

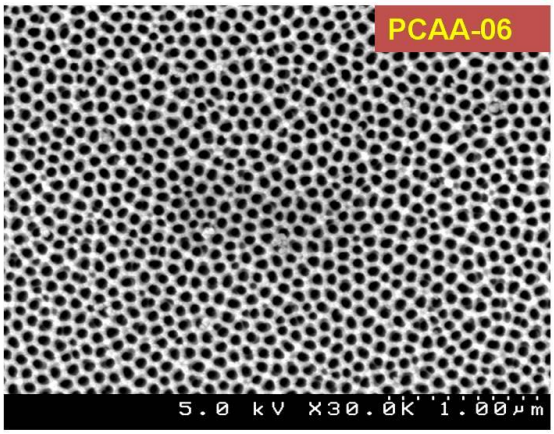

- Good quality Image
- Adequate to calculate D-spacing
- Number of Data points > 500

- Average pore diameter = (60.13 ± 11.31) nm
- Average shape factor = 0.8425
- Number of data points = 994

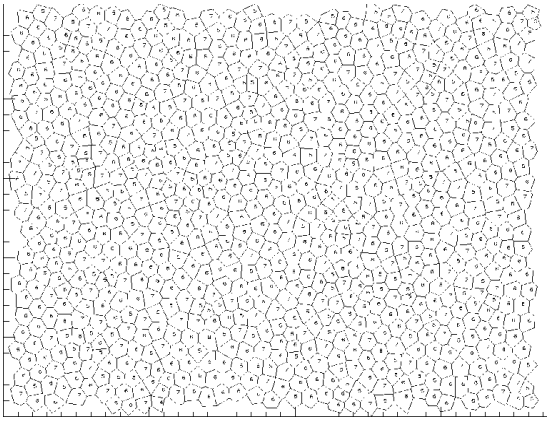

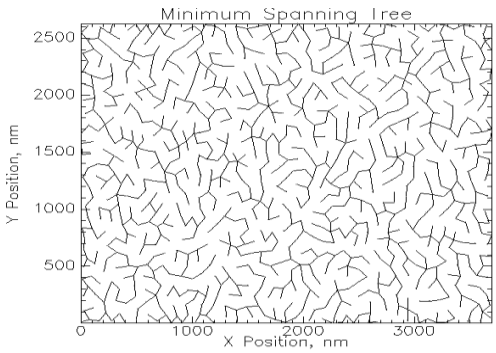

Appendix C

Single crystal anodic alumina – MST and VORONOI polygons

SCAA100-2

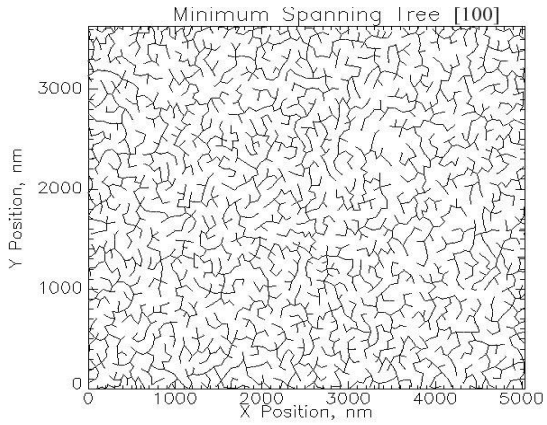

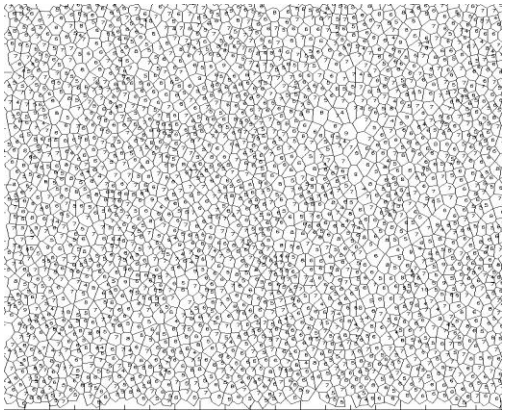

SCAA 100-3

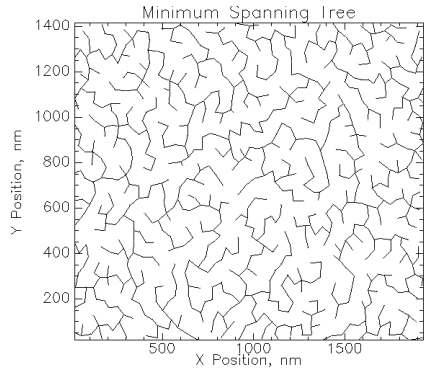

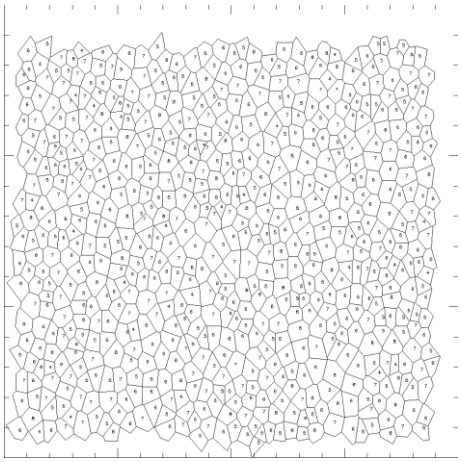

SCAA 110-2

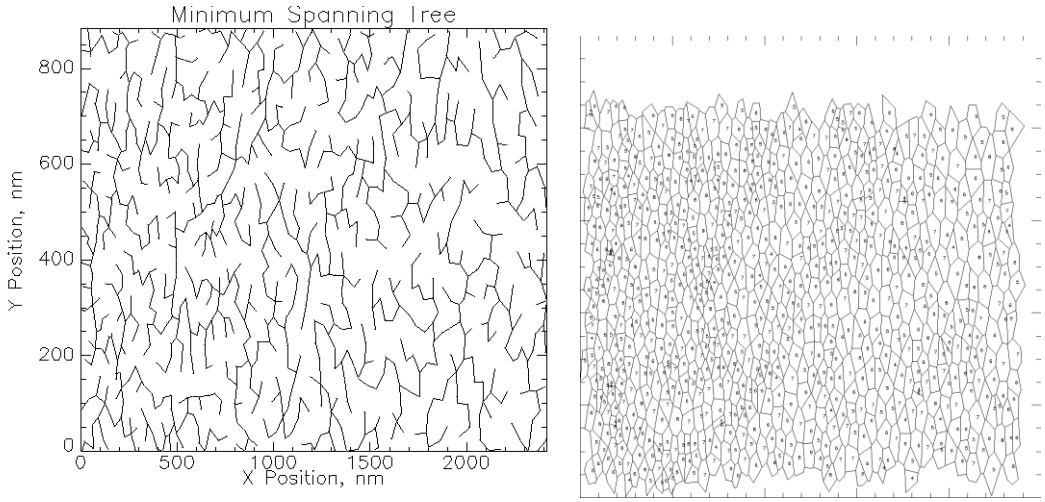

SCAA 110-3

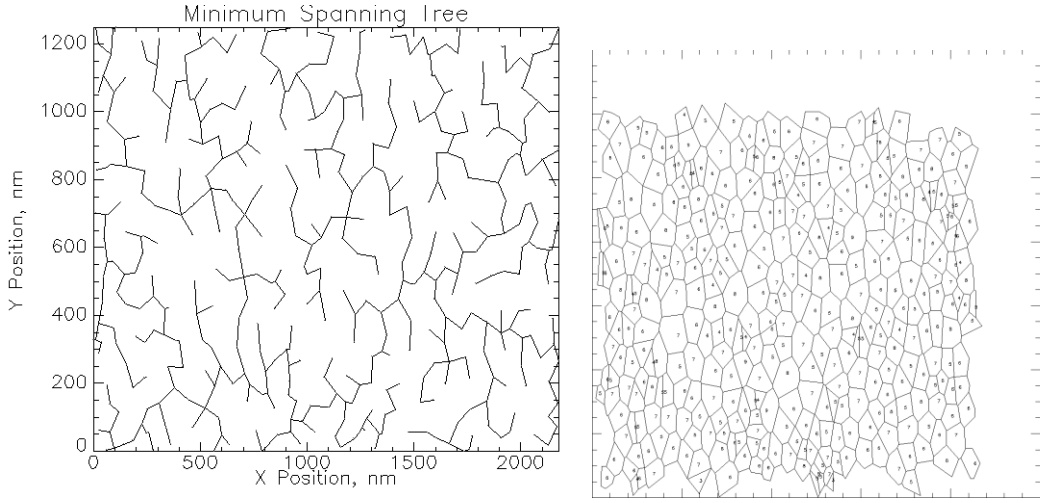

SCAA111-2

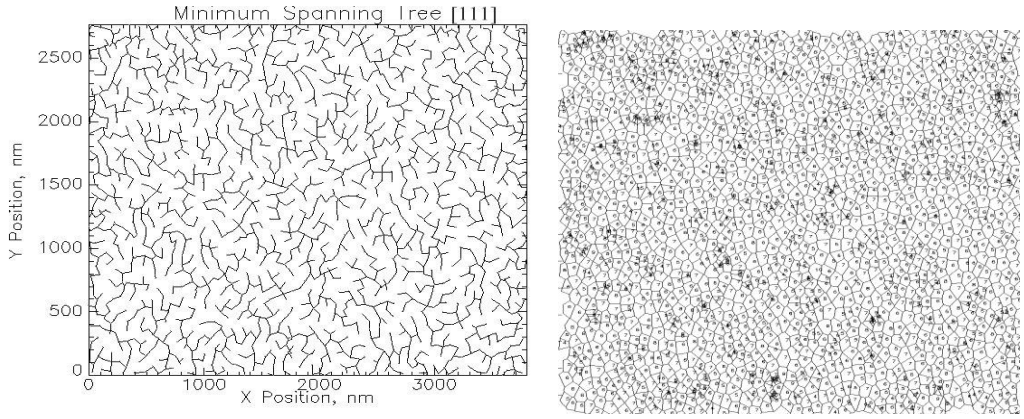

SCAA111-3

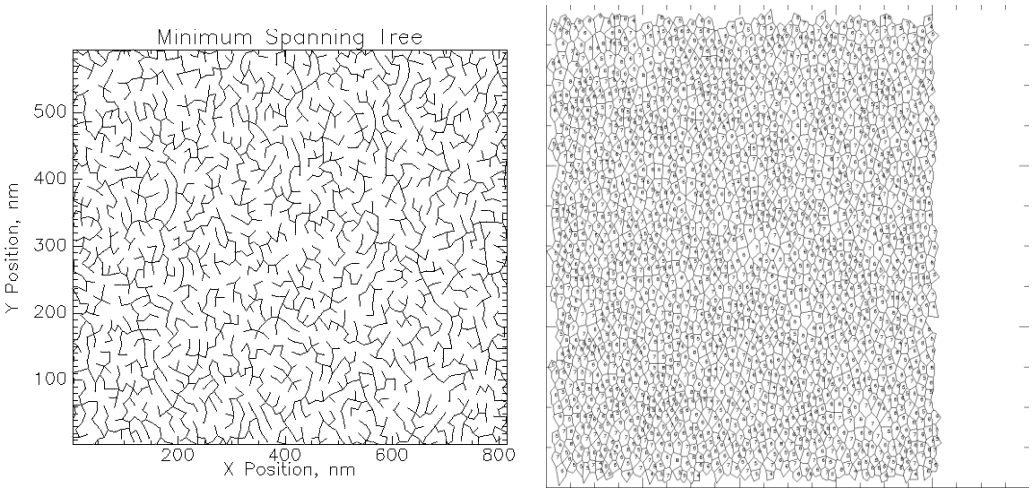

APPENDIX D

ANALYSIS – ONE WAY ANOVA-PORE DIAMETER AND NEAREST NEIGHBOR SPACING – SCAA

One Way Analysis of Variance

Data source: SCAA in Notebook 1

Group Name	N	Missing	Mean	Std Dev	SEM
Row 1	2056	0	38.031	11.132	0.246
Row 2	1651	0	21.191	7.007	0.172
Row 3	2100	0	30.786	12.922	0.282

Source of Variation	DF	SS	MS	F	P
Between Groups	2	259769.954	129884.977	1098.599	<0.001
Residual	5804	686194.207	118.228		
Total	5806	945964.161			

The differences in the mean values among the treatment groups are greater than would be expected by chance; there is a statistically significant difference (P = <0.001).

Power of performed test with alpha = 0.050: 1.000

All Pairwise Multiple Comparison Procedures (Holm-Sidak method):
Overall significance level = 0.05

Comparisons for factor:

Comparison	Diff of Means	t	Unadjusted P	Critical Level	Significant?
Row 1 vs. Row 2	16.840	46.866	0.000	0.017	Yes
Row 3 vs. Row 2	9.595	26.828	1.478E-149	0.025	Yes
Row 1 vs. Row 3	7.246	21.478	1.573E-098	0.050	Yes

Analysis – One way ANOVA of pore diameter – SCAA

One Way Analysis of Variance

Data source: Data 1 in Notebook 1

Group Name	N	Missing	Mean	Std Dev	SEM
Row 1	2056	0	63.240	14.300	0.315
Row 2	1651	0	45.720	11.360	0.280
Row 3	2100	0	52.320	18.130	0.396

Source of Variation	DF	SS	MS	F	P
Between Groups	2	294095.877	147047.939	645.054	<0.001
Residual	5804	1323093.583	227.962		
Total	5806	1617189.460			

The differences in the mean values among the treatment groups are greater than would be expected by chance; there is a statistically significant difference (P = <0.001).

Power of performed test with alpha = 0.050: 1.000

All Pairwise Multiple Comparison Procedures (Holm-Sidak method):
Overall significance level = 0.05

Comparisons for factor:

Comparison	Diff of Means	t	Unadjusted P	Critical Level
Row 1 vs. Row 2	17.520	35.114	4.183E-245	0.017
Row 1 vs. Row 3	10.920	23.312	5.616E-115	0.025
Row 3 vs. Row 2	6.600	13.290	1.004E-039	0.050

Analysis – One way ANOVA of nearest neighbor spacing – SCAA